Technische Universität München

Fakultät für Physik

Lehrstuhl für Molekulare Nanowissenschaften und
Chemische Physik von Grenzflächen (E20)

# Chemistry on noble metal surfaces: Towards covalently linked nanoarchitectures

Dissertation

Li Jiang

TECHNISCHE UNIVERSITÄT MÜNCHEN

Lehrstuhl E20 -

Molekulare Nanowissenschaften & Chemische Physik von Grenzflächen

# Chemistry on noble metal surfaces: Towards covalently linked nanoarchitectures

Li Jiang

Vollstädiger Abdruck der von der Fakultät für Physik der Technischen Universität München zur Erlangung des akademischen Grades eines Doktors der Naturwissenschaften (Dr. rer. nat.) genehmigten Dissertation.

Vorsitzender: Prof. Dr. Martin Zacharias
Prüfer der Dissertation: 1. Prof. Dr. Johannes Barth
2. Priv.-Doz. Dr. Markus Lackinger

Die Promotion wurde am 10.07.2017 bei der Technischen Universität München eingereicht und durch die Fakultät für Physik am 26.07.2017 angenommen.

# Abstract

Here we present a combined study using scanning tunneling microscopy and X-ray photoelectron spectroscopy under ultra-high vacuum to explore covalent bond formations on close-packed Ag, Au, Cu, and Pt single crystal surfaces. Besides the investigation of metal-organic interactions of a cyclic peptide, the main goal was to achieve and optimize covalent nanostructures via imine formation, Ullmann coupling and carbene formation. The most promising results were found for imine formation on Ag and for a prototypical N-heterocyclic carbene, which universally formed monolayers of bis-carbene metal adatom complexes.

# Kurzzusammenfassung

In der vorliegenden Arbeit wurde die Herstellung und Optimierung wohldefinierter molekularer Nanoarchitekturen auf dichtgepackten Ag-, Au-, Cu- und Pt-Einkristalloberflächen im Ultrahochvakuum mittels Rastertunnelmikroskopie und Photoelektronenspektroskopie untersucht. Neben der Untersuchung von metallorganischen Wechselwirkungen eines zyklischen Peptids, war das Hauptziel die Generierung kovalent gebundener Strukturen mittels Imine Bildung, Ullmann-Kupplung und Carbene Bildung. Die vielversprechendsten Ergebnisse wurden für die Imine Bildung auf Silber und für ein prototypisches N-Heterocyclisches Carben gefunden, welches generell metallorganische Dimere bildet.

# Contents

# List of Figures

# List of Tables

# 1. Introduction

Since more than a decade, ordered two-dimensional[1] or three-dimensional[2] molecular architectures have been implemented on a range of surfaces. A series of interactions have been utilized in their fabrication. Research focused on hydrogen bonds[3-6], π-π stacking[7], van der Waals[8], and metal-ligand interactions[9] for supramolecular systems. Recently there has been increasing interest in the development of covalently linked nanoarchitectures,[10-13] because they are thermally, mechanically, and chemically more stable. Hitherto, a variety of surface-confined covalent bond forming reactions have been explored, including Schiff base formation reaction[14-18], Ullmann coupling[10,19-24], dehydration condensation reaction[25-27], and others. These fabricated nanoarchitectures, especially when encompassing π-conjugated backbones show great potential for applications in fields such as electronics, sensors, batteries, and catalysts.[28-31]

For the handling of complex molecules on metals, adsorption geometry, mobility and lateral intermolecular interactions are determinants for generating designed nanoarchitectures, which not only depend on intermolecular interactions but also relate to the substrate environment, chemical nature, and symmetry.[32-34] Only the delicate balance of intermolecular vs. molecule-substrate interactions allows for the emergence of supramolecular structures.[35] Different nanoarchitectures have been notably explored on coinage metal substrates.

More recently, graphene nanoribbons doped with heteroatoms,[36-40] have been in the focus of intensive research, since their electronic structure can be tailored by the dopands.[41] Especially, N-doping can introduce additional n-type carriers into carbon systems, which is essential for semiconductor devices[42], energy conversion and storage[43,44], as well as bio-sensing applications[45-47].

Carbenes are currently considered a promising alternative to thiols for self-assembled monolayers (SAMs)[48] as well as metal-molecule junctions. They are thermally robust entities[49] with rich chemical reactivity[50,51] and predicted to have superior electronic conductivity to thiols.[52] Moreover, N-heterocyclic carbenes (NHC) are excellent ligands for metal complexes and nanoparticles.[53,54]

Beside organic molecules, natural cyclic peptides are also used as versatile molecular building units for emerging nanodevices[55-57], due to their unique chemical conformation and

functional diversity. One application is to channel metal ions such as $K^+$ because certain peptides can interact with ions in their centers or on specific residues.[58]

However, the exploration of potential pathways for the targeted design of such nanostructured devices still needs intense investigations. In this thesis, we focus on this challenge and present systematic measurements in ultra-high vacuum describing novel bottom-up nanofabrication methods. Our basic analytical tool has been the scanning tunneling microscope (STM), which was invented in the early 1980's by Gerd Binnig and Heinrich Rohrer[59], and allows to obtain real-space imaging of a surface on the atomic level, the detailed molecular arrangement and even the orientation of the molecules on the surface. X-ray photoelectron spectroscopy (XPS) can provide information about the chemical state of molecular moieties, which is helpful to explain the self-assembly changes and uncover potential reaction mechanisms. These two techniques are described in finer detail in chapter 2. This chapter also describes the detailed experimental setup, the sample preparation procedures, and the structural modelling of molecular compounds.

Chapter 3 comprises four sections, each presenting the results of the investigated molecules. The first two sections focus on synthesizing N-doped graphene nanoribbons by two different pathways: Schiff base formation and Ullmann coupling. The employed molecules are shown in **Table 1.1**.

Section 3.1 provides a systematic investigation of different combinations of tetraketone and tetraamine molecules aiming to trigger the Schiff base formation reaction. The behavior of the tetraketone 1 and tetraamine 1 as a function of the annealing temperature and stoichiometry of tetraketone to tetraamine on three coinage metal surfaces: Ag(111),Au(111), and Cu(111) is studied by STM. It turns out that only on Ag(111), oligomers were generated under certain conditions. Combined with XPS measurements, the role of the substrate and the reaction mechanism are elucidated. In the following, other precursors (tetraketone 2, 3 and tetraamine 2, 3) differing in substituents in an attempt to tune the interaction with the substrate by introducing more or less bulky groups, were tried on the Ag(111) substrate, albeit without achieving longer ribbons.

**Table 1.1:** Molecules investigated in section 3.1 and 3.2 of Chapter 3.

| N-doped graphene nanoribbons | | |
|---|---|---|
| Schiff base formation | | Ullmann coupling |
| Tetraketone 1 | Tetraamine 1 | DBBQ |
| 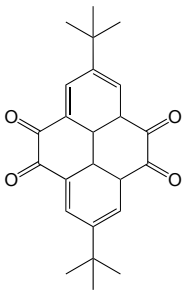 | 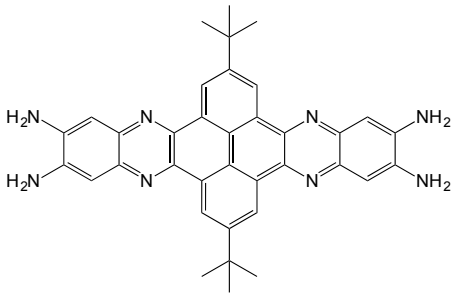 | 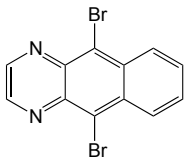 |
| Tetraketone 2 | Tetraamine 2 | DBBPP |
| 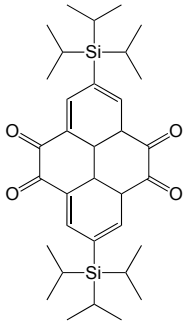 | 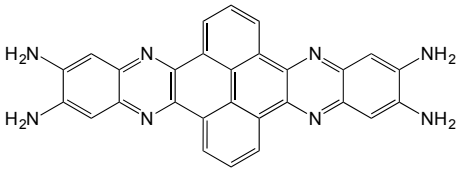 | 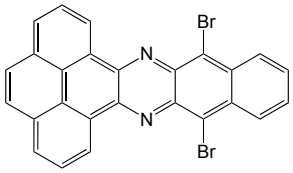 |
| Tetraketone 3 | Tetraamine 3 | |
| 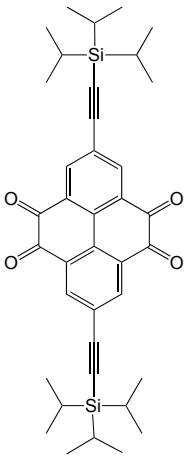 | 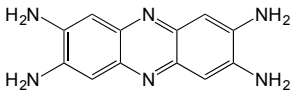 | |

In section 3.2, a different route to N-doped nanoribbons was envisaged, whereby a two-step reaction would be used, first utilizing Ullmann coupling, followed by

cyclodehydrogenations. Two molecules (DBBQ and DBBPP, table 1.1) were addressed on three different metal substrates: Ag(111), Au(111), and Cu(111). But unfortunately, there are no ordered polymeric chains observed under any circumstances. There is a significant discovery deduced from N 1s spectra, which could probably explain this failure.

The self-assembly and chemical nature of the NHC ligands on three substrates: Cu(111), Au(111), and Pt(111), are systematically elucidated in section 3.3 with a combination of microscopy and XPS. 1,3-dimethyl-1*H*-imidazol-3-ium-2-carboxylate is employed as the precursor of the NHC 1,3-dimethyl-1*H*-imidazol-3-ium-2-ide (IMe). Dimeric $(IMe)_2$-metal species formed on all three substrates.

Section 3.4 summarizes the interaction of a macrocyclic peptide (Cyclosporin A) with different metals: K, Co, and Fe on a Cu(111) substrate. The role of the metal for different supramolecular assemblies and configurations were addressed.

Chapter 4 gives conclusions and an outlook regarding future perspectives.

# 2. Experimental Methods: Theory and Setup

This chapter describes the techniques and instrumentations utilized for the experiments conducted in context of the present thesis. The experiments mainly rely on STM. Therefore, the first section gives a brief introduction of the physical principles of the tunneling effect, a general description of STM, the details of the variable-temperature STM and the ultrahigh vacuum chamber setup, and the applied preparation procedures. Apart from STM experiments, XPS measurements were also employed, which were carried out at the HE-SGM dipole magnet beamline at the BESSY II in Berlin or in a dedicated facility (SPECS GmbH) at the E20—WSI laboratory in Garching. The following section briefly introduces the basic theoretical background of XPS together with the general description of the different setups employed.

## 2.1 The scanning tunnelling microscopy

STM has been widely used as a microscopic technique that allows the investigation of (semi)conducting surface properties down to the atomic scale.

### 2.1.1 The tunnelling effect

STM is based on the physical phenomenon of tunneling effect, which arises from quantum mechanics[60,61]. In classical mechanics, an object cannot penetrate a potential barrier higher than its overall energy. However, in quantum mechanics, an electron can pass through a potential barrier even if its energy is lower than the barrier potential as shown in **Figure 2.1**.

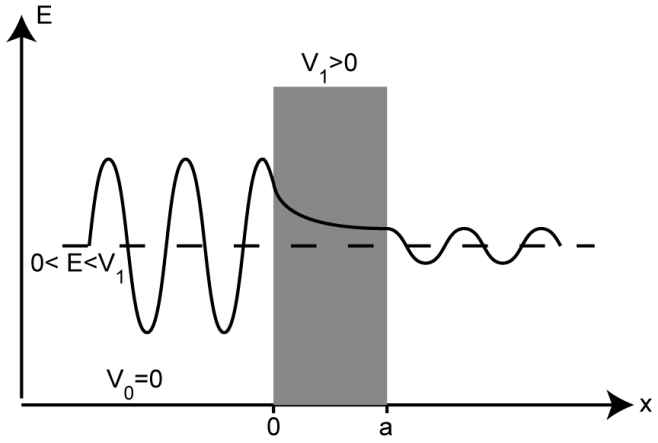


**Figure 2.1:** Schematic illustration of an electron wave function with the energy $E$ tunneling through a potential barrier of $V_1 > E$ [60]

The following description will focus on electrons in one dimension. The time independent Schrödinger equation (TISE) of an electron with the wave function $\psi$ can be written as:

$$\frac{d^2\psi}{dx^2} = \frac{2m}{\hbar^2}(V_x - E)\psi \tag{2.1}$$

with $m$ being the electron mass, $E$ the energy of the electron, $\hbar$ the Planck constant divided by $2\pi$, $x$ the spatial coordinate and $V$ the potential energy. Here $V = V_1 > E$ for $0 \leq x \leq a$, and $V = V_0 = 0$ for $x \leq 0$ and $x \geq a$ (**Figure 2.1**).

The general solution to the TISE is:

$$\psi = \begin{cases} A_1 e^{ikx} + A_2 e^{-ikx}, & (x \leq 0) \\ B_1 e^{\kappa x} + B_2 e^{-\kappa x}, & (0 \leq x \leq a) \\ C_1 e^{ikx} + C_2 e^{-ikx}, & (x \geq a) \end{cases} \tag{2.2}$$

where $A_1$, $A_2$, $B_1$, $B_2$, $C_1$, and $C_2$ are constants, $k = \sqrt{\frac{2mE}{\hbar^2}}$ and $\kappa = \sqrt{\frac{2m(V_1-E)}{\hbar^2}}$. Since for $x \geq a$, we can only have waves propagating out of the potential barrier, $C_2$ can be set equal to zero. By imposing the continuity of the wave function at 0 and $a$, we can express the transmission coefficient as:

$$T = \left(1 + \frac{(k^2+\kappa^2)^2}{4k^2\kappa^2}\sin h^2(\kappa a)\right)^{-1} \tag{2.3}$$

For a large attenuating barrier, this can be approximated as:

$$T \approx \frac{16k^2\kappa^2}{(k^2+\kappa^2)^2} e^{-2\kappa a} \tag{2.4}$$

We can see that the transmission coefficient has an exponential dependence on the tunneling barrier width.

Accordingly, the tunneling current can be expressed as:

$$I_t = Ce^{-2\kappa a} = Ce^{-2\frac{\sqrt{2m(V_1-E)}}{\hbar}a} \tag{2.5}$$

where $C$ is a constant.

This expression for the tunneling current, which is based on the simple model of an individual electron passing through a potential barrier, provides a first idea on tunneling between two solid surfaces. The tunneling current is exponentially dependent on the distance between the sample and the tip.

In the metal-vacuum-metal system, the potential of the barrier $V_1$ can be replaced by the vacuum level of the metal. The work functions of sample and tip are assumed to be the same. Applying a voltage $V_b$ between them leads to a net tunneling current. As electron conductivity is a prerequisite for detecting current, STM is not suitable for the investigation

of insulating samples. Therefore, an electron of an occupied sample state $\psi_n$ whose energy lies in between $E_F$ and $E_F - eV_b$ has a possibility to tunnel into the tip (**Figure 2.2**).

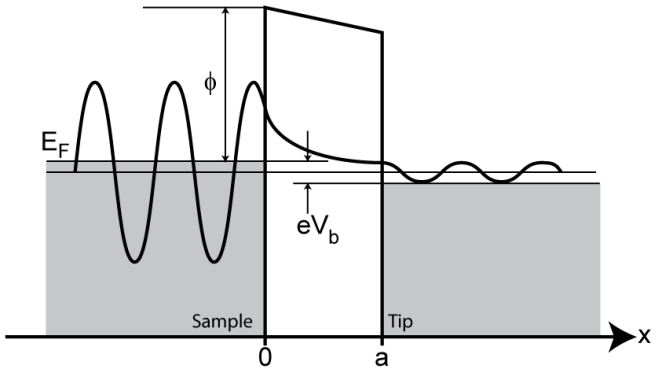


**Figure 2.2:** Schematic illustration of the metal-vacuum-metal system showing the tunneling process from the sample into the tip at finite voltage[61].

Assuming that the sample state *n* of interest is lying close to the Fermi level, the probability of an electron tunneling from this sample state to the surface of the tip is analogous to

$$|\psi_n(0)|^2 e^{-2\kappa a} \text{ with } \kappa = \sqrt{\frac{2m\phi}{\hbar}} \tag{2.6}$$

As a finite number of sample states exist, summing up over all sample states between $E_F$ and $E_F - eV_b$ leads to the formulation for the tunneling current:

$$I_t \propto \sum_{E_F - eV_b}^{E_F} |\psi_n(x)|^2 \tag{2.7}$$

Supposing a constant local density of states (LODS) for the tip as well as low voltages and $T = 0$, equation 2.7 can be written as:

$$I_t \propto V_\rho(0, E_F) e^{-2\kappa a} = V_\rho(0, E_F) e^{\frac{-2a\sqrt{2m\phi}}{\hbar}} \tag{2.8}$$

where $\rho(x, E_F)$ is the local density of states (LDOS) of the sample. From this correlation we can see that the tunneling current is proportional to the voltage and the LDOS, but it is exponentially dependent on the distance between the sample and the tip.

Bardeen[62] introduced that tip and sample have different wave functions and that there is a matrix element, which describes the overlap of the two wave functions. Tersoff and Hamann[63] considered a tip represented by a locally spherical potential well and evaluated the matrix element for an *s*-type tip wave function and the two wave functions that do not influence each other. For small bias voltages $V_b$, the tunneling current $I_t$ is directly proportional to the LDOS of the sample.

$$I_t \propto V_b e^{-2kR} \rho_{tip}(E_F) \rho_{sample}(E_F, \gamma_0) \text{ with } k = \frac{\sqrt{2m\phi_t}}{\hbar} \tag{2.9}$$

where $R$ is the effective tip radius, $\phi_t$ the barrier height and $\gamma_0$ the center of curvature of the tip. This indicates that an STM image does not represent the true topography of the surface, but a convolution of the LDOS and the topography, which is also influenced by the shape of the tip.

### 2.1.2 Scanning modes

In STM experiments, the tip is first moved by a piezo tube scanner to carefully approach to the surface. Once the tip is close enough to the surface for a tunneling current to be recorded, the tip scans the surface line-by-line. There are two important scanning modes: constant current mode and constant height mode (**Figure 2.3**).

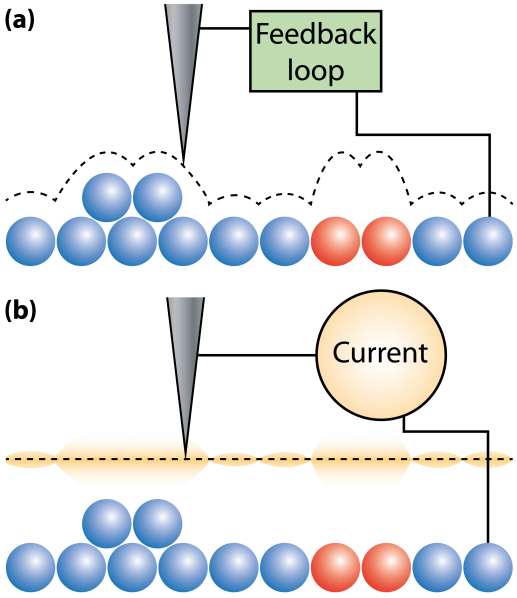


**Figure 2.3:** Illustration of the two STM operation modes: (a) The constant current mode. (b) The constant height mode.[64]

The constant current mode is the one used in most cases, where the height of the tip is adjusted continuously by means of a feedback loop, so that a chosen tunneling current remains always constant. A topographic image is derived by recording the movement of the tip. The substituted atoms shown in red in **Figure 2.3** exhibit a different apparent height compared to the blue surface atoms due to their different local density of states.

In the constant height mode, the average height of the tip above the surface is constant and variations of the tunneling current are recorded, shown by an orange glow. Similarly, the current of the substituted atoms is higher than that of the surrounding surface atoms. The advantage of this mode is that it does require a quick responding feedback loop, which

allows high scanning speeds and eliminates related artifacts. But there is the risk of crashing the tip into the sample.

### 2.1.3 Experimental setup

All the STM measurements were performed in a custom designed ultra-high vacuum (UHV) system equipped with a commercially available variable-temperature STM (Aarhus 150 SPECS Surface Nano Analysis GmbH[65,66]). The setup is schematically shown in **Figure 2.4**. This UHV system consists of two chambers: the STM chamber and the preparation chamber separated by a vertical gate valve. The preparation chamber is used to prepare the sample, for example, cleaning the surface by $Ar^+$ sputter guns, dosing molecules on the surface through an organic molecular beam epitaxy (OMBE), and physical vapor deposition (PVD) of metals on the surface via home built metal evaporators. The molecules are filled in quartz crucibles with a diameter of 5 mm and sublimated into vacuum by heating. Our OMBE can hold four crucibles at the same time. The parking stage can store up to four samples and comprises a heating stage. The sample can be heated by electron beam heating up to 1200 K. After the preparation, the sample can be transferred through the combination of different manipulators (**Figure 2.4**(6, 10, 12)) to the STM chamber to perform atomic scale investigations. The manipulator located in the load-lock is used to transfer samples from air into the UHV chamber without breaking the vacuum.

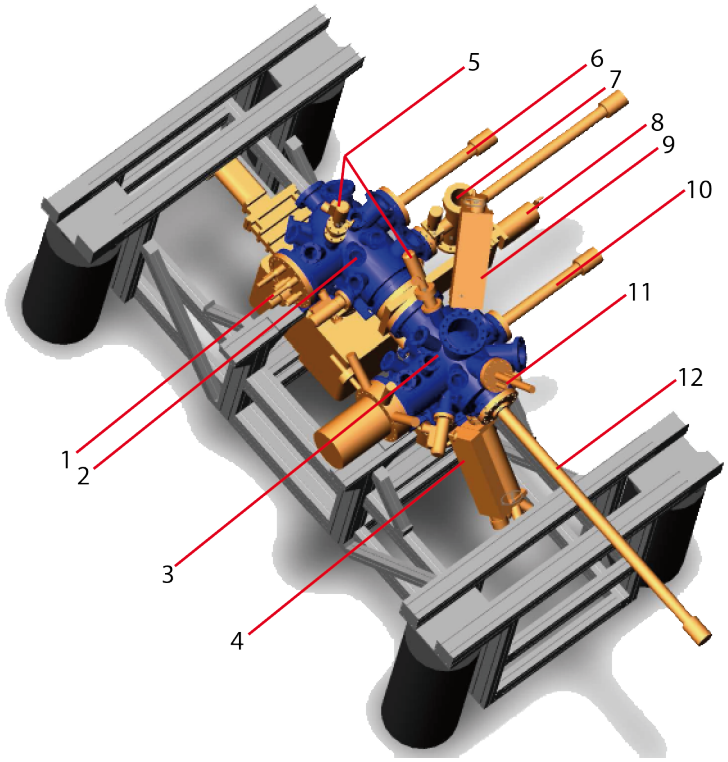

**Figure 2.4:** Setup of the UHV chamber. (1) The variable-temperature Aarhus STM, (2) STM chamber, (3) preparation chamber, (4) OMBE, (5) argon sputter guns in two chambers, (6, 10, 12) manipulators, (7) load-lock, (8) gate valve, (9) metal evaporator, (11) sample parking stage.[67]

The ultra-high vacuum system is maintained by a three-stage pumping system connected in series. The first pumping stage of the system is a rotary pump that can reduce the pressure to roughly $10^{-3}$ mbar. A small turbo molecular pump as the second pumping stage further decreases the pressure to ~ $10^{-7}$ mbar. The main pump located on the bottom of the preparation chamber is a big turbo molecular pump that can pump the whole system to a base pressure up to $2\times10^{-10}$ mbar after a proper bake-out. Besides, there is an ion getter pump situated in the STM chamber supporting the whole pumping system.

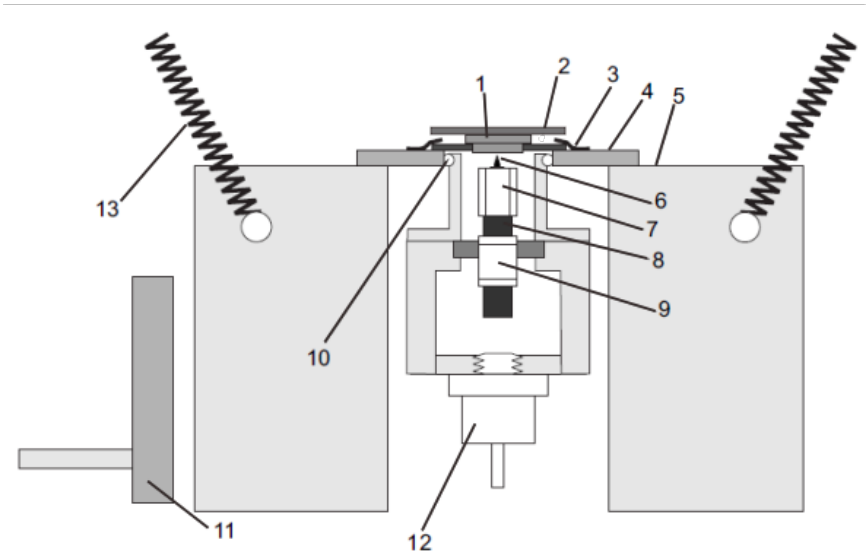


**Figure 2.5:** Cross-section side view of the Aarhus STM. (1) Sample, (2) sample holder, (3) clamps, (4) base plate, (5) aluminum block, (6) tungsten tip, (7) scanner piezo motor, (8) SiC rod, (9) inchworm piezo motor, (10) ceramic balls, (11) cooling finger, (12) Zener diode, (13) suspension springs.[68]

The cross section side view of the Aarhus STM is shown in **Figure 2.5**. The pre-mounted sample is inserted into the scanning stage and fixed with two clamps (3). The STM scanner is located on top of an inchworm motor (9) that is used to coarsely approach the tip towards the surface. The piezo motor (7) can further move the SiC rod (8) with high precision in a range of several millimeters. In our case, we used tungsten tips (6) for all the experiments, which were sharpened by electrochemical etching and pre-mounted on a tip holder. A Zener diode (12) is designed to heat the STM scanner and keep it at room temperature or above. The scanner is mounted inside the base plate (4) and fixed with ceramic balls (10). The aluminum block can be cooled with cooling agent such as liquid nitrogen while locked by

the cooling finger (11). But the scanner is thermally insulated from the aluminum block, which is used to keep the scanner at a set temperature when conducting experiments at low or elevated temperatures. In order to stay isolated from the external vibrations, the whole STM setup is suspended through springs (13) and the aluminum block is supported by three Viton bands.

### 2.1.4 Sample preparation procedures

In the present thesis, we studied the self-assembly and molecular behaviors of different molecules on Ag(111), Au(111), Cu(111) and Pt(111) substrates. Firstly, the single-crystal surfaces were prepared by repeated cycles of $Ar^+$ sputtering and subsequent thermal annealing. The sputter gun can ionize argon and accelerate the argon ions with high voltage of 1 kV and emission current of 15 mA. The adsorbates and impurities are removed by bombarding the surface with $Ar^+$, but the top layers of the surface atoms are also partly removed, leaving a rough surface. The subsequent annealing in vacuum to 650 K (Au), 700 K (Ag), 770 K (Cu), and 980 K (Pt) can heal the surfaces to get clean and atomically flat surfaces eventually. For Pt(111) surface, the annealing was performed in a $5\times10^{-8}$ mbar of $O_2$ to oxidize carbonaceous impurities.

After cleaning, the molecules were deposited on the substrates by OMBE. The investigated molecules with corresponding sublimation temperatures are listed in **Table 2.1**. The sample was kept at room temperature during evaporation. The deposition time was appropriately controlled to attain the desired molecular coverage. After dosing molecules, the sample was transferred to the STM chamber to do the analysis. STM measurements were conducted in a range betwee 93 K to 300 K. Images were processed with the WSxM program[69].

**Table 2.1:** Molecules investigated in the present thesis and their corresponding manufacturer, purity and sublimation temperatures.

| **Molecule** | **Provided/acquired by** | **Purity** | **Sublimation temperature / K** |
|---|---|---|---|
| Tetraketone 1 | S. More, R. Bhosale, A. Mateo-Alonso (Freiburg University, POLYMAT Spain) | ≥ 99% | 470 |
| Tetraketone 2 | A. Belén Marco, A. Mateo-Alonso (POLYMAT Spain) | ≥ 99% | 470 |

| | | | |
|---|---|---|---|
| Tetraketone 3 | D. Cortizo-Lacalle, A. Mateo-Alonso (POLYMAT Spain) | ≥ 99% | 510 |
| Tetraamine 1 | S. More, R. Bhosale, A. Mateo-Alonso (Freiburg University, POLYMAT Spain) | ≥ 99% | 650 |
| Tetraamine 2 | Gabriella Antonicelli, A. Mateo-Alonso (POLYMAT Spain) | ≥ 99% | 680 |
| Tetraamine 3 | Gabriella Antonicelli, A. Mateo-Alonso (POLYMAT Spain) | ≥ 99% | 510 |
| DBBQ | V. Montagna, A. Mateo-Alonso (POLYMAT Spain) | ≥ 99% | 410 |
| DBBPP | V. Montagna, A. Mateo-Alonso (POLYMAT Spain) | ≥ 99% | 450 |
| 1,3-dimethyl-1*H*-imidazol-3-ium-2-carboxylate precursor to 1,3-dimethyl-1H-imidazol-3-ium-2-ide (IMe) | G. Médard, B. Küster (Proteomics and Bioanalytics, TUM) | ≥ 99% | 380 |
| Cyclosporin A | Sigma Aldrich | ≥ 98.5% | 470 |

## 2.2 X-ray photoelectron spectroscopy (XPS)

XPS is widely used to monitor chemical changes, which can provide complementary information to explain the STM results. In this thesis, XPS experiments were carried out at HE-SGM dipole magnet beamline at the BESSY II in Berlin or in a dedicated facility (SPECS GmbH) at the TUM—WSI laboratory in Garching.

### 2.2.1 Basic principles of XPS

XPS is based on photoelectric effect and the basic principle of the photoelectric effect was enunciated by Einstein in 1905[70]. Each atom has its own core electrons with characteristic binding energies. When an X-ray beam, usually soft X-ray radiation in a range of 200-1500 eV, is directed to the sample surface, the energy of the X-ray photon is adsorbed (in **Figure 2.6**). If the photon energy $h\nu$ is large enough, a core electron will then escape from the atom and be emitted out of the surface. The emitted electron with the kinetic energy of $E_k$ is called photoelectron and is detected by an electron analyzer.

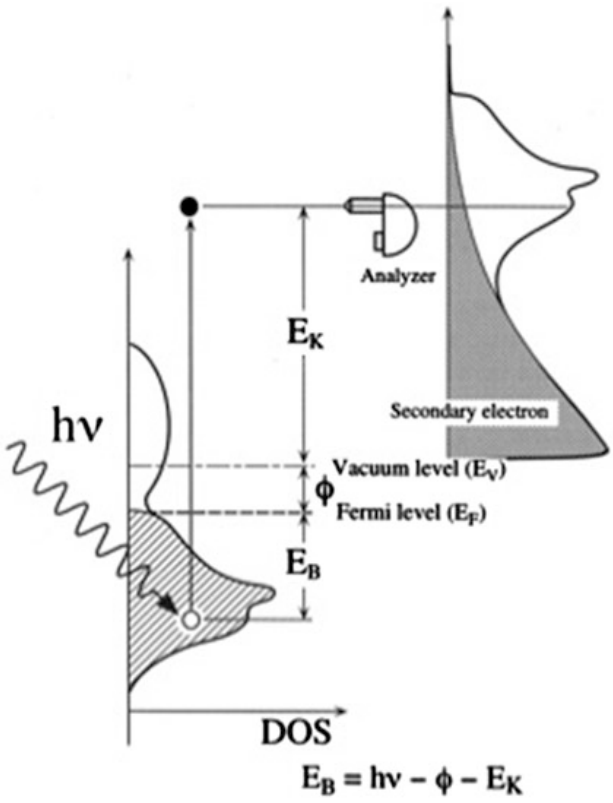


**Figure 2.6:** Schematic illustration of the excitation of core electrons by X-ray radiation. The kinetic energy of the photoelectrons is detected by an electron analyzer.[71]

The binding energy of the core electron is given by the equation 2.10.

$$E_B = h\nu - E_k - \phi \tag{2.10}$$

where $h\upsilon$ is the excitation energy, $E_k$ is the measured kinetic energy of photoelectron, and $\phi$ is the work function of the analyzer.

The binding energy of core levels is characteristic for each element and the chemical shift can be utilized to identify its chemical environment changes.

### 2.2.2 Experimental setup and procedures

Part of the XPS experiments were performed in the HE-SGM dipole magnet beamline at the BESSY II in Berlin. It consists of three chambers, the preparation chamber, the analysis chamber, and a transfer chamber with a rotatable manipulator (UFO) that allows transferring samples between two chambers. The base pressures of the preparation chamber and analysis chamber are $2\times10^{-8}$ mbar and $2\times10^{-10}$ mbar, respectively. The preparation chamber is equipped with a sputter gun and an OMBE. The samples were prepared employing similar procedures as described in previous section 2.1.4. The spectra were collected in the analysis chamber using a Scienta R3000 hemispherical electron energy

analyzer mounted in the plane of the photon polarization, 45° from the incident photon beam.

Additional XPS measurements were carried out at a dedicated facility (SPECS GmbH) at the TUM—WSI laboratory in Garching. The experimental chamber operates at a base pressure of $2\times10^{-10}$ mbar and is equipped with a PHOIBOS 150 hemispherical analyzer, a XR50 X-ray source with ellipsoidal crystal FOCUS 500 monochromator (SPECS GmbH) delivering monochromatized Al Kα radiation (hν = 1486.74 eV), and all ancillary facilities for surface preparation and cleaning.

The XPS experiments were conducted in normal emission geometry. For the acquisition of the C 1s, N 1s, O 1s spectra, the excitation energies at BESSY were 435 eV, 550 eV, and 680 eV, respectively. The binding energy of the XP spectra was calibrated against the Ag $3d_{5/2}$, Au $4f_{7/2}$, or Cu $2p_{3/2}$ core levels at 368.3 eV, 84.0 eV, or 75.1 eV, respectively. For the acquired XPS data, a liner or Shirley background was subtracted from the raw data, and Voigt functions were used to fit the individual components.

## 2.3 Structural modelling of molecular compounds

In the first two sections of chapter 3, the molecular models were built in ChemDraw 3D software by applying minimal energy optimization.

In the third section, the molecular models proposed are substructures of compounds with reported single crystal data. The atomic coordinates of the C, N and metal atoms in the tentative molecular models presented are based on the respective reported single crystal data, while the positions of the hydrogen atoms are estimated with a C-H bond distance of 0.1 nm. The single crystal data used were retrieved from http://www.crystallography.net and correspond to 5,5'-6,6'-tetramethoxy-1,1'-3,3'-tetramethylbibenzimidazolinylidene[72] for the tetraazafulvane, N,N′-bis[2,6-(di-isopropyl)phenyl] imidazol-2-ylidene-N,N′-(dicyclohexyl)imidazol-2-ylidene Copper(I)[73] for the $Cu(IMe)_2$, (9,11,20,22,23,25-hexamethyl-3,6,14,17-tetraazapentacyclo[17.3.1.13,6.18,12.114,17]hexacosa-1(23),4,8(25),9,11,15,19,21-octaene-24,26-diylidene)-gold[74] for $Au(IMe)_2$ and Au(IMe).

In the fourth section, modeling (MM+ geometry optimization) of the Cyclosporin A on Cu(111) was performed by using the commercial package HyperChem (Hypercube Inc., 1115 NW 4th Street, Gainesville, Florida 32601, U.S.A.)

# 3. Results

## 3.1 Tetraketone and tetraamine modules on three coinage metal surfaces: Phase transformations with temperature, stoichiometry and substrate

Since the discovery of fullerenes in 1985,[75] there has been an intense effort in exploring low dimensional conjugated carbon materials and tapping the full potential of their properties. More recently, graphene related materials, in particular graphene nanoribbons doped with heteroatoms,[36-40] have been the focus of intensive research, as the introduction of nitrogen atoms (N-doping) can be used to tailor their electronic structure,[41] which is an essential requirement for the development of future organic electronics based on graphene circuits. These materials also provide electrochemically-active systems with properties useful for rechargeable batteries and fuel cells and the tunable and exceptionally high light absorption in the visible makes them promising candidates as absorber layers in organic photovoltaics.[76] However, the exploration of potential pathways for the targeted design of such nanostructured devices still needs intense investigations to progress from being a purely academic playground to ensuring technological impact of low dimensional graphene based materials.

Pyrene-fused pyrazaacenes[77] (PPAs) are among this type of nitrogenated ribbon-like structures (**Scheme 3.1**c). Besides their tunable optoelectronic properties, PPAs have shown a very high stability, which makes them an ideal platform to develop narrow one-dimensional materials. PPA-based oligomers[78-83] (with up to 16 linearly-fused aromatic rings) and polymers[84-86] have been synthesized through solution based methods by means of imine-type cyclocondensations (**Scheme 3.1**b).

**Scheme 3.1.** (a) Condensation of a ketone and an amine. (b) Cyclocondensation reaction of diketone and diamine. (c) Cyclocondensation reaction of the tetraketone and the tetraamine molecules employed here into PPAs.

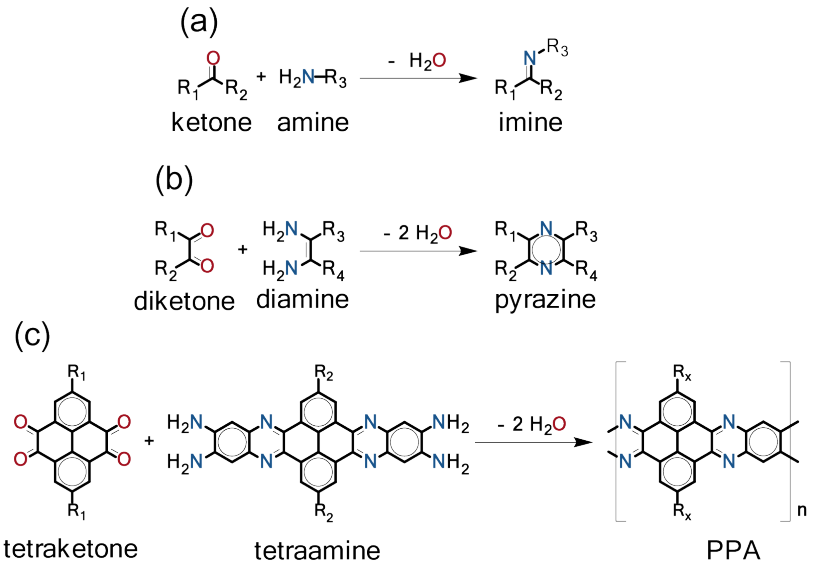


Nevertheless, PPAs are very insoluble materials with a great tendency to aggregate, which hampers their synthesis and characterization. Therefore, on-surface synthetic methods provide not only an alternative aggregation-free environment for producing PPAs but also for characterizing their structure with submolecular resolution, allowing the identification and study of intermediates and defects.

Schiff base (imine) formations (**Scheme 3.1**a) have been successfully implemented for low dimensional structures in solid-liquid interfaces.[16-18,87-91] Imine formation under these conditions has a dynamic character which relies on the reversibility of the relevant covalent bonds under thermodynamic control.[92] Therefore this type of bonding combines the increased stability of covalent bonds with the potential of producing regular superstructures, due to its dynamic character. These characteristics place it among the most promising routes for covalent molecular architectonics, and imines have been demonstrated to form under vacuum conditions as well.[14,15,93] Specifically, an aldehyde and octylamine on Au(111) surfaces form the imine product readily at room temperature (RT),[14] whereas cyclocondensation reactions (**Scheme 3.1**b) have been reported for thick films of suitable diamine and diketone molecules at temperatures above ~ 373 K.[93]

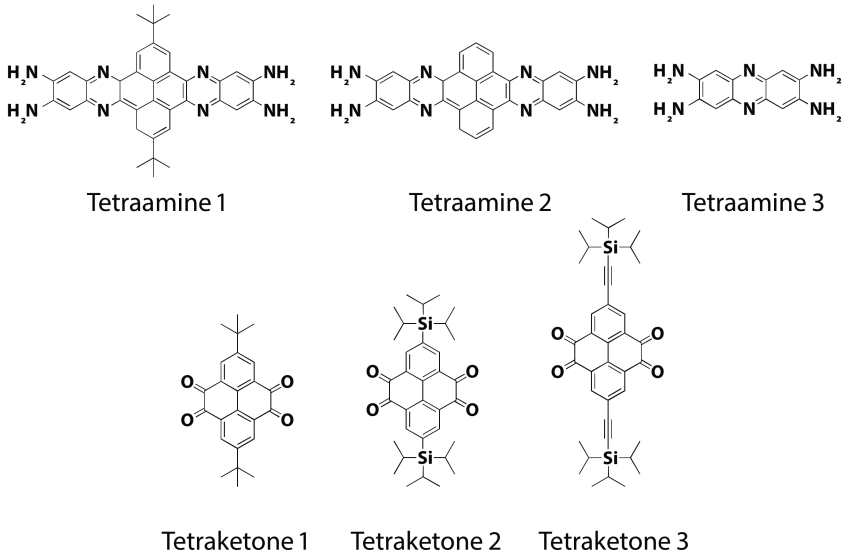


**Figure 3.1:** The molecules investigated in this section.

The study presented in this chapter, which has been published in part previously,[94] provides a systematic investigation of tetraketone and tetraamine molecules aiming to trigger the stated imine formation reaction. Here, we employed several compounds (shown in **Figure 3.1**) for the *in situ* formation of PPAs (**Scheme 3.1**c), and studied the behavior of the different molecules as a function of annealing temperature on three different coinage metal surfaces: Ag(111), Au(111), and Cu(111) in ultrahigh vacuum (UHV) conditions. These differ in the $R_1$, $R_2$ substituents (**Scheme 3.1**) in an attempt to tune the distance from the substrate by introducing more or less bulky groups. STM experiments show clearly different phase transformations during thermal treatment, while XPS measurements provide information about the changes of molecular chemical structures.

### 3.1.1 Tetraketone 1 and tetraamine 1 on three coinage metal substrates

Firstly, we studied the self-assembly of 2,7-di-*tert*-butyl-pyrene-4,5,9,10-tetraketone (tetraketone 1) and 2,11-di-*tert*-butylquinoxalino[2',3':9,10]phenanthro[4,5-*abc*]phenazine-6,7,15,16-tetraamine (tetraamine 1) and the potential of triggering this imine formation reaction on three different substrates.

#### 3.1.1.1 Tetraketone 1 and tetraamine 1 on the Ag(111) substrate

Initially the STM appearance of the monomers employed and their thermal chemistry was established by dosing tetraketone 1 and tetraamine 1 molecules separately on the Ag(111) surface. **Figure 3.2**a shows a representative STM image zooming in a densely packed island of tetraketones, from which we can identify the molecules lying with their π-bonded

moieties nearly parallel to the surface. An individual tetraketone 1 molecule is outlined in black. The contrast is dominated by the physically protruding *tert*-butyl groups that are imaged as bright lobes, whereas the molecular backbone is resolved more faintly. The unit cell has sides of 0.87 nm and 1.60 nm ± 0.1 nm with an angle of 60° between them. **Figure 3.2**c depicts two adjacent tetraketone 1 molecules, superposed with the proposed molecular ball-and-stick models. The H-bond interactions between -C=O and hydrogen on phenyl groups stabilized this arrangement, which are highlighted in green ellipses. The tetraamine 1 molecule has a different π conjugated system, which is imaged in the STM topographical images as a faint ellipse between the two *tert*-butyl bright protrusions (**Figure 3.2**d).

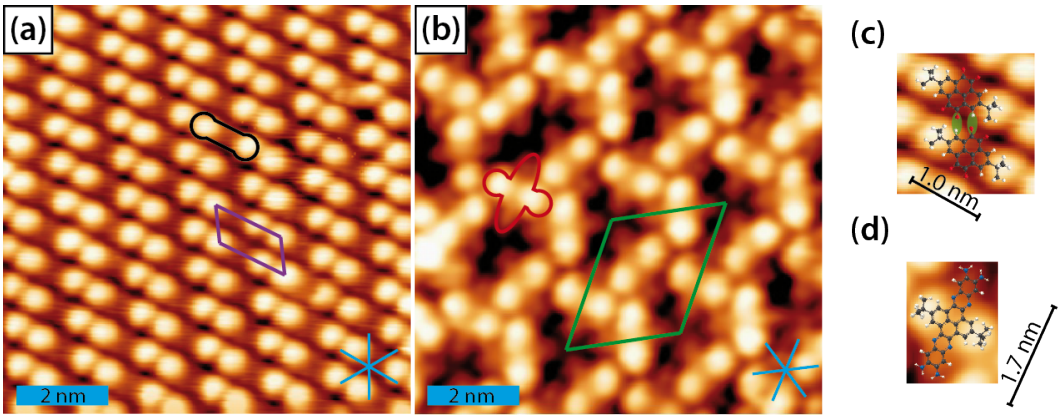


**Figure 3.2:** STM topography of tetraketone 1 and tetraamine 1 molecules on Ag(111) substrate after deposition at RT. The blue lines indicate the high symmetry axes of the substrate. In (a-b) single tetraketone 1 and single tetraamine 1 molecules are outlined in black and red, respectively. The unit cells are marked in purple and green, respectively. (a) STM image of densely packed tetraketone 1 molecules ($T_{STM}$ ~ 170 K, $U_s$ = 1.25 V, $I_t$ = 0.16 nA). (b) Self-assembly of tetraamine 1 molecules ($T_{STM}$ ~ 110 K, $U_s$ = 1.54 V, $I_t$ = 0.11 nA).[95] (c-d) Zoom in STM images (c: tetraketone 1, d: tetraamine 1) overlaid with corresponding ball-and-stick models. In (c) two adjacent tetraketone 1 molecules were selected to reveal H-bond interactions highlighted in green oval shapes.

In **Figure 3.2**b one can clearly identify tetraamine 1 molecules clustered together, their faint rod like backbones orientated along the high symmetry directions of the substrate. The unit cell has sides of 2.52 nm and 3.00 nm ± 0.1 nm with an angle of 60° between them. STM investigations of the tetraamine 1 show molecules only within these intricate molecular arrangements, which appeared after RT deposition and were maintained up to annealing temperatures as high as 530 K.

Complementary XPS measurements provide more information changes of the chemical state during this annealing process. **Figure 3.3** shows the N 1s and C 1s XP spectra of the tetraamine 1 adsorbed on Ag(111) at RT and after annealing treatment (510 K).

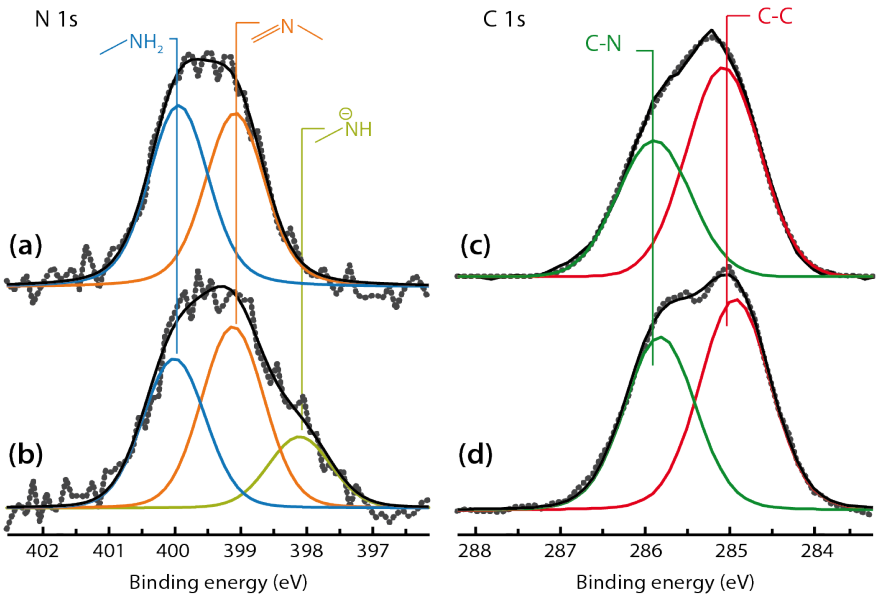


**Figure 3.3:** XP spectra of the N 1s and C 1s core levels of a submonolayer coverage of tetraamine 1 on Ag(111) after RT deposition (a, c), and after annealing to 510 K (b, d). A photon energy of 550 eV and 435 eV was used for the acquisition of N 1s and C 1s, respectively.

The C 1s spectrum of the tetraamine 1 after RT deposition was deconvoluted into two peaks with an intensity ratio of 1 : 2 in agreement with the elemental ratio of C linked to N : C linked to C. The N 1s spectrum of the tetraamine after RT deposition shows two components of similar intensity, one centered at a binding energy of 400.1 ± 0.1 eV due to the primary aminic N (-C-$NH_2$)[96] and the other centered at a binding energy of 398.9 ± 0.1 eV attributed to iminic N (-C=N-C=).[97,98] Conversely, after annealing to 420 K the deconvolution of the spectrum shows three components (**Figure 3.3**b). In addition to the aminic and the iminic N, a weaker peak appears at 397.8 ± 0.1 eV, associated with the presence of –N-H.[98,99]

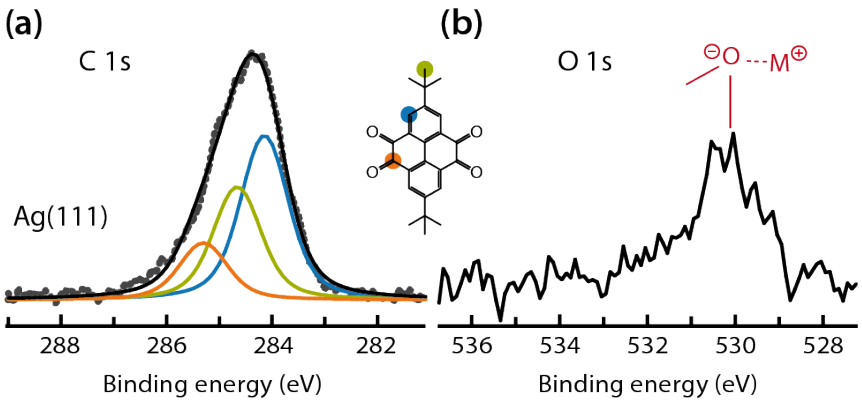


**Figure 3.4:** XP spectra of the C 1s (a) and O 1s (b) core levels, corresponding to a submonolayer coverage of tetraketone 1 on Ag(111) after RT deposition. In the C 1s signal three different contributions can be resolved. The corresponding peaks are colored as the respective C atoms in the molecular model. All spectra were acquired using monochromatized Al Kα radiation.

Furthermore the adsorption of the tetraketone 1 molecules was studied by XPS on Ag(111); the corresponding C 1s and O 1s XP spectra are shown in **Figure 3.4**. The O 1s spectrum displays a single peak centered at a binding energy of 530.2 eV, which is ascribed to hybridization of the C=O group with the substrate metal states ($-C-O^{-}\cdots M^{+}$).[100] This hybridization is presumably to be associated with the formation of an extended π-conjugated system that is strongly coupled to the metal states.

The C 1s spectrum shows three contributions with a ratio of approximately 3:2:1. The peak centered at a binding energy of 284.1 eV is attributed to the presence of aromatic carbon atoms.[101,102] Another peak at a binding energy of 284.6 eV is corresponding to aliphatic carbon atoms.[102,103] The peak contributed by the carbonylic carbon atoms should appear at a binding energy of about 286.9 eV,[100,104] but in our case, the third peak related to carbon atoms bonded to oxygen is shifted to lower binding energy by ~ 1.8 eV, further confirming that the bond of these carbon atoms to oxygen is significantly weaker than in carbonyl moieties.

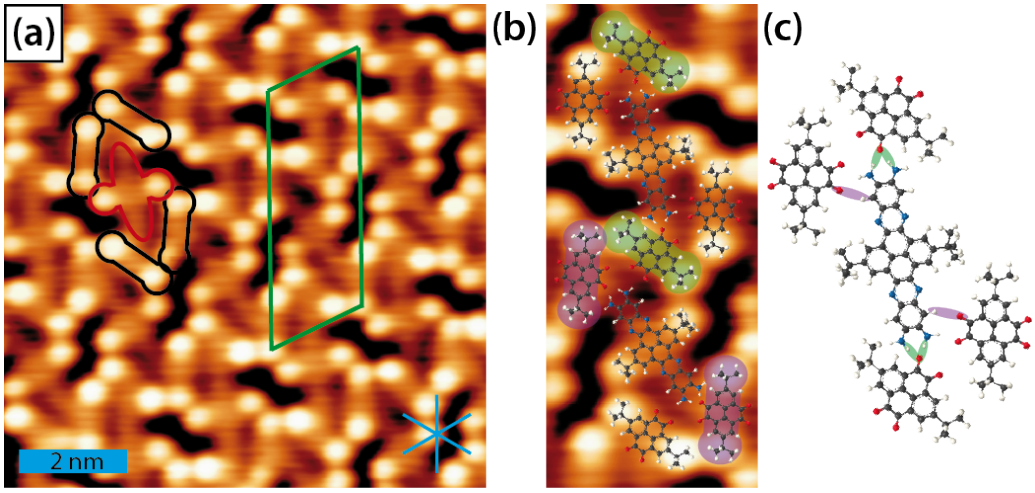


**Figure 3.5:** (a) 2-D nanostructures of tetraketone 1 intermixed with tetraamine 1 ($T_{STM}$ ~ 160 K, $U_s$ = 2.89 V, $I_t$ = 0.12 nA). Single tetraketone 1 and single tetraamine 1 molecules are outlined in black and red, respectively. The unit cell is indicated in green. (b) Zoom in STM image of the mixture of tetraketone 1 and tetraamine 1 overlaid with corresponding ball-and-stick models.[95] (c) Illustration showing different intermolecular H-bonds stabilizing this self-assembly.

In order to promote the cyclocondensation reactions, submonolayer coverages of tetraketone 1 and tetraamine 1 molecules were deposited onto the Ag(111) surface at RT and subsequently annealed gradually to 510 K. At room temperature, the two molecules readily intermix in regular bimolecular assemblies (**Figure 3.5**), so that one tetraamine is surrounded by four tetraketones and stabilized by intermolecular H-bond interactions. Single tetraamine 1 and tetraketone 1 molecules are outlined in red and black, respectively. From this image we can identify the molecular orientation relative to the Ag(111) plane. Both π conjugated systems are lying nearly parallel to the surface as no asymmetry is evidenced in its apparent height along the Ag [1$\bar{2}$1].

This configuration is observed even after annealing up to 510 K. The two molecules arrange in a well ordered zigzag conformation on the silver surface, having a unit cell containing one tetraamine and two tetraketone molecules, with sides of 1.86 nm and 4.75 nm ± 0.1 nm and an angle of 60° between them. **Figure 3.5**b shows the magnified image with superimposed molecular models, from which we can figure out that the orientation of central tetraamine is duplicated every two rows because of the inequivalent interaction between one tetraamine and surrounding four tetraamine molecules. In the top row, the central tetraamine is close to the tetraketone located right above and left below, highlighted by green molecular outlines. Due to the deviation of the self-assembly of the molecules, the next tetraamine in the bottom row is slightly rotated towards the upper left and lower right

tetraketone, highlighted by purple molecular outlines, which are not so closely attracted by tetraamine in the adjacent rows. **Figure 3.5**c gives us an intuitive explanation about the deviation of the formation. The central tetraamine has two H-bond interactions between amines and ketones, indicated in green ellipes, which are much stronger than the side H-bond interaction between ketone and hydrogen of the phenyl groups, highlighted in purple. This inequivalent intermolecular interaction results in the deviation of the assembly.

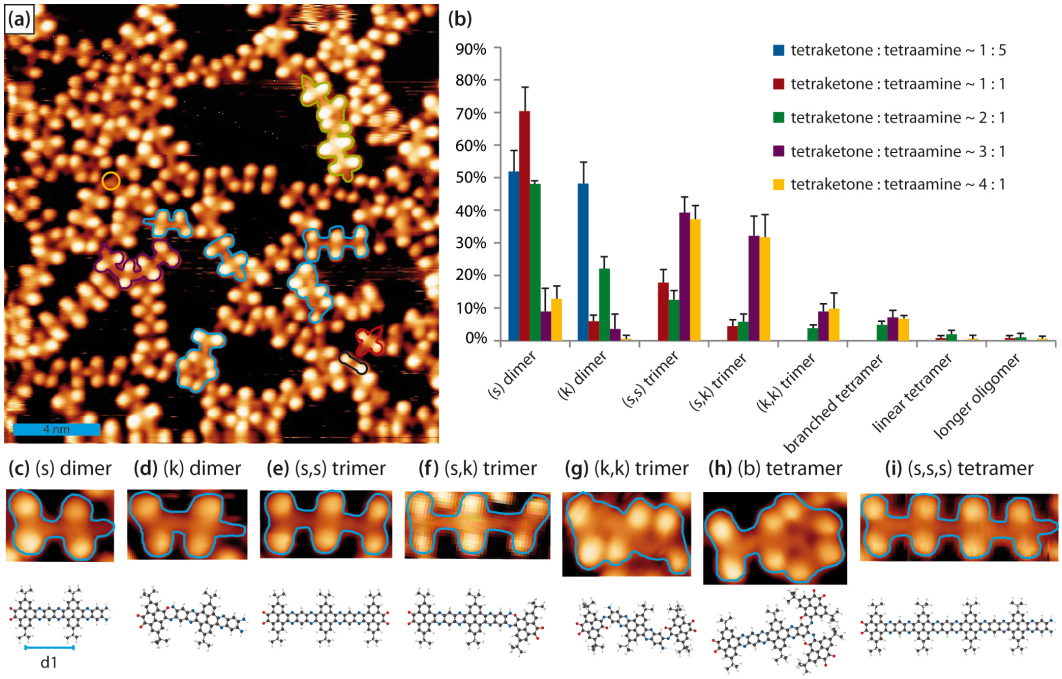


**Figure 3.6:** Condensation products of tetraketone 1 and tetraamine 1. (a) Overview of imine formation reactions on Ag(111) after annealing to 510 K with a stoichiometry of tetraketone 1 to tetraamine 1 ~ 2:1 ($T_{STM}$ = RT, $U_s$ = 2.22 V, $I_t$ = 0.09 nA). (b) Histogram of different oligomers generated after annealing to 510 K as a function of the molecular ratio of tetraketone 1 to tetraamine 1. (c-i) STM images and molecular models of the main types of oligomers resolved after annealing.

In addition, after this treatment, different kinds of oligomers furnish the surface. **Figure 3.6**a shows an overview in which we can discern some distinct oligomers, for instance, a straight (s) dimer, a bent (k) dimer, a straight (s,s) trimer, a bent (k,k) trimer, and a branched (b) tetramer, whose boundaries are outlined by blue solid lines. Here (s) and (k) denote a straight connection between the monomers and a kink in the connection, respectively. Furthermore, one pentamer (outlined in green in **Figure 3.6**a) can be observed, in which two (s) dimers are coupled with one tetraamine. Apart from these oligomers, there are still unreacted monomers (see molecules outlined by black and red lines in **Figure 3.6**a). Some undesired side reaction appears between free terminal amines, which fused together after

this annealing treatment as highlighted by yellow circle; the amine groups from two (s) dimers and a (k) dimer appear linked altogether. Overall, the surface is dominated by dimers and trimers (see also **Figure 3.6**b). However, trimers terminated with diamine moieties are statistically insignificant, a point to which we will return later.

The STM data and molecular models in **Figure 3.6**c-i give a simplified classification of the occurring oligomers. Due to its linear shape and the distance between its *tert*-butyl groups (marked as d1 in **Figure 3.6**c), which was measured to be approximately 1.08 nm, the dimer labeled (s) is assigned to the product of the desired cyclocondensation. In contrast, the (k) dimer assumes a kinked conformation, presumably because only one ketone reacted with one amine to form a single imine. This dimer has two different conformations: the one that allows the ketone moiety to have an intermolecular interaction with the neighboring amine moiety (shown in **Figure 3.6**d), and one that does not (shown in **Figure 3.7**).

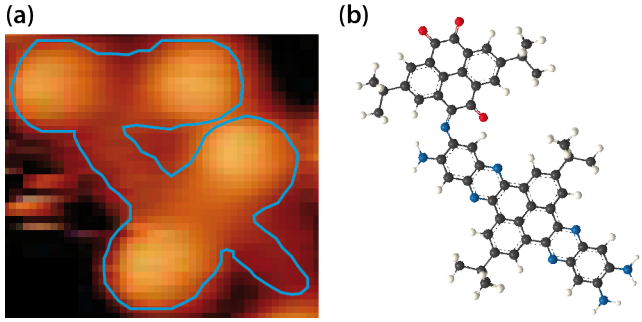


**Figure 3.7:** Second conformation of the (k) dimer. (a) STM image ($T_{STM}$ = RT, $U_s$ = 2.22 V, $I_t$ = 0.09 nA). (b) Molecular model.

**Figure 3.6**e-g categorizes the types of trimers based on the number of cyclocondensations and single imine formations, similar to the categorization of the dimers. For example, (k,k) has two kinks, where both the tetraketone molecule moieties are tilted relatively to the central tetraamine molecule and every tetraketone was linked by a single imine with each side of tetraamine. The tetramers are divided in two types: those that are branched (**Figure 3.6**h), where one tetraamine is surrounded by three tetraketones; and those that are linear, in which two tetraketones alternately link with two tetraamines. In addition to the illustrated (s,s,s) tetramer in **Figure 3.6**i, linear tetramers containing single imines instead of pyrazine rings existed, similar to those found in the (k) dimer and in (s,k) and (k,k) trimers. For example, a (s,k,k) tetramer is outlined in purple in **Figure 3.6**a.

To investigate the effect of stoichiometry, we tuned the tetraketone 1 to tetraamine 1 ratio from ~ 1 : 5 to ~ 4 : 1. The distribution of different oligomer species as a function of stoichiometry is shown in **Figure 3.6**b. From that we can infer the following: Firstly, we note that in the same oligomer category, and for every investigated stoichiometry, the straight type is more probable than the corresponding bent-type. This effect is more pronounced for dimers but can also be distinguished for the longer oligomers. It indicates that the cyclocondensation is preferred to the single imine formation, albeit with less selectivity the longer the oligomer. This selectivity could originate in the ring closure (Scheme 3.1b) being a sequential reaction of 1 + 1 imine formation reaction, in which the product with the single imine (Scheme 3.1a) is a stable intermediate. It is important to note that this type of ketoimine intermediates obtained from *o*-phenylenediamines have not been isolated from solution-based synthetic methods. Secondly, we observed that increasing the proportion of tetraketone molecules increased the yield of trimers. On a surface with an excess of tetraamine molecules, all the tetraketone molecules reacted to form dimers (blue histogram in **Figure 3.6**b), but no longer oligomers were observed. Initially, the formation of dimers seems to be the favorable product at the annealing temperature of 510 K, however, especially in the presence of excess of tetraketone, we observed that the same treatment results in the addition of the tetraketone monomers to the dimer amine side. The yield of the tetraamine modules within the oligomers at 1 : 1, 2 : 1, 3 : 1 and 4 : 1 (tetraketone : tetraamine) stoichiometry was 35%, 54%, 60%, and 69%, respectively, whereas the percentage of amine to imine conversion is 20%, 29%, 47%, and 54%, respectively; *i.e.*, as the relative amount of tetraketone increases, both the amount of (partially) reacted tetraamine molecules and the amount of formed imines increase. In all the cases, there is a limited number of terminal amines in the polymers, showing that the condensation of an amine module (or oligomer) with a diketone terminated oligomer is unfavorable.

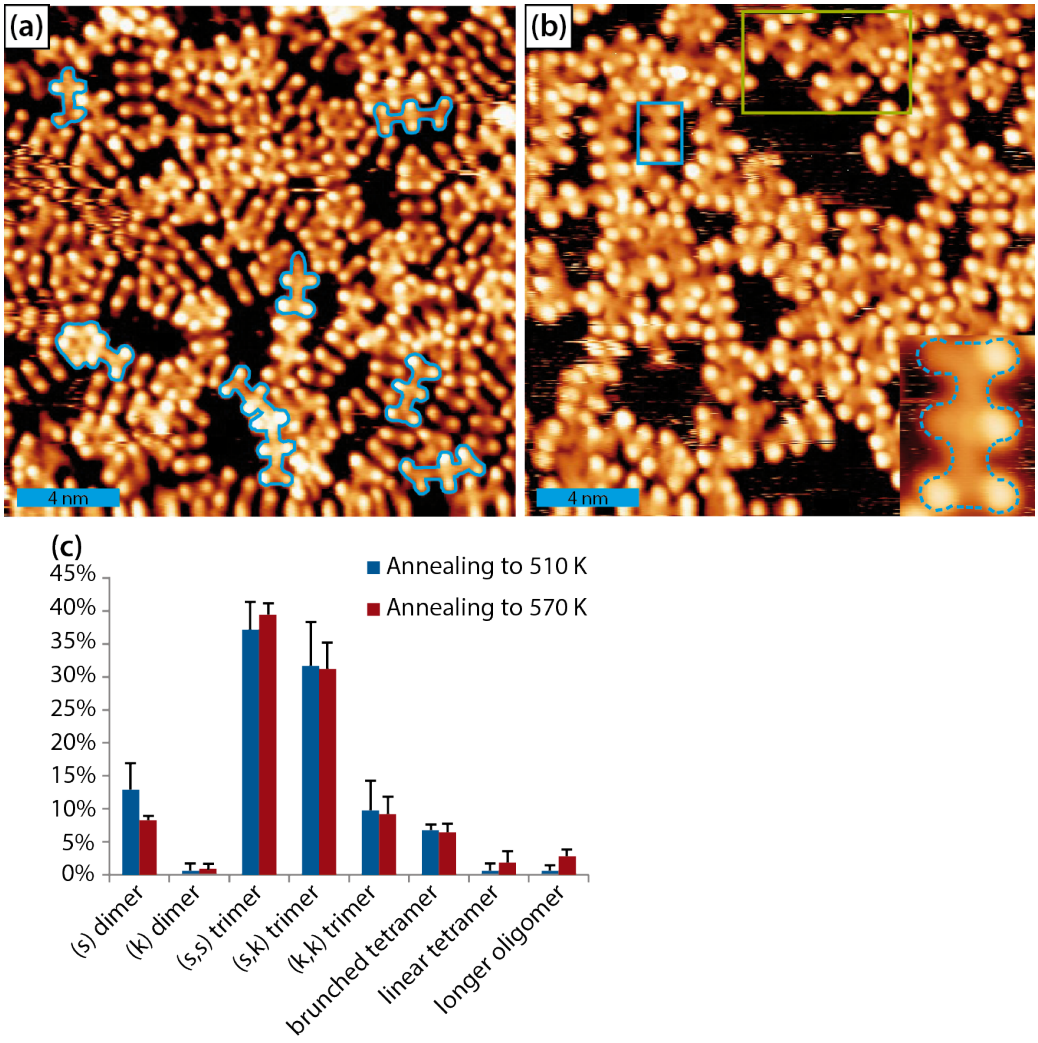


**Figure 3.8:** Effect of annealing temperature on the polymerization process. (a) STM image showing condensation products after dosing tetraketone 1 and tetraamine 1 in ~ 4 : 1 stoichiometry and then annealing to 510 K ($T_{STM}$ = RT, $U_s$ = 1.54 V, $I_t$ = 0.03 nA). (b) Overview of this surface after further annealing to 570 K ($T_{STM}$ = RT, $U_s$ = 1.24 V, $I_t$ = 0.12 nA). The inset displays a magnified image of the blue box with a straight trimer with two partially decomposed *tert*-butyl groups outlined by a dashed blue line. (c) Distribution of different oligomer species as a function of annealing temperature.

Furthermore, we investigated the influence of the annealing temperature on the polymerization process. **Figure 3.8**a reveals the condensation products after dosing tetraketone 1 and tetraamine 1 molecules in a ~ 4 : 1 stoichiometry and then annealing to 510 K. We can distinguish the two types of dimers, the three kinds of trimers, the branched tetramer, and a bent (s,s,k,s) pentamer (highlighted by blue solid lines). Subsequent further annealing to 570 K desorbed most of the unreacted tetraketone and modestly promoted lengthening of the oligomers, as illustrated in **Figure 3.8**. This is also reflected on the percentage of tetraamine molecules incorporated into oligomers, which increased from 69% to 79% after this higher temperature annealing.

The histogram in **Figure 3.8**c presents the trend of oligomer formation with the annealing temperature. By inspection we can deduce that part of (s) dimer reacted with the available tetraketone, forming trimers, especially straight (s,s) trimers. This heat treatment also affected a significant portion of the *tert*-butyl groups. This is illustrated by the straight trimer outlined in blue in the inset of **Figure 3.8**b, where two *tert*-butyl groups are resolved faintly in comparison with the intact ones. In some areas (example shown in the green box in **Figure 3.8**b), the molecular decomposition prevents us from identifying the molecular shape. With increased annealing temperature, more tetraketone molecules desorbed from the surface limiting the elongation of the polymers. We therefore corroborate our earlier conclusion that longer oligomers require a second stage, higher temperature annealing. In this situation, no excess of tetraketone is left on the surface but it is still possible to condense dimers and trimers into forming longer oligomers (n=5) and/or to condense tetraamine monomers to existing oligomers.

The annealing temperatures required for the cyclocondensation reaction on Ag (510 K) are significantly higher than the ones reported for similar cyclocondensation reactions on thick molecular films under vacuum (373 K),[93] as well as in solution (~ 323-453 K).[78-83] Accordingly, we dosed molecules in three layers (tetraketone-tetraamine-tetraketone), which turns out to produce a very limited number of dimers at lower temperatures (400 K). After this annealing treatment only molecules in direct contact with the metal surface remained. As no condensation products were observed after annealing a submonolayer of tetraketone 1 and tetraamine 1 molecules to 400 K, we can conclude that the condensation reaction requires much lower thermal energy in the case that the two reacting modules are not confined in the two dimensional geometry imposed when they are adsorbed on the metal surface. Indeed, on the Ag(111) surface the reaction seems to proceed at the temperature of the onset of desorption of the tetraketone molecule. It is estimated by STM images that annealing to 510 K causes a 10-20% loss of the surface tetraketone molecules. No decrease in coverage was observed for the tetraamine molecules under the same conditions, thus implying that they are more strongly bound to the Ag(111) surface.

**Scheme 3.2.** Mechanism of imine formation in solution. B= base

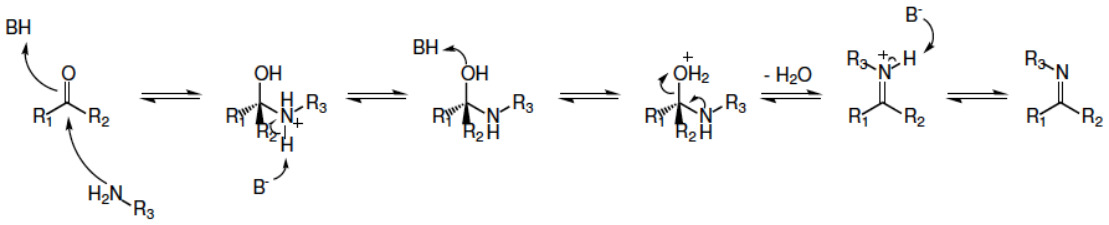


Assuming that the reaction needs a non-planar intermediate, as expected for the classical imine formation between a ketone and an amine shown in Scheme 3.2, this would require a lift-off of the π-conjugated backbone from the surface. (We note that in contrast to the reaction in solution, on Ag(111) and Cu(111) we might reasonably expect that no additional base is required, as the surface itself can abstract protons from the molecular moieties.[105,106]) In fact, this assumption would justify why diamine terminated oligomers longer than dimers rarely form and why the polymerization is limited: the tetraketone π-conjugated backbone is the easiest to lift-off from the surface, whereas more extended modules adsorb more strongly on the surface. More than 98% of all *s* or *k* joints observed after annealing at 510 K can be accounted for with the addition of a tetraketone monomer to a longer module.

To explore the effect of the underlying metal surface we also investigated this reaction on gold and copper. The details are discussed in the following.

### 3.1.1.2 Tetraketone 1 and tetraamine 1 on the Au(111) substrate

On the Au(111) substrate, individual tetraketone 1 and tetraamine 1 molecules form a similar self-assembly as that on Ag(111). When mixed together in a stoichiometry of 6 : 1 and subsequently annealed to 360 K, different domains appeared, which remained after annealing to 380 K.

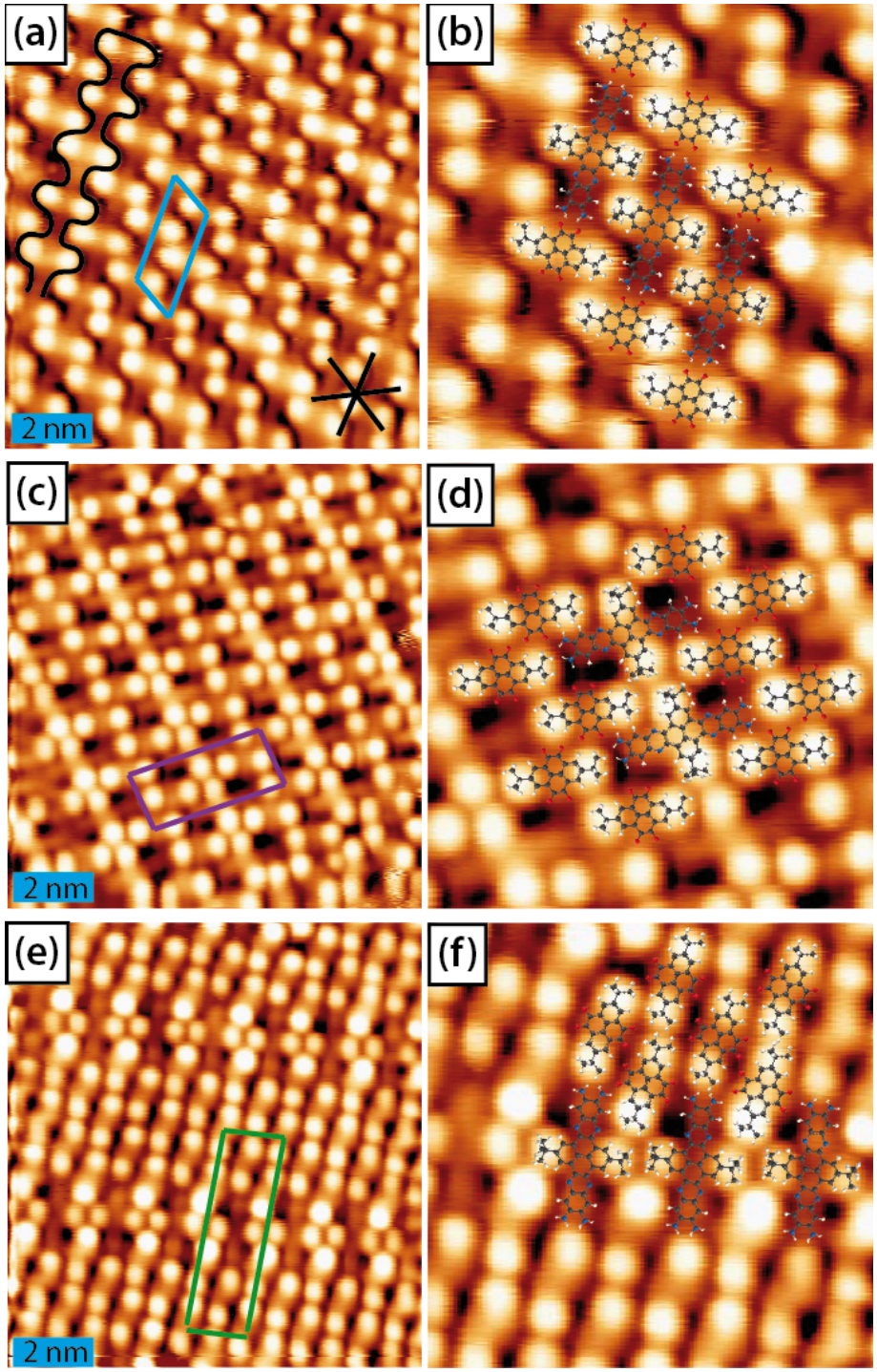


**Figure 3.9:** Different self-assembly of tetraketone 1 and tetraamine 1 on Au(111) after annealing to 380 K recorded at room temperature. (a, b) Linearly packed polymer-like structure ($U_s$ = 1.58 V, $I_t$ = 0.11 nA). (c, d) Network-like structure ($U_s$ = 1.58 V, $I_t$ = 0.10 nA). (e, f) Stripe-like structure ($U_s$ = 1.58 V, $I_t$ = 0.10 nA). The unit cells are marked in blue, purple and green, respectively. The black star in (a) indicates the high symmetry axes of the substrate.

**Figure 3.9** depicts several STM images recorded after the aforementioned preparation condition on Au(111). Similarly to what we found on Ag(111), the bright protrusions in the

images are *tert*-butyl groups and the one with faint oval shape between two protrusions is the tetraamine 1 molecule as mentioned before. **Figure 3.9**a shows a densely packed linear polymer-like structure where the tetraketone is linked with the tetraamine by H-bonding between the diketone and diamine groups. The unit cell containing one tetraketone and one tetraamine has sides of 1.25 nm and 2.74 nm ± 0.1 nm with an angle of 60° between them. One molecular chain is highlighted in the black outline in **Figure 3.9**a. We can see that the adjacent molecular chains assemble like zippers. The detailed imaging superposed with molecular models is shown in **Figure 3.9**b. **Figure 3.9** (c-f) depicts a similar arrangement with a difference in the ratio of tetraketone to tetraamine molecules. The ratio of tetraketone to tetraamine in the network-like structure in (c) is 3 : 1, whose unit cell has sides of 1.50 nm and 3.44 nm ± 0.1 nm with an angle of 84° between them. In the arrangement shown in (e), the ratio is 5 : 1 and the unit cell has sides of 1.50 nm and 4.93 nm ± 0.1 nm with an angle of 84° between them.

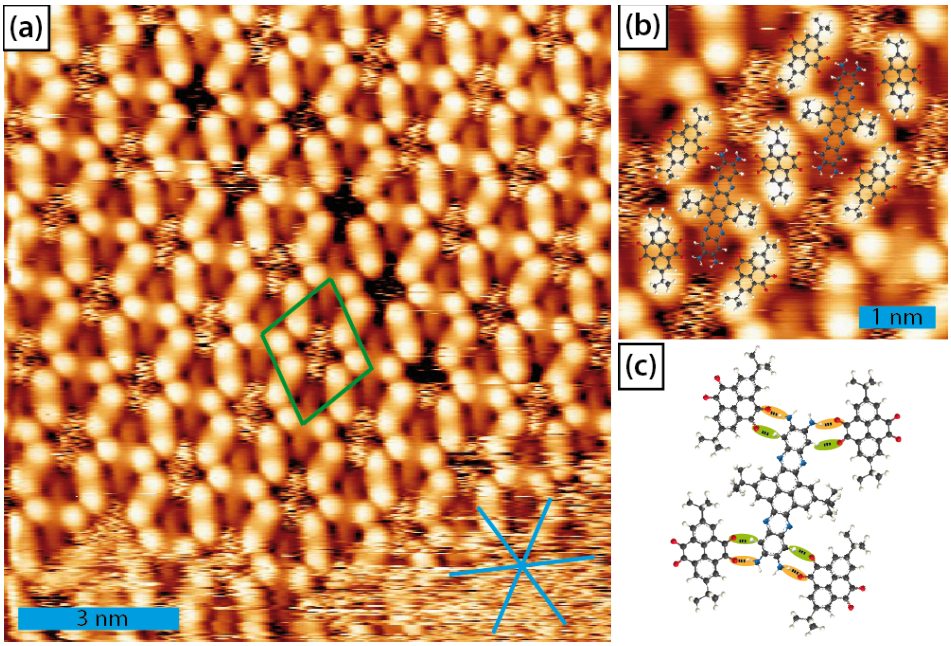


**Figure 3.10:** Self-assembly of tetraketone 1 and tetraamine 1 on Au(111) surface after annealing the sample to 450 K recorded at room temperature. (a) Overview of orderly packed molecules ($U_s$ = 1.58 V, $I_t$ = 0.11 nA). (b) Detailed image of this new domain with superposed molecular models. (c) Illustration showing intermolecular H-bond interactions: H-bond between -C=O and -$NH_2$ indicated in orange, between -C=O and hydrogen on phenyl groups highlighted in green.

After annealing the sample to 450 K, tetraketone 1 desorbed partially and was distributed more evenly with tetraamine 1 in similar arrangements as described in subsection 3.1.1.1. In addition to this, we monitored a new domain illustrated in **Figure 3.10**a that is similar to the

self-assembly of molecules on Ag(111) (in **Figure 3.5**), however this new arrangement is even more ordered and symmetric compared with that. The central tetraamine is no longer inclined to certain tetraketones in adjacent rows. In this circumstance, the unit cell, comprised of one tetraamine with two tetraketone molecules, has sides of 1.86 nm and 1.65 nm ± 0.1 nm with an angle of 76° between them. From **Figure 3.10**c we can figure out the reason for the occurrence of this symmetric arrangement. The central tetraamine has nearly equivalent intermolecular interaction with the surrounding four tetraketones via H-bond interaction between -C=O and -$NH_2$ (indicated in orange in **Figure 3.10**c), as well as between -C=O and hydrogen on phenyl groups (indicated in green in **Figure 3.10**c). This domain survived after annealing the sample to 480 K.

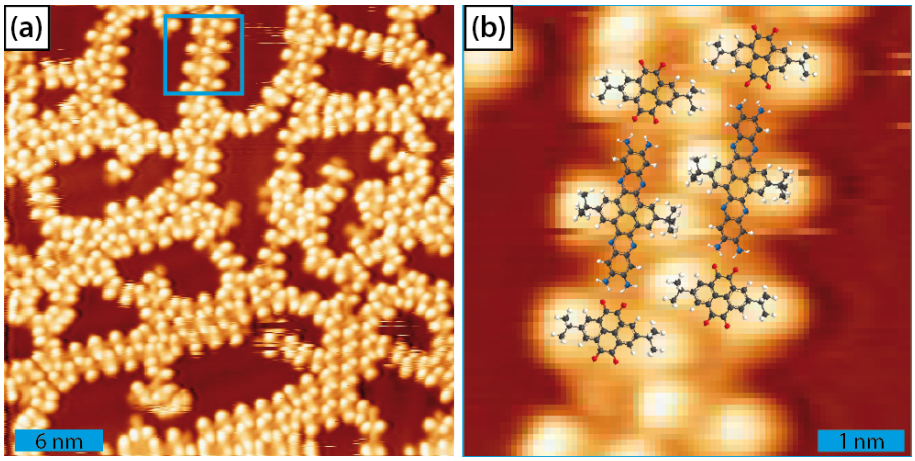


**Figure 3.11:** (a) Overview of the two dimensional network structure of tetraketone 1 and tetraamine 1 on Au(111) after annealing the sample to 510 K ($T_{STM}$ = 95 K, $U_s$ = 1.58 V, $I_t$ = 0.12 nA). (b) Magnified image of the linear polymer-like structure (blue box in (a)) with superposed molecular models.

In the following experiment, we heated the sample to 510 K and scanned at 95 K. It is amazing that most of the excess tetraketone molecules desorbed and only the polymer-like structure left, forming the two-dimensional network arrangement illustrated in **Figure 3.11**a. The molecular chains consist of tetraketone and tetraamine molecules and form long and straight rows that interact with adjacent rows in a zipper-like fashion, similar to the arrangement shown in **Figure 3.9**a. Tetraketone and tetraamine still linked together through H-bond interactions between ketone and amine groups, which is much clearly shown in **Figure 3.11**b. Due to the desorption of the tetraketone molecules, the intact distinctive herringbone Au substrate can be seen again.

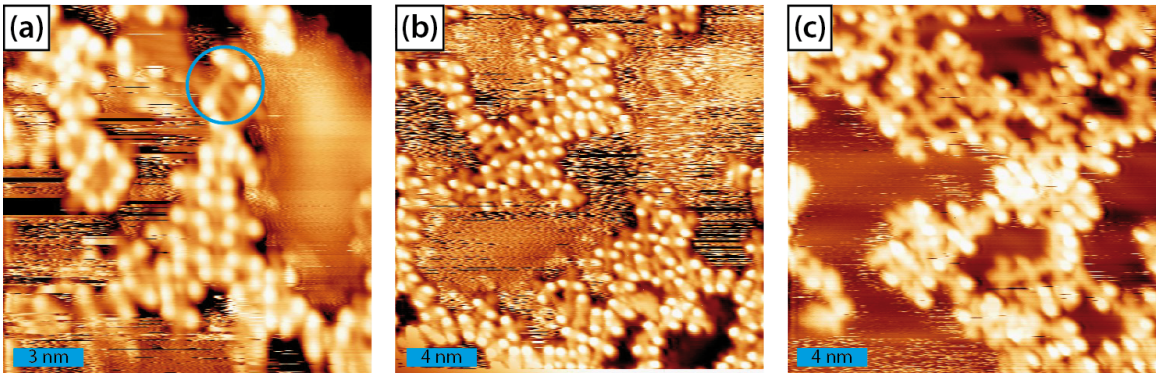


**Figure 3.12:** STM images of the self-assembly of tetraketone 1 with tetraamine 1 on Au(111) as a function of the annealing temperature. (a) After annealing of the sample to 540 K ($T_{STM}$ = RT, $U_s$ = 1.54 V, $I_t$ = 0.11 nA). Most of the tetraketone 1 molecules have desorbed from the Au(111) surface. No products of imine formation could be identified. A blue circle indicates *tert*-butyl groups in tetraamine molecules that have been affected by the annealing and no longer appear as bright as before. (b) After annealing of the sample to 570 K ($T_{STM}$ = RT, $U_s$ = 1.06 V, $I_t$ = 0.15 nA). (c) After annealing of the sample to 640 K ($T_{STM}$ = RT, $U_s$ = 1.58 V, $I_t$ = 0.12 nA). A large portion of the *tert*-butyl groups have been affected by the annealing, no products of ketone-amine condensation could be identified.

We further annealed the sample to 540 K. Inferred from **Figure 3.12**, molecular lines consisting of alternating tetraketone and tetraamine molecules as discussed above still existed albeit shorter. Moreover, as the tetraketone desorbed further, the tetraamine molecules tended to cluster together head to head, and some *tert*-butyl groups were already destroyed, highlighted by the blue circle. After annealing to 640 K, the surface contained almost exclusively tetraamine molecules with numerous *tert*-butyl groups decomposed. And the tetraamines interacted with each other forming covalent bonds.

Concluding from the experimental results above, tetraketone 1 and tetraamine 1 can form symmetric domains on Au(111) surface stabilized by intermolecular H-bond interactions. However, no oligomers formed because a major fraction of tetraketone molecules desorbed from the surface rather than reacted with tetraamine.

### 3.1.1.3 Tetraketone 1 and tetraamine 1 on the Cu(111) substrate

On the Cu(111) substrate, molecules behaved differently compared to the other two crystals. Firstly, we studied the temperature dependent self-assembly of tetraamine 1 on Cu(111).

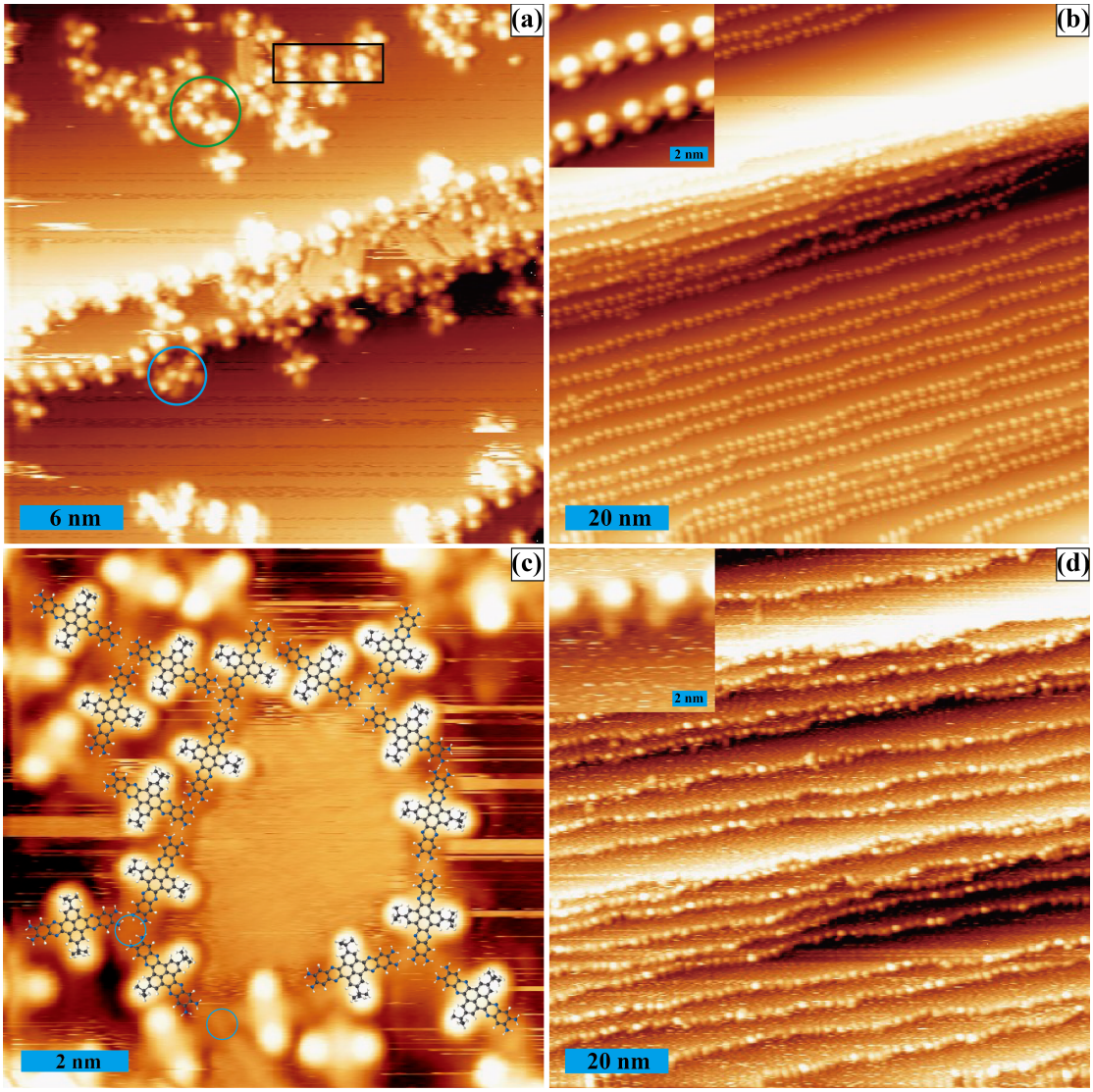


**Figure 3.13:** Self-assembly of tetraamine 1 on Cu(111) as a function of the annealing temperature. (a) STM image of tetraamine 1 deposited on Cu(111) ($T_{STM}$ = 93 K, $U_s$ = -1.36 V, $I_t$ = -0.06 nA). (b) After annealing the sample to 373 K ($T_{STM}$ = 153 K, $U_s$ = 1.74 V, $I_t$ = 0.04 nA), insert ($U_s$ = 1.74 V, $I_t$ = 0.11 nA) shows detailed image. (c) Annealing the sample to 433 K ($T_{STM}$ = 180 K, $U_s$ = 1.40 V, $I_t$ = 0.10 nA). (d) Annealing the sample to 513 K ($T_{STM}$ = 276 K, $U_s$ = 2.02 V, $I_t$ = 0.07 nA), insert ($U_s$ = 2.02 V, $I_t$ = 0.11 nA) illustrates detailed image.

As indicated in **Figure 3.13**a, after dosing tetraamine 1 on Cu(111) with a surface coverage of approx. 25%, tetraamine mainly adsorbed with its conjugated moiety parallel to the step edges in a head to head geometry interacting by H-bonds with diamine groups. On terraces, some tetraamine behaved similarly as on step edges (highlighted in the black box) forming linear molecular chains. A certain amount of tetraamine is visible on the surface side by side (in blue circle) or head to head yet in a non-linear arrangement (in green circle) interacting via intermolecular H-bonds, like the self-assembly on Ag(111) but not as well ordered. On negative bias, the density of molecules increased where we scanned, indicating

that the molecules interact with Cu adatoms induced by the tip.[107-110] After annealing the sample to 373 K, most of the molecules segregated to the step edges, as depicted in **Figure 3.13**b. After further heating the sample to 433 K, the molecules assemble head to head, preferentially in a triangular or rectangular arrangement (**Figure 3.13**c). Although the diamine groups of tetraamine molecules do not overlap with each other when clustered together, as confirmed by superimposing molecular models on the image, there is something in between the diamines, which is probably the coordinating Cu adatoms[111], marked by blue circles. This will be further discussed in combination with the following experiments. The dendritic structure was also mainly found in the vicinity of step edges and the total coverage remained as before. However, after annealing the sample to 513 K, the previous dendritic structure disappeared and the tetraamine adsorbed exclusively to step edges. From **Figure 3.13**d, we can see that the coverage of the tetraamine decreased a bit. Comparing the insert with that of **Figure 3.13**b, we can infer by the contrast of the butyl groups that some *tert*-butyl groups were already affected after this thermal treatment.

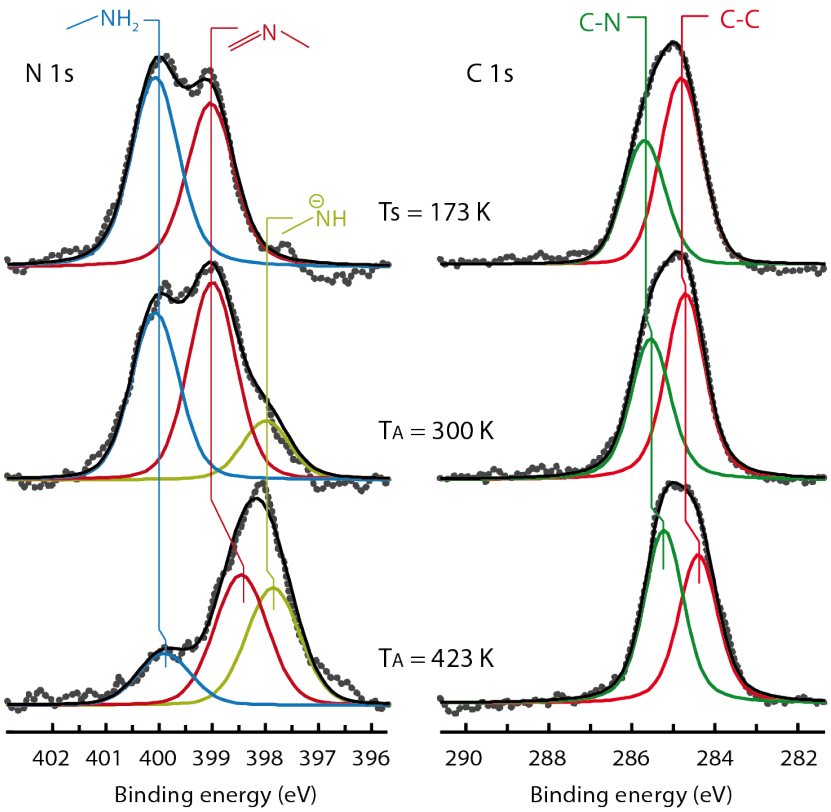


**Figure 3.14:** XP spectra of the N 1s and C 1s core levels of a submonolayer coverage of tetraamine 1 on Cu(111) after deposition at 173 K, and after annealing to 300 K and 423 K.

Supplementary XPS measurements shed light into this structure. The C 1s spectrum of the tetraamine 1 after deposition at 173 K was deconvoluted into two peaks with intensity ratio of 1 : 2 in agreement with the elemental ratio of C linked to N : C linked to C. As discussed above, a peak centered at a binding energy of 400.1 ± 0.1 eV is due to the primary aminic N (-C-$NH_2$)[96] and a peak centered at a binding energy of 398.9 ± 0.1 eV is attributed to iminic N (-C=N-C=).[97,98] In **Figure 3.14**, after deposition of tetraamine 1 on Cu(111) at 173 K, the N 1s spectrum shows these two components of similar intensity. After slight annealing to 300 K, a third peak appears at 397.8 ± 0.1 eV, associated with the presence of –$N^-$H.[98,99] And after further annealing to 423 K, the three peaks all shifted to lower binding energy. So it is deduced that the Cu surface activates the amines by partial dehydrogenation, and then the dehydrogenated amines may coordinate with copper adatoms.[111]

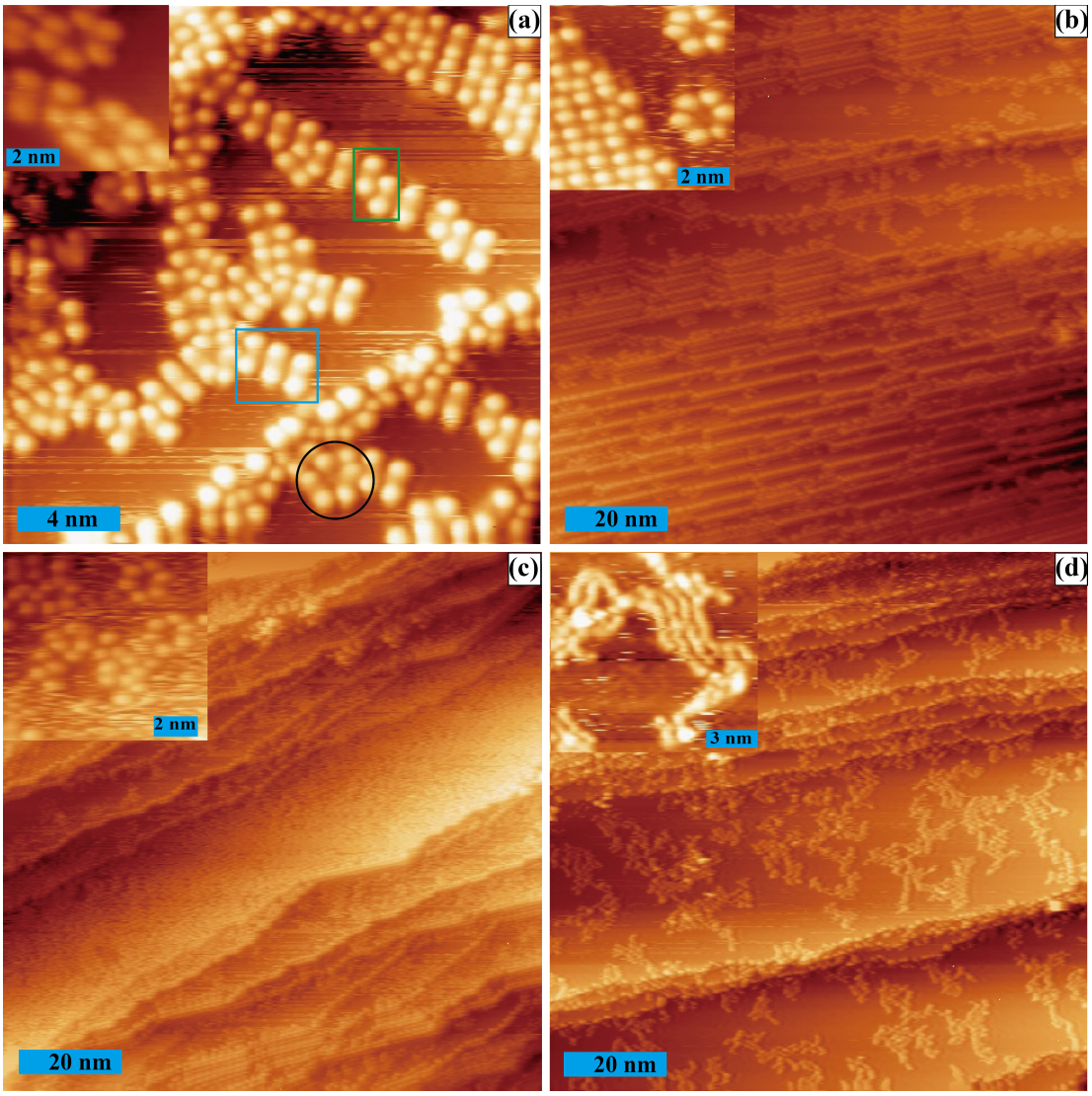


**Figure 3.15:** Self-assembly of tetraketone 1 on the Cu(111) surface as a function of the annealing temperature. (a) STM image of tetraketone 1 deposited on Cu(111) ($T_{STM}$ = 194 K, $U_s$ = 2.02 V, $I_t$ = 0.11 nA), inset ($U_s$ =

1.25 V, $I_t$ = 0.10 nA) shows the flower-like structure. (b) Annealing the sample to 393 K ($T_{STM}$ = RT, $U_s$ = 1.25 V, $I_t$ = 0.06 nA), inset ($U_s$ = 1.24 V, $I_t$ = 0.11 nA) shows a detailed image. (c) Annealing the sample to 423 K ($T_{STM}$ = RT, $U_s$ =1.25 V, $I_t$ = 0.09 nA), inset ($U_s$ = 1.25 V, $I_t$ = 0.12 nA). (d) Annealing the sample to 513 K ($T_{STM}$ = RT, $U_s$ = 1.24 V, $I_t$ = 0.07 nA), inset ($U_s$ = 1.25 V, $I_t$ = 0.10 nA) shows a magnification with details.

Then we investigated the self-assembly of tetraketone 1 on the Cu(111) substrate as a function of the annealing temperature. Apart from a similar arrangement as that on Ag(111) or Au(111) where tetraketone molecules are packed together in zigzag pattern, pictured in **Figure 3.15**a (green box), there occurred several new domains after RT deposition. One is the parallel-arranged region outlined by the blue box and the other one is indicated by the black circle where three tetraketones stabilized with each other forming discrete, well-defined flower-like structures as also shown in the inset. After heating the sample to 373 K, as illustrated in **Figure 3.16**a, the densely packed structure of the tetraketone molecules as in the green box of **Figure 3.15**a dominated, where the adjacent rows are offset and form a zigzag pattern. One can notice that on the border of every densely packed domain, the *tert*-butyl groups without adjacent diketone groups to interact with, appeared a bit brighter (highlighted in blue circles) than the other protrusions. In addition to this, there were still flower-like structures shown in **Figure 3.16**b-c. Inferred from the two consecutively scanned images, indicated by the blue box, the surrounding isolated tetraketone molecules were still mobile and rearrange occasionally to form the trimer flower-like structures.

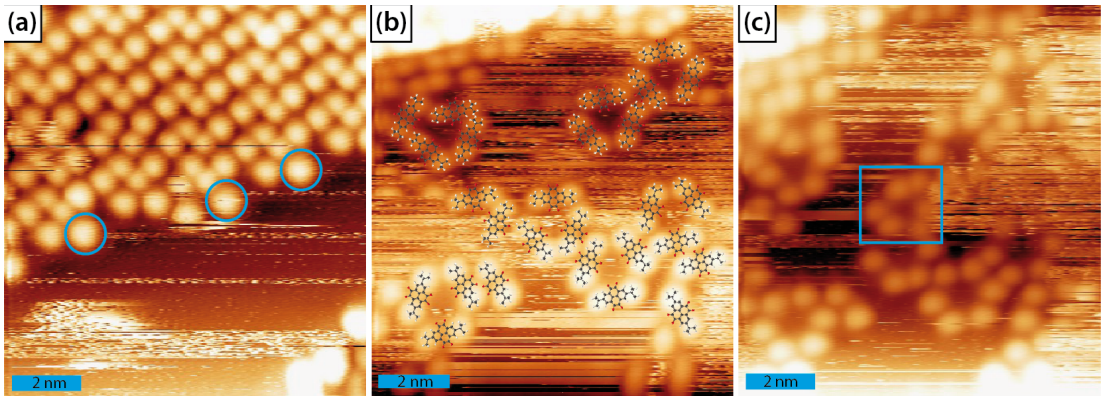


**Figure 3.16:** Self-assembly of tetraketone 1 on Cu(111) surface after annealing the sample to 373 K, recorded at 283 K. (a) Densely packed tetraketone 1 molecules ($U_s$ = 1.25 V, $I_t$ = 0.09 nA). (b) Flower-like structure with superimposed molecular models ($U_s$ = 1.40 V, $I_t$ = 0.12 nA). (c) Dynamic structural rearrangement ($U_s$ = 1.40 V, $I_t$ = 0.09 nA).

Subsequently heating to 393 K, restructuring of the substrate induced by the molecules was observed, as inferred from the orientation of the step edges shown in **Figure 3.15**b. Different from before, tetraketone 1 molecules now situated very orderly and parallel to the

step edges, though on terraces they existed in a similar arrangement, in a densely packed pattern and a flower-like structure, shown in the inset. Further heating the sample to 423 K reduced the amount of densely packed tetraketones. On terraces, mainly flower-like arrangement appeared and scattered molecules that restructured and moved around quickly made the surface appear fuzzy, as indicated in **Figure 3.15**c. There were no big changes except a slight desorption of tetraketone after heating the sample to 443 K and 473 K, however, tetraketone molecules decomposed, polymerized and aggregated after further annealing to 513 K shown in **Figure 3.15**d.

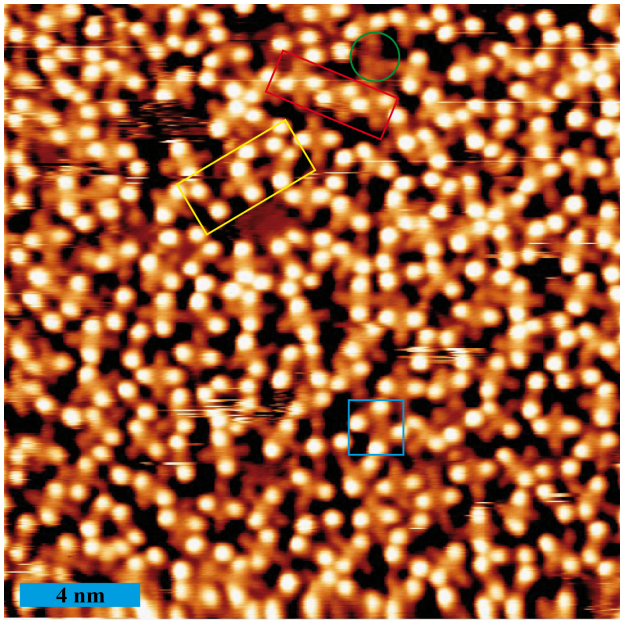


**Figure 3.17:** Self-assembly of tetraketone 1 and tetraamine 1 on Cu(111) as deposited at RT ($T_{STM}$ = 94 K, $U_s$ = 2.02 V, $I_t$ = 0.10 nA).

Then tetraketone 1 and tetraamine 1 were deposited on Cu(111) sequentially, generating a sub-monolayer coverage of organic molecules with a 1 :1 stoichiometry. As indicated in **Figure 3.17**, after deposition, the two molecules intermix on the Cu(111) substrate, from which we can see that the tetraamine still preferred to form a similar zigzag arrangement stabilized by hydrogen bonding between amine and ketone groups like on the Ag(111) substrate highlighted by the yellow box. Similar to what we found with only tetraamine molecules, clustered tetraamine molecules arranged head to head, marked by the green circle and shoulder by shoulder marked by the red box.

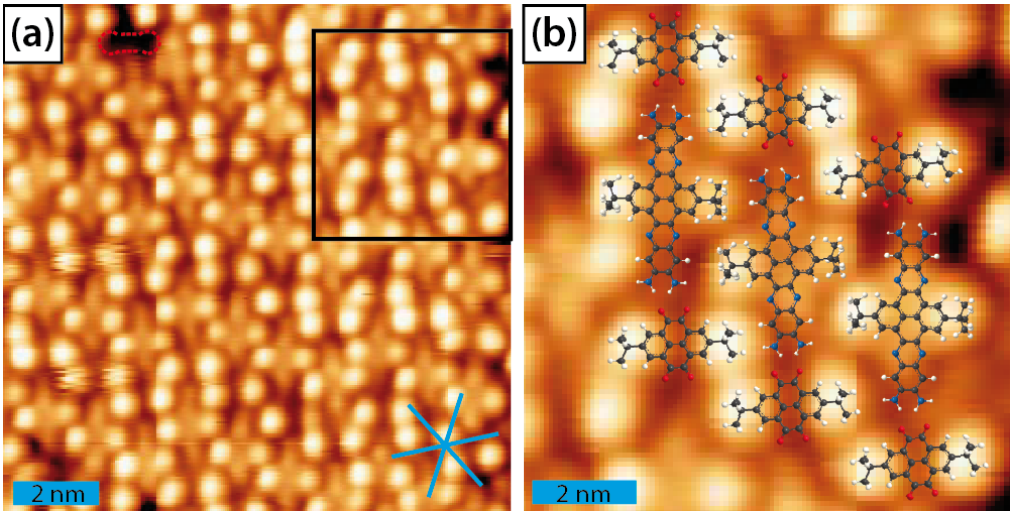


**Figure 3.18:** Self-assembly of tetraketone 1 and tetraamine 1 on the Cu(111) substrate after annealing the sample to 360 K. (a) Polymer-like domain ($T_{STM}$ = 153 K, $U_s$ = 1.90 V, $I_t$ = 0.13 nA). (b) Magnified image of the black box in (a) with superposed molecular models.

After annealing the sample to 360 K for 10 min, we found two kinds of different arrangements, polymer-like and fence-like domains, shown in **Figure 3.18** and **Figure 3.19**, respectively. Actually these arrangements already existed after deposition without heating the surface though not very ordered and only in small areas. The polymer-like domain is stabilized by hydrogen bonds between diamines and diketones. The arrangement had some defects such as missing a certain tetraketone shown by red dashed line in **Figure 3.18**a. Besides, the domain was not so highly ordered as that on Au(111) (**Figure 3.9**a and **Figure 3.11**b). In **Figure 3.18**b we pictured three rows of this polymer-like arrangement to demonstrate the ordering. In the outermost two rows of tetraketone, the bottom left and upper right tetraketone deviated a bit from the normal position and got close to the adjacent tetraketone in the middle column, which is also the reason for different appearance of this domain compared with that on the Au(111) substrate.

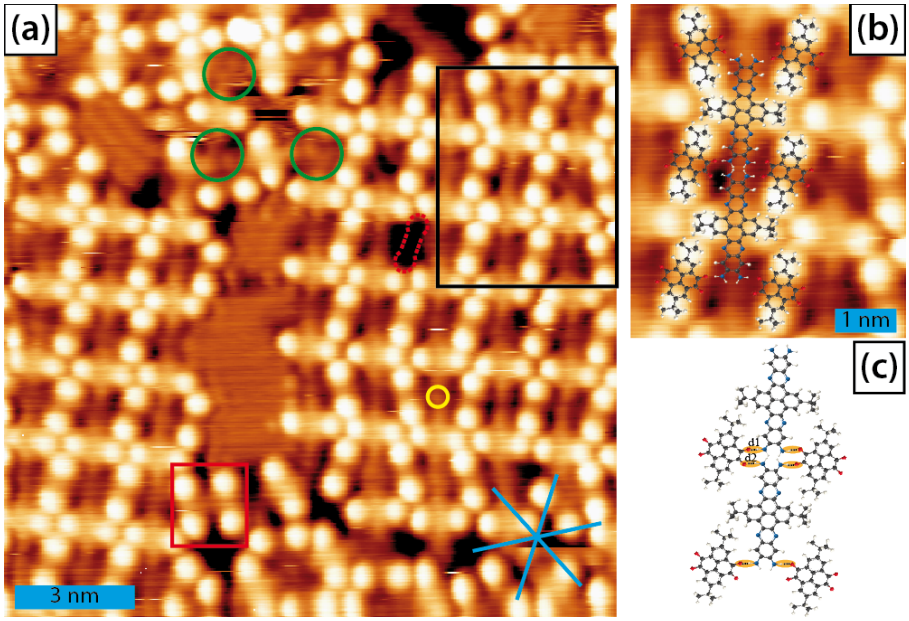


**Figure 3.19:** Self-assembly of tetraketone 1 and tetraamine 1 on Cu(111) after annealing the sample to 460 K. (a) Fence-like domain ($T_{STM}$ = 153 K, $U_s$ = 2.02 V, $I_t$ = 0.11 nA). (b) Magnified image of the black box in (a) with superposed molecular models. (c) Detailed illustration of H-bond interactions.

The fence-like domain is shown in the STM image after annealing the sample to 460 K in **Figure 3.19**a. As we can see there is also a missing tetraketone marked in red dashed line. Besides, in different rows, the orientation of tetraketone molecules adsorbing on the surface was not always consistent. Shown in **Figure 3.19**b, in adjacent rows, tetraamines are linked with each other end to end forming long straight lines. Tetraketones in this network stabilize the arrangement by H-bond interactions between amines and ketones, which is much more obvious in **Figure 3.19**c.

This newly discovered fence-like domain is very interesting. As discussed above in **Figure 3.2**b, on Ag(111), individual tetraamine cluster together head to head. On Cu(111), individual tetraamines also form similar self-assembly shown in **Figure 3.13**c. But after mixing tetraamine with tetraketone and annealing to higher temperature, besides the aforementioned clustering of tetraamine molecules marked in green circles in **Figure 3.19**a, a new phase appeared that is this fence-like domain, where tetraamines linked head to tail forming long straight lines. Tetraamines also seem to coordinate with Cu adatoms highlighted in yellow circle in **Figure 3.19**a.

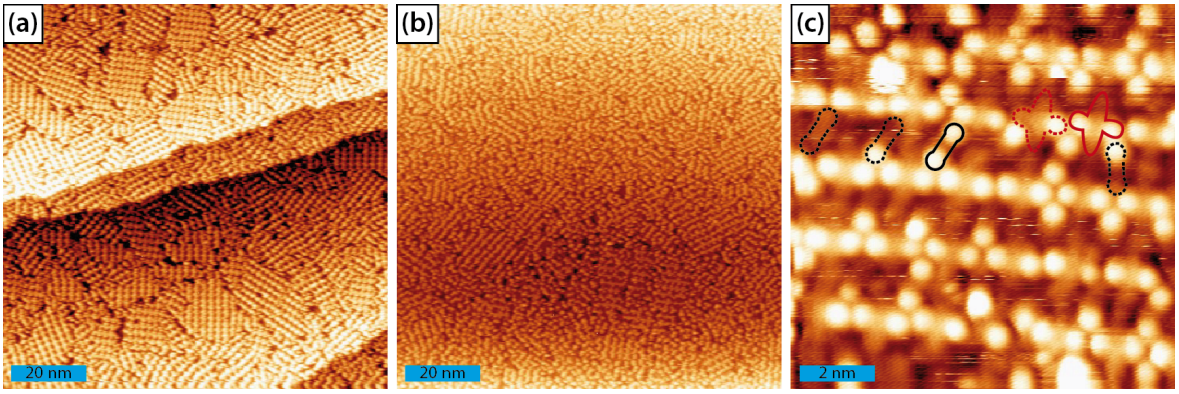


**Figure 3.20:** Self-assembly of tetraketone 1 and tetraamine 1 on Cu(111) as a function of annealing temperature. (a) Overview of mainly fence-like domains after heating the sample to 430 K ($T_{STM}$ = 150 K, $U_s$ = 2.29 V, $I_t$ = 0.10 nA). (b) Overview image after heating the sample to 490 K ($T_{STM}$ = 195 K, $U_s$ = 2.15 V, $I_t$ = 0.07 nA). (c) Detailed image of domain with decomposed molecules after heating the sample to 490 K ($T_{STM}$ = 195 K, $U_s$ = 2.15 V, $I_t$ = 0.10 nA). Black and red solid lines mark intact tetraketone 1 and tetraamine 1 molecules, respectively. Black and red dashes outline decomposed tetraketone 1 and tetraamine 1 molecules, respectively.

Further heating the sample to higher temperatures leads to decrease of the polymer-like domains and increase of the fence-like domains obviously. When heated up to 430 K, there were mainly fence-like domains, which can be confirmed by the overview image in **Figure 3.20**a. These fence-like arrangements maintained after annealing the sample to 460 K. The detailed arrangement has already been discussed above in **Figure 3.19**. After annealing the sample to 490 K, the coverage and structure did not change too much (**Figure 3.20**b). Deduced from the detailed image after this heat treatment in **Figure 3.20**c, so many *tert*-butyl groups were decomposed marked in black dashed lines for tetraketone and red dashed line for tetraamine. Nevertheless, the fence-like domains within the framework still maintained. Although some *tert*-butyl groups decomposed, the backbone of tetraketone is still vigorously anchored to the substrate confirmed by the faint contrast labeled in black dashed lines, which also stabilize the arrangement. Presumably because of the strong interaction with the substrate, the molecules were trapped into this framework and could not react with each other.

### 3.1.1.4 Comparison and discussions

From the above three subchapters, we can get some general understanding about the influence of different substrates on this Schiff-base condensation reaction. Only on the Ag(111) substrate, PPA-based oligomers occurred after thermal treatment. On the Au(111) substrate, no oligomers formed because the tetraketone 1 desorbed rather than reacted with

tetraamine 1 after stepwise heating up to 610 K (**Figure 3.12**). After annealing to 610 K, the surface contained almost exclusively tetraamine molecules with numerous *tert*-butyl groups decomposed. On the Cu(111) surface, no oligomers formed either after annealing up to 490 K, although a number of *tert*-butyl groups decomposed under this annealing treatment (**Figure 3.20**c).

Based on these results, we infer that Ag binds the monomers strongly enough for them to react on the surface, but not so strong as to inhibit the lift-off necessary for the imine formation. In contrast, on Au the tetraketone monomer desorbed during higher temperature annealing. On Cu, the monomers have a higher affinity to the metal surface and therefore decompose at annealing temperatures below the condensation temperature found on Ag(111). The lift-off of the ketone might be further hindered on Cu due to a stronger coupling.

Complementary XPS characterization of these reactants on Ag(111) and Au(111) sheds light on the reaction mechanism. The N 1s spectra of the tetraamine 1 on Ag(111) after RT deposition and annealing to 510 K have already been discussed above in **Figure 3.3**. From that we can deduce that the Ag surface activates the amines by partial dehydrogenation, which is expected to promote the desired imine formation. In such a case, the condensation reaction would proceed slightly differently on the Ag surface than in solution (Scheme 3.2), with $H_2$ as one of the by-products at lower temperature.[112]

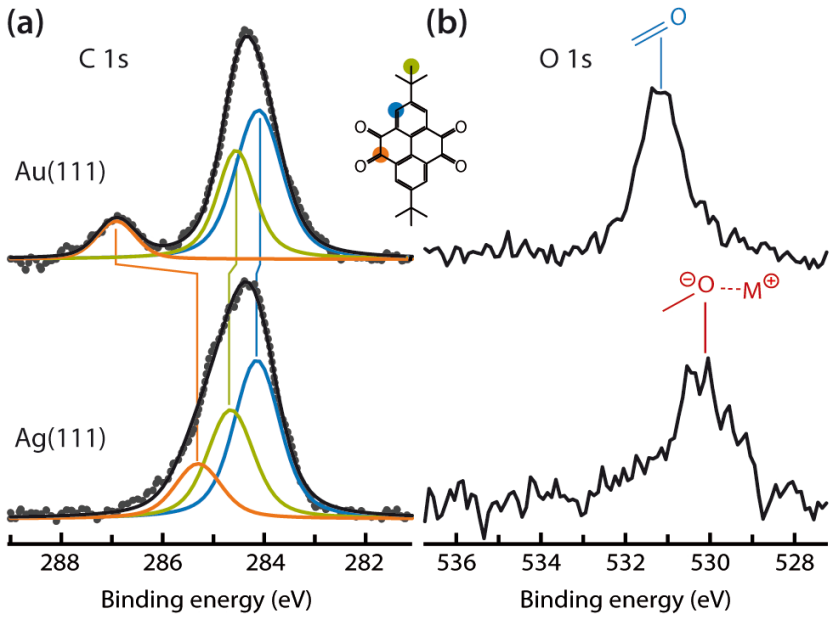


**Figure 3.21:** XP spectra of the C 1s (a) and O 1s (b) core levels, corresponding to a submonolayer coverage of tetraketone 1 on Au(111) (top) and Ag(111) (bottom) after RT deposition. In the C 1s signal three different

contributions can be resolved in the analysis. The corresponding peaks are colored as the highlights of the respective C atoms in the molecular model. All spectra were acquired using monochromatized Al Kα radiation.

XPS spectra of tetraketone 1 on Ag(111) are already displayed in **Figure 3.4**. Here, the data collected on Au(111) substrate is also included to make a comparison. On Au(111), the C 1s spectrum shows three contributions at binding energies of 284.1,[101,102] 284.6,[102,103] and 286.9 eV,[100,104] which can be attributed to the presence of aromatic, aliphatic, and carbonylic carbon atoms, respectively, with a ratio of approximately 3:2:1. The O 1s spectrum instead displays a single peak centered at a binding energy of 531.2 eV corresponding to carbonylic O (-C=O).[100,113] On Ag(111) this peak shifts to lower binding energy by ~ 1 eV, which is ascribed to hybridization of the C=O group with the substrate metal states ($-C-O^{-\cdots}M^{+}$).[100] From the comparison we infer that the hybridized oxygen is beneficial to this polymerization reaction, probably because the tetraketone molecules can remain in the vicinity of the Ag(111) surface upon annealing to higher temperatures, and thereafter, they can adopt the optimal geometric configuration relative to tetraamines to activate the imine formation reaction before desorbing from the surface. In contrast, there is no hybridized oxygen on Au(111), and as a consequence of the weaker anchoring the tetraketone molecules desorb from the surface before reacting with tetraamines.

### 3.1.2 Tetraamine 1 and tetraketone 3 on the Ag(111) substrate

As discussed in the previous section, the imine formation reaction requires an activation step: the lift-off of the ketones. In order to produce longer polymer not only oligomers, a new precursor: 2,7-bis((triisopropylsilyl)ethynyl)pyrene-4,5,9,10-tetraone (tetraketone 3) with two bulky side groups (TIPS groups) intending to lift-off the ketone module was investigated. As the reaction worked before only on the Ag, we investigated this tetraketone 3 and tetraamine 1 only on Ag(111).

Firstly, we studied the self-assembly of individual tetraketone 3 on Ag(111). After RT deposition, different packing appeared on the surface. One is a parallel packing with the ketones facing to each other as shown in **Figure 3.22**a. Similar to the appearance of tetraketone 1, the very bright lobes are corresponding to the physically protruding TIPS groups, whereas the molecular backbone is resolved more faintly. Besides this, in between two adjacent tetraketones, one additional small bright lobe appeared, outlined in blue circle, which is probably caused by ketones interacting with Ag adatoms, which is much clearer to see from the magnified image of the purple box in (a) superposed with molecular models.

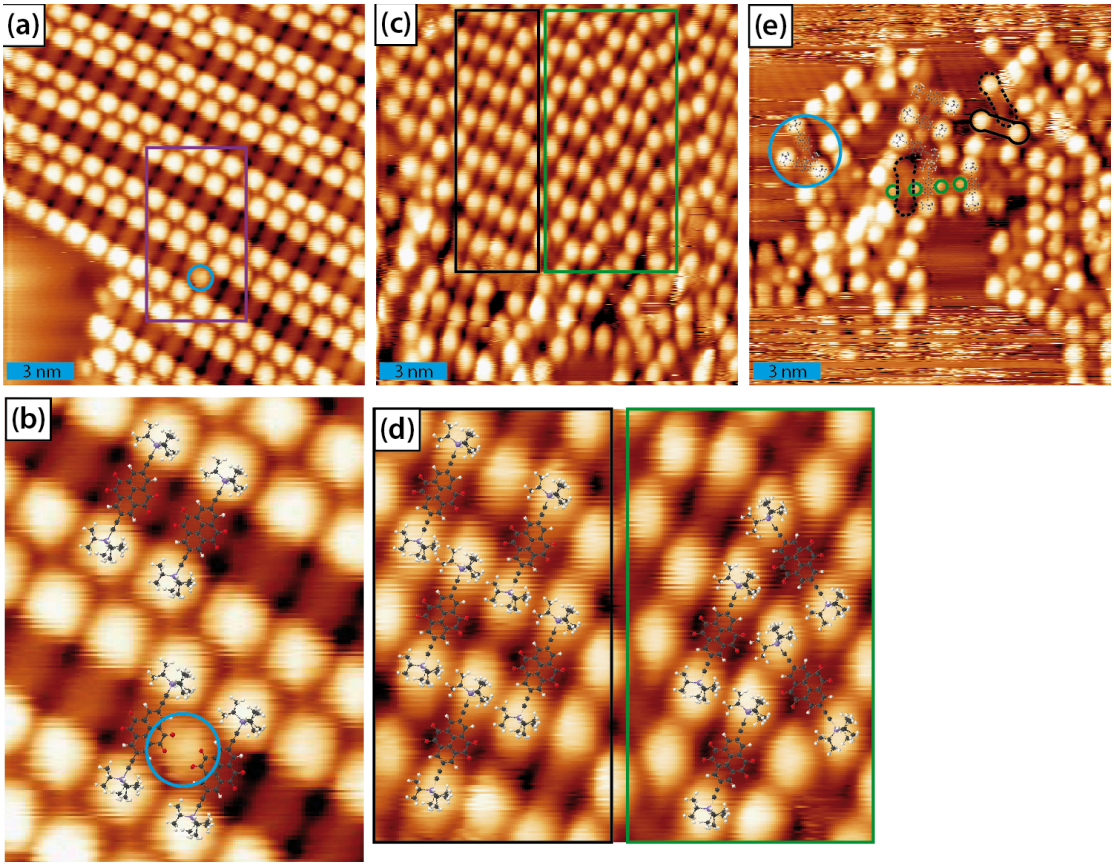


**Figure 3.22:** (a, c) Different packing of individual tetraketone 3 after RT deposition on Ag(111) ($T_{STM}$ = 113 K, $U_s$ = 1.32 V, $I_t$ = 0.11 nA). (b, d) Magnified images of (a, c) superposed with molecular models. (e) After annealing the sample to 390 K ($T_{STM}$ = 153 K, $U_s$ = 1.68 V, $I_t$ = 0.11 nA). A large portion of tetraketones decomposed (dashed line models) or interacted with each other (green/blue circles).

**Figure 3.22**c shows two other assemblies: one is parallel packing yet with ketones facing to TIPS groups (black box), and the other one is a staggered packing scheme (green box). The magnified image shown in (d) gives intuitive description of the two different packing. After annealing to 390 K, most of the tetraketones desorbed from the surface, and the remaining molecules partly decomposed as seen in **Figure 3.22**e. Black solid lines highlight intact molecule and the dashed lines indicate the decomposed molecules with TIPS groups imaged more faintly. Some molecules fused together, outlined in blue circle. More ketones seem to interact with Ag adatoms as the amount of bright small lobes increased (green circles).

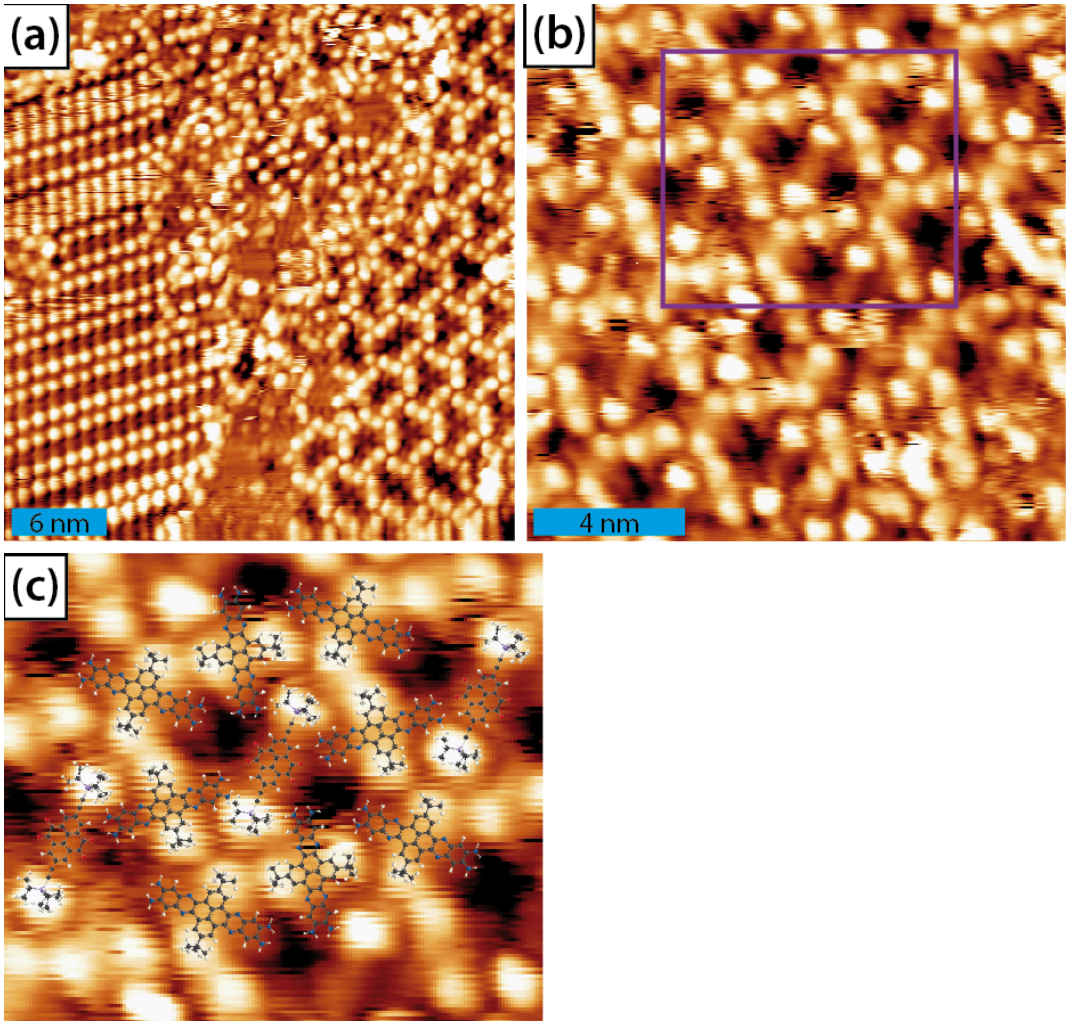


**Figure 3.23:** (a) STM image of tetraamine 1 and tetraketone 3 in a 1:1 ratio after subsequent deposition on Ag(111) kept at RT ($T_{STM}$ = 100 K, $U_s$ = 1.53 V, $I_t$ = 0.09 nA). (b) Detailed image of the mixture of the two molecules ($T_{STM}$ = 100 K, $U_s$ = 1.53 V, $I_t$ = 0.11 nA). (c) Magnified image of the purple box in (b) superposed with molecular models.

Further, we dosed tetraketone 3 and tetraamine 1 in a 1:1 ratio on Ag(111) at RT. The two molecules preferred not to intermix with each other. Instead they rather segregated in different domains shown in **Figure 3.23**a. The detailed structures have already been described in **Figure 3.2**b and **Figure 3.22**a. But there are also areas composed of the mixture of the two molecules forming a grid-like arrangement (in **Figure 3.23**b, c), where one tetraketone surrounded by eight tetraamines.

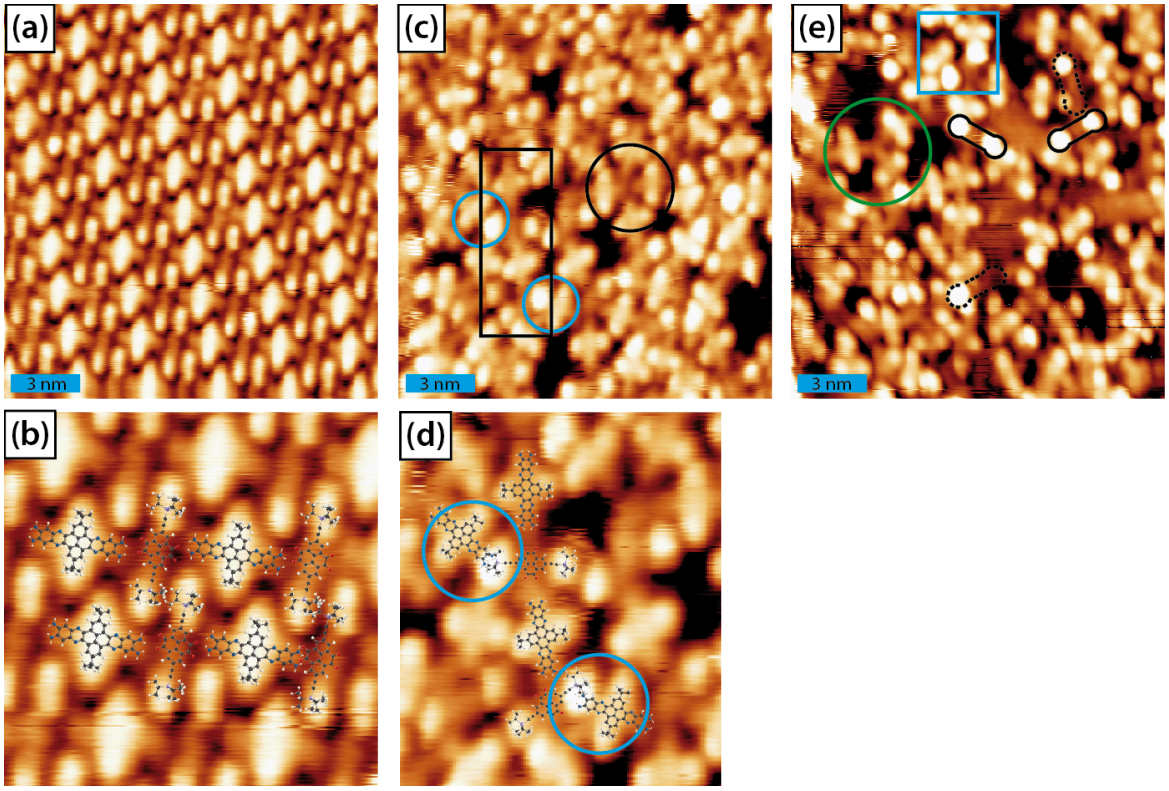


**Figure 3.24:** STM images of the self-assembly of tetraketone 3 with tetraamine 1 on Ag(111) surface as a function of annealing temperature. (a, c) Different domains of the molecules after annealing to 430 K ($T_{STM}$ = 160 K, $U_s$ = 1.79 V, $I_t$ = 0.11 nA). (b, d) Magnified images of (a, c) superposed with molecular models. In the domain displayed in (c), some tetraamine interacted with its TIPS groups highlighted in blue circles. (e) After annealing to 490 K ($T_{STM}$ = 200 K, $U_s$ = 1.79 V, $I_t$ = 0.11 nA). Black solid lines and dashed lines are for intact tetraketone 3 and decomposed tetraketone 3 molecules, respectively. The green circle indicates tetraamines that are fused together. The blue box highlights tetraamines reacted with TIPS groups.

After annealing to 430 K, the segregated domains disappeared and the two molecules mixed together, either in an ordered self-assembly (in **Figure 3.24**a) or in a disordered arrangement (in **Figure 3.24**c). In this long range ordered domain, tetraamine 1 stabilized with tetraketone 3 by intermolecular interactions between amines and ketones. Because the backbone of tetraketone 3 is longer than that of tetraamine 1, this alignment is different than the one observed before. The detailed imaging superposed with molecular models is shown in **Figure 3.24**b. Apart from the regular domains above, there were many areas shown in **Figure 3.24**c, where clustered tetraamines covered most of the surface, marked in black circle. Though the occurrence of oligomers was suspected (in the black box), it showed that they were not covalently linked together after superposing molecular models on the image (**Figure 3.24**d). Additionally, some tetraamines reacted with the TIPS groups, indicated by the blue circles.

After further annealing to 490 K, no ordered domain existed, and most of the tetraketone 3 molecules desorbed from the surface, and tetraamines fused together, marked in green circle. Some TIPS groups decomposed, shown in dashed line models and more tetraamines reacted with TIPS groups, indicated by the blue box.

Deduced from the above experiments, no desired Schiff-base formation reaction happened on Ag(111) with this new tetraketone 3 molecule. This is probably caused by the weaker interaction between the new molecules and the substrate and the lift-off effect of the big side groups. So most of the molecules desorbed from the surface before reacting with tetraamines. Besides this, the TIPS groups are chemically more active than ketones groups and the tetraamines tend to react with the TIPS groups instead of the ketones.

### 3.1.3 Tetraamine 1 and tetraketone 2 on the Ag(111) substrate

Based on the previous experience, we further tailored the molecule by removing the triple bond linking the TIPS groups in order to decrease its reactivity. In the following, we studied the molecular behavior of 2,7-bis(triisopropylsilyl)pyrene-4,5,9,10-tetraone (tetraketone 2) and tetraamine 1 on Ag(111).

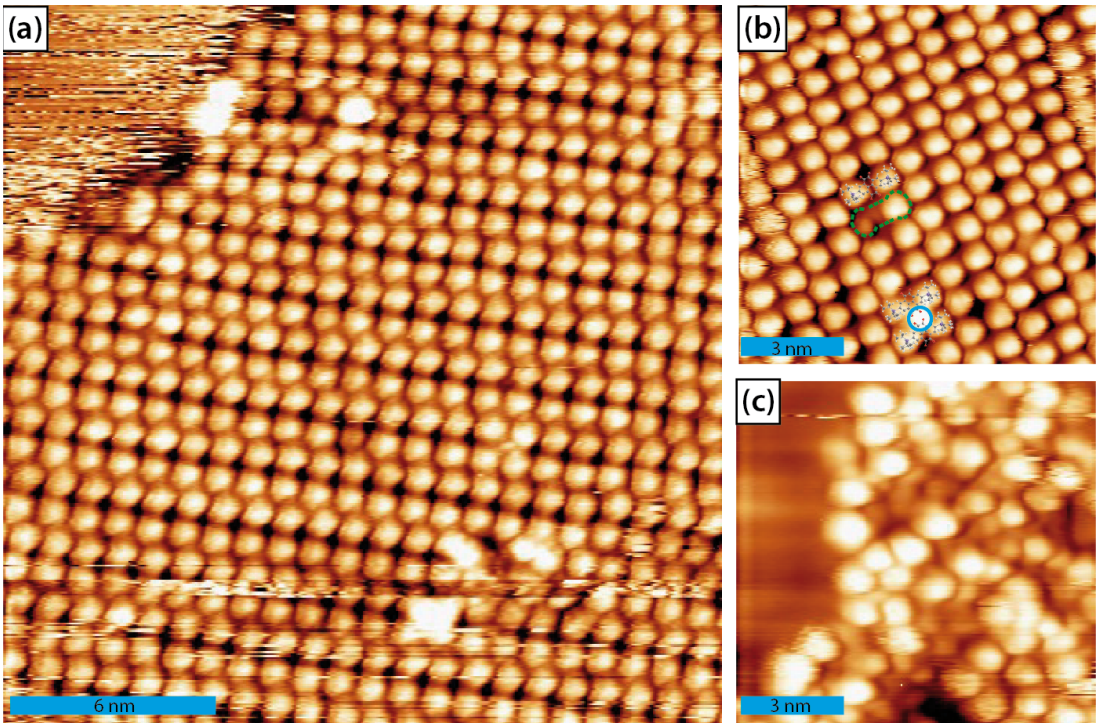


**Figure 3.25:** (a) STM image of the self-assembly of tetraketone 2 on Ag(111) after RT deposition ($T_{STM}$ = 120 K, $U_s$ = 1.25 V, $I_t$ = 0.10 nA). (b) After annealing to 390 K ($T_{STM}$ = 210 K, $U_s$ = 1.16 V, $I_t$ = 0.09 nA). Green dashed line marks one tetraketone molecule with decomposed TIPS group, and the blue circle indicates

ketones which might have reacted with Ag adatoms. (c) After annealing to 560 K ($T_{STM}$ = 130 K, $U_s$ = 1.13 V, $I_t$ = 0.10 nA).

After RT deposition on Ag(111), tetraketone 2 formed a similar self-assembly as the other two molecules (in **Figure 3.25**a). After annealing to 390 K, the arrangement is even more regular, but some TIPS groups have already been damaged, marked by the green dashed line in **Figure 3.25**b. Besides, some tetraketones interacted with Ag adatoms shown in the blue circle. Further heating to 560 K totally destroyed this arrangement. The molecules clustered together and many TIPS groups were damaged.

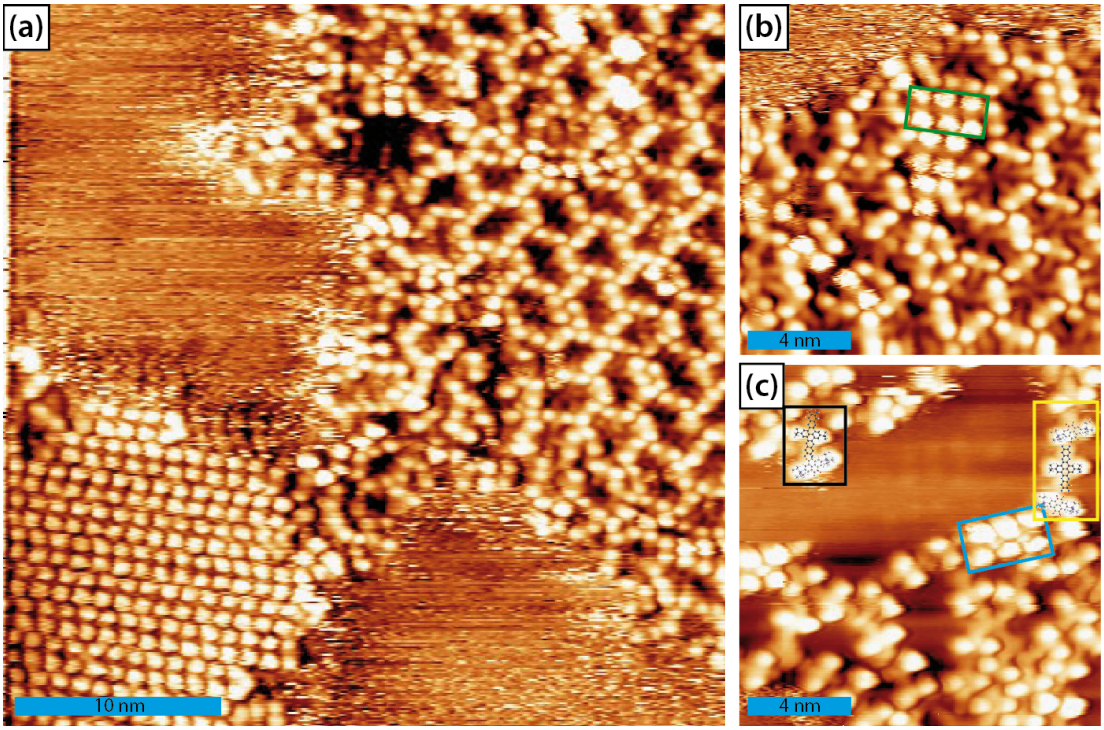


**Figure 3.26:** (a) STM image of the mixture of tetraketone 2 and tetraamine 1 on Ag(111) after RT deposition ($T_{STM}$ = 120 K, $U_s$ = 1.25 V, $I_t$ = 0.06 nA). (b) Detailed image of tetraamine 1 intermixed with tetraketone 2 ($T_{STM}$ = 130 K, $U_s$ = 1.25 V, $I_t$ = 0.09 nA). (c) After annealing to 550 K ($T_{STM}$ = 170 K, $U_s$ = 1.25 V, $I_t$ = 0.08 nA). Blue box indicates tetraketones that might have reacted with Ag adatoms.

Then we dosed the two molecules on Ag(111). The two molecules segregated similar to what was observed before in two different domains instead of mixing together as shown in **Figure 3.26**a. Only a small fraction of tetraketone 2 intermixed with tetraamine 1 and even in this small region, tetraketone 2 still prefers to stick together, indicated by the green box in **Figure 3.26**b.

After annealing to 550 K, a large portion of tetraketones desorbed from the surface. Some tetraketone interacted with tetraamine forming linear structures yet with H-bond interaction

and almost no covalent bonding could be observed (in yellow box). But there are indeed some oligomers, for example, marked in black box, which is the aforementioned kinked dimer with one ketone reacting with one amine forming one imine. There are also many tetraketones interacting with Ag adatoms, indicated by the blue box, as well as tetraamines fused together after this high temperature treatment. Nevertheless still no desired long polymers were generated with these two precursors.

### 3.1.4 Tetraamine 3 and tetraketone 2 on the Ag(111) substrate

Then we tried another route by using a modified amine without the *tert*-butyl groups and shortened molecular backbone. Here the combination of tetraketone 2 and the new designed molecule: phenazine-2,3,7,8-tetraamine (tetraamine 3) is studied on Ag(111).

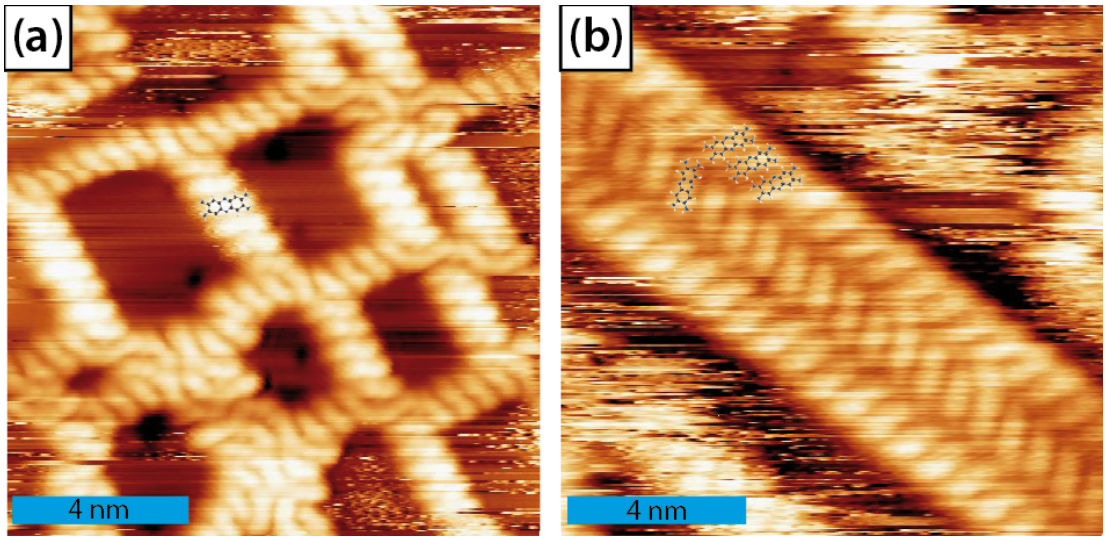


**Figure 3.27:** Different types of self-assemblies of tetraamine 3 on Ag(111) after RT deposition. (a) Grid-like domain ($T_{STM}$ = 130 K, $U_s$ = 1.28 V, $I_t$ = 0.10 nA). (b) Stripe-like domain ($T_{STM}$ = 120 K, $U_s$ = 1.58 V, $I_t$ = 0.13 nA).

Firstly, the self-assembly of the new tetraamine 3 was studied and is displayed in **Figure 3.27**. After RT deposition, the molecules formed different structures on the surface, either a grid-like domain or a stripe-like domain. Because the molecules are very small, they are mobile even at low scanning temperatures (120 K). After annealing to 390 K, a large portion of the tetraamine molecules desorbed from the surface. After further annealing to 500 K, nearly all the molecules were gone.

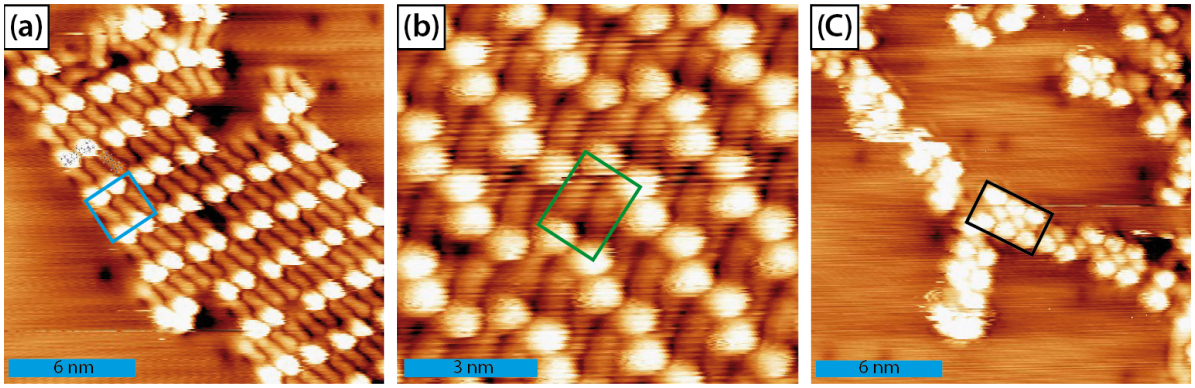


**Figure 3.28:** (a) STM image of the mixture of tetraketone 2 and tetraamine 3 on Ag(111) after RT deposition ($T_{STM}$ = 110 K, $U_s$ = 1.25 V, $I_t$ = 0.10 nA). (b) After annealing to 390 K ($T_{STM}$ = 170 K, $U_s$ = 1.25 V, $I_t$ = 0.10 nA). (c) After annealing to 560 K ($T_{STM}$ = 110 K, $U_s$ = 1.28 V, $I_t$ = 0.11 nA).

Then we dosed tetraamine 3 and tetraketone 2 subsequently on Ag(111). The two molecules intermixed with each other very well after RT deposition shown in **Figure 3.28**a. In most cases, one tetraketone 2 interacted with three tetraamine 3 (in blue box) with its amines groups faced toward the ketones. After annealing to 390 K, a substantial part of the tetraamine 3 molecules desorbed, as expected based on the study of individual tetraamine 3. Now one tetraketone 2 interacts with two tetraamine 3 indicated by the green box in **Figure 3.28**b. After further annealing to 560 K, almost all the tetraamine 3 molecules desorbed from the surface and the remaining tetraketone 2 interacted with Ag adatoms shown in the black box in **Figure 3.28**c.

So this attempt to form the desired reaction with tetraamine 3 also failed because this molecule is too small to withstand the high temperature treatment and desorbed from the surface before reacting with tetraketone 2.

### 3.1.5 Tetraamine 2 and tetraketone 2 on the Ag(111) substrate

To address the weakened anchoring strength resulting from shortening of the backbone in tetraamine 3, we employed a new precursor: 1,12b-dihydroquinoxalino[2',3':9,10]phenanthro[4,5-*abc*]phenazine-6,7,15,16-tetraamine (tetraamine 2) with the same backbone as that of tetraamine 1 but without the *tert*-butyl groups and investigated the molecular behavior of this tetraamine 2 with tetraketone 2 on Ag(111).

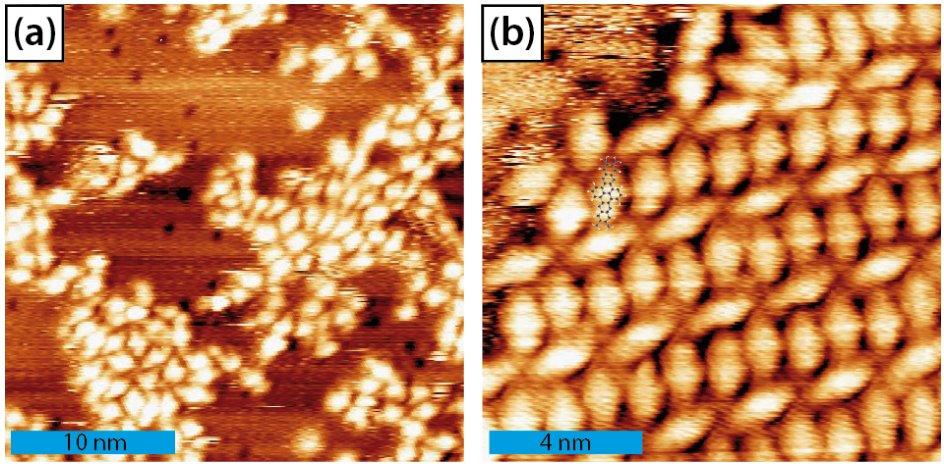


**Figure 3.29:** Different domains of tetraamine 2 on Ag(111) after RT deposition. (a) Disordered arrangement ($T_{STM}$ = 150 K, $U_s$ = 1.13 V, $I_t$ = 0.12 nA). (b) Ordered self-assembly ($T_{STM}$ = 150 K, $U_s$ = 1.32 V, $I_t$ = 0.11 nA).

After RT deposition on Ag(111), tetraamine 2 molecules tended to interact with each other head to head forming either disordered domains as in **Figure 3.29**a, or two dimensional ordered structures as shown in **Figure 3.29**b. Due to the lack of the *tert*-butyl groups, amines can interact with iminic N in the backbone generating this fence-like arrangement.

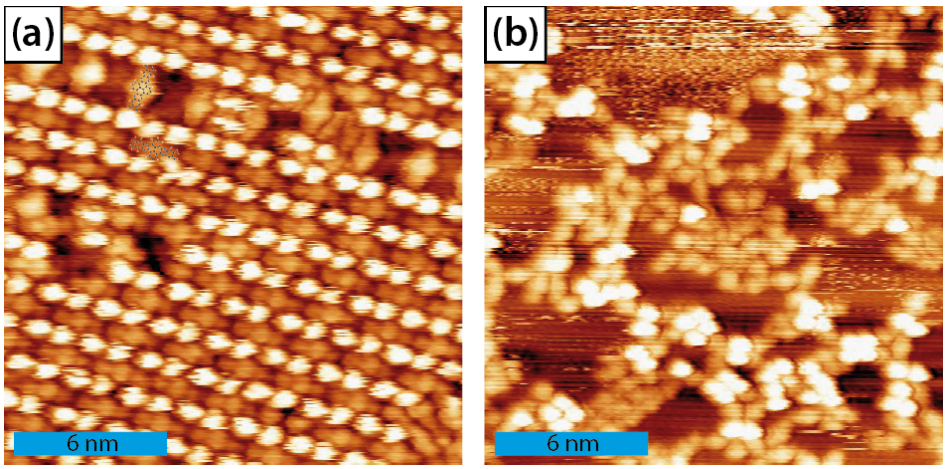


**Figure 3.30:** (a) STM image of the mixture of tetraketone 2 and tetraamine 2 on Ag(111) after RT deposition ($T_{STM}$ = 130 K, $U_s$ = 1.25 V, $I_t$ = 0.12 nA). (b) After annealing to 500 K ($T_{STM}$ = 170 K, $U_s$ = 1.44 V, $I_t$ = 0.14 nA).

Subsequently, we dosed tetraketone 2 on this Ag(111) substrate containing tetraamine 2. The two molecules intermixed with each other as shown in **Figure 3.30**a. Most of the tetraamine 2 are parallel to the tetraketone 2 and only a small fraction of tetraamine 2 is perpendicular to tetraketone 2. After annealing up to 500 K, desorption of tetraketones was observed, and the left tetraamines did not exhibit any ordered arrangement.

This newly tailored molecul still did not have the desired effect but this time tetraamine 2 could survive high temperature annealing and stay on the surface. The problem is that the ketones prefer facing to the iminic N in the ring without the hindrance of the *tert*-butyl groups, which is not beneficial to the imine formation reaction. Although at higher annealing temperatures, there is too much mobility to overcome this attractive interaction.

### 3.1.6 Summary and Conclusions

In this chapter, we did a comprehensive investigation of Schiff-base formation reaction on three coinage metal surfaces by utilizing STM and XPS measurements and employing different reactants in ultra-high vacuum conditions.

In the first combination of tetraketone 1 and tetraamine 1, we explored the influence of the annealing temperature, stoichiometry of tetraketone to tetraamine, and the underlying metal surface. On Ag(111), tetraketone 1 and tetraamine 1 can form zigzag conformation stabilized by intermolecular H-bond interactions between amine and ketone groups as well as between ketone and hydrogen of the phenyl groups, which maintained after RT deposition and gradually annealing to 510 K. Besides, we found that this imine formation reaction requires an activation step: a lift-off of the ketones. Different oligomers could be generated only on the Ag(111) substrate because silver gives the best compromise between adsorption strength and moderate chemical interaction.

Deduced from XPS characterization, the majority of the ketone groups hybridized with the silver surface after RT deposition of the tetraketone. This hybridization presumably enables the molecule to remain on the surface during the temperature activated lift-off of the ketones, which creates a suitable geometry to react with a diamine terminated module. The proposed mechanism is illustrated in **Figure 3.31** by a schematic drawing.

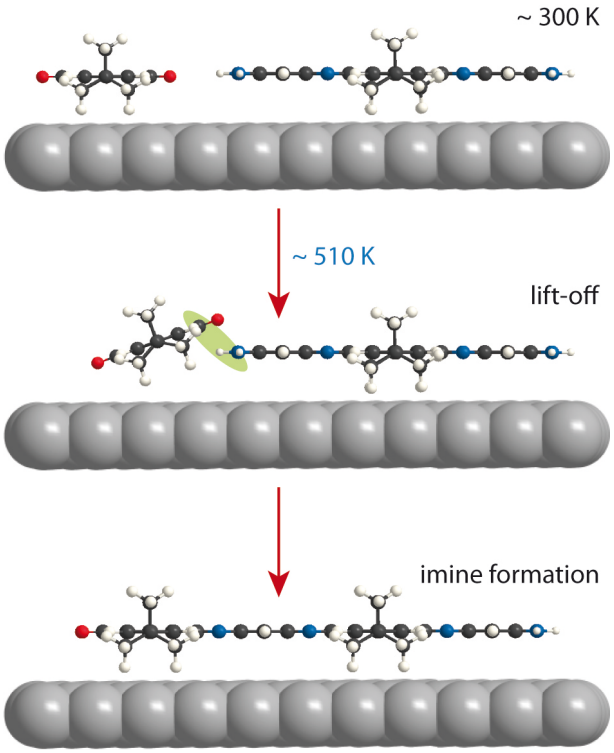


**Figure 3.31:** Cartoon of the imine formation mechanism by reaction of tetraketone 1 (left) and tetraamine 1 (right) on the Ag(111) surface. From top to bottom: After RT deposition, ketone moieties are strongly hybridized with the metal surface. At ~ 510 K, the ketone lift-off enables a suitable geometry (green highlight) for the formation of new imines.

We found that in general the cyclocondensation is favored over the single imine formation. Moreover we observed that dimers are the preferred products, but in the presence of an excess of tetraketone molecules, ketone terminated trimers become the most favorable. The elongation to longer oligomers seems instead to be unfavorable.

Importantly, we found marked differences between supporting the employed reactants on gold, silver and copper. Among the three coinage metals, silver gives the best compromise between adsorption strength and relatively weak chemical interaction: both molecules can be confined in the vicinity of the surface under conditions that facilitate the condensation reaction. On the Au(111) surface, tetraketone and tetraamine went through several temperature dependent phase transformations. But the anchoring appears to be too weak to promote the condensation reaction, such that the majority of the tetraketone molecules desorbed when the temperature was raised. On the contrary, the Cu(111) surface interacts too strong with the molecules and resulted in decomposition rather than polymerization. This is because dehydrogenated amines coordinated with copper adatoms forming a quite strong framework that won't break down to facilitate the condensation reaction.

In order to produce longer polymers and not only oligomers, we tailored the molecular precursors and tried different combinations. Since this imine formation reaction requires an activation step, we employed a new precursor: tetraketone 3 with two big side groups (TIPS groups) that can lift off the ketones from the surface and mixed it with tetraamine 1. But no expected polymers generated on Ag(111) probably because the interaction between the new molecule and the substrate is too weak due to the lift-off effect of the big side groups, so most of the molecules desorbed from the surface before reacting with tetraamines. Besides this, the TIPS groups are more active than the ketones and therefore tetraamines tend to react with TIPS groups instead of ketones.

We further tailored the molecule by removing the triple bond linking to the TIPS groups (tetraketone 2) in order to decrease its reactivity, and again mixed it with tetraamine 1. But no expected long polymers generated with these two precursors, probably because the two molecules dislike mixing together and then there is no chance of triggering this reaction.

Then we tried another way by removing the *tert*-butyl groups and shortening the molecular backbone to decrease the steric hindrance. It turns out that the combination of tetraketone 2 and this new designed molecule (tetraamine 3) also failed to produce longer polymers although they intermixed very well with each other, because this tetraamine 3 molecule is too small to withstand high temperature treatment and desorbed from the surface before reacting with tetraketone 2.

Therefore, we used another precursor: tetraamine 2 without the *tert*-butyl groups yet with a long backbone. But this tailoring of the molecule still did not work although this time tetraamine 2 can survive high temperature annealing and stays on the surface. The problem is that ketones prefer facing to iminic N in the ring without the steric hindrance of the *tert*-butyl groups, which is not beneficial to the imine formation reaction.

In conclusion, this work has demonstrated the feasibility of preparing PPA-based oligomers on a metal surface, but there is still a long way to go to produce long polymers. The combination of direct visualization of all reactants and reaction products combined with the spectroscopic characterization of the reactants has provided a unique mechanistic insight into the interfacial synthesis of PPA-based oligomers on solid surfaces. This is expected to provide valuable input to the rational design of appropriate building blocks and platforms by imine formation as well as a sound methodology for studying other on-surface polymerization reactions.

## 3.2 Surface confined Ullmann coupling: halogen bonded self-assembly versus metal coordinated nanoarchitectures

Since the first report of the experimental synthesis of graphene via the "Scotch tape" method in 2004,[114] extensive studies about graphene revealed potential for applications in fields such as electronics, sensors, batteries, and catalysts.[28-31] However, the appliances of graphene in electronics are limited owing to its lack of a band-gap, which indicates its conductivity cannot be switched off.[115] Doping it with other elements is a promising way to tailor the electrical properties of graphene.[42,116-120] Especially, N-doping could introduce additional n-type carriers into carbon systems, which is helpful in semiconductor devices[42], energy conversion and storage facilities[43,44], as well as bio-sensing applications[45-47]. There are already many references introducing different ways of synthesizing this N-doped graphene.[36,116,120-123]

The Ullmann coupling is the oldest known C-C coupling method for aromatic molecules.[124] It has been demonstrated as a feasible route for C-C coupling of halogenated molecules on several metal surfaces: copper[23,125-127], silver[22,128] and gold[10,19,24]. C-H bonds cleavage and activation was achieved to form intermolecular aryl-aryl coupling, which has been utilized for the preparation of graphene nanoribbons on metal surfaces,[129-131] and under ultrahigh vacuum conditions[101,132,133]. Based on this, we proposed a new method, a two-step reaction to synthesize this N-doped graphene nanoribbons, first utilizing Ullmann coupling to link C-C, and then C-H cleaving and reacting with the neighboring N, shown in **Figure 3.32**. The first step is relatively well-established, but the second step is rather unexplored, especially on metal surfaces in UHV conditions. After the first report of experimental and theoretical evidence of covalent bonded C-N between benzene and pyridine in 2009[134], there was no significant progress in this area.

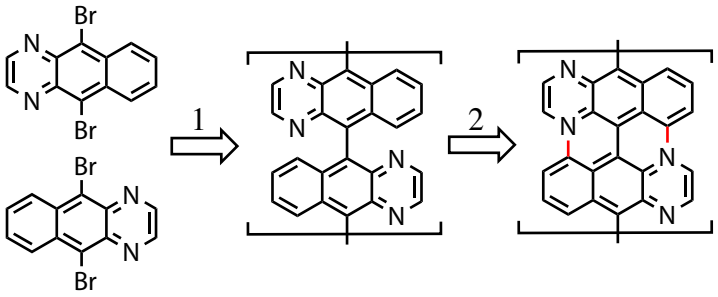


**Figure 3.32:** Two-step reaction procedures. (1) The first step: Ullmann coupling to link C-C. (2) The second step: C-H cleaving and reacting with the neighboring N.

In this section, we present results on two molecules: 5,10-dibromobenzo[*g*]quinoxaline (DBBQ) and 10,15-dibromobenzo[*i*]phenanthro[4,5-*abc*]phenazine (DBBPP), shown in **Figure 3.33**.

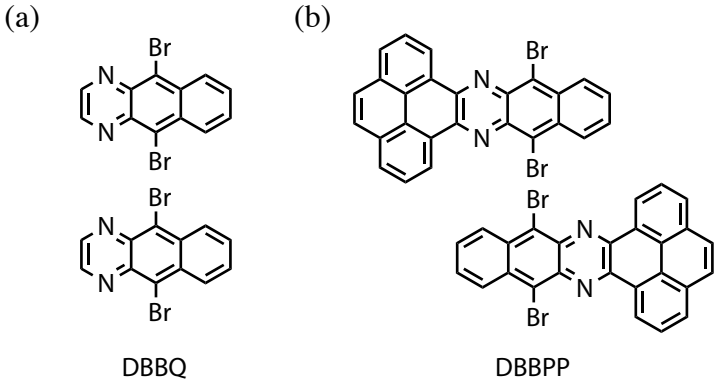


**Figure 3.33:** (a) Unfavorable geometry of DBBQ for the second reaction step. (b) New customized molecule DBBPP, intended to use the big side groups to force the molecules into a suitable relative position.

The Ullmann coupling of DBBQ can proceed in tow different geometries (**Figure 3.32** and **Figure 3.33**a) where the second (N of adjacent molecules face each other) is unfavorable for the second reaction step, resulting into the termination of the expected polymers. Therefore, another molecule DBBPP with a larger side group that can cause great steric hindrance, favoring a suitable relative position to trigger the reaction, was also investigated. We mainly employed STM to visually monitor the feasibility to produce this N-doped graphene nanoribbons, and utilized XPS measurements to explore the chemical changes during this process.

### 3.2.1 Molecular behavior of DBBQ on three coinage metal substrates

Firstly, we studied the self-assembly and thermal behavior of this small molecule DBBQ on Ag(111), Au(111) and Cu(111).

#### 3.2.1.1 Investigation of DBBQ on Ag(111)

First we discuss the results of X-ray photoelectron spectroscopy of DBBQ on Ag(111). In **Figure 3.34**a, the Br 3p XP spectrum (top) of DBBQ molecules deposited on a cold Ag(111) substrate ($T_s$ = 95 K) shows that the Br $3p_{3/2}$ binding energy is 184.4 eV, indicative of intact C–Br bonds.[135] After annealing to 300 K, this peak shifted to lower BE by about 2 eV, which is assigned to chemisorbed Br atoms formed after C–Br bond scission.[136]

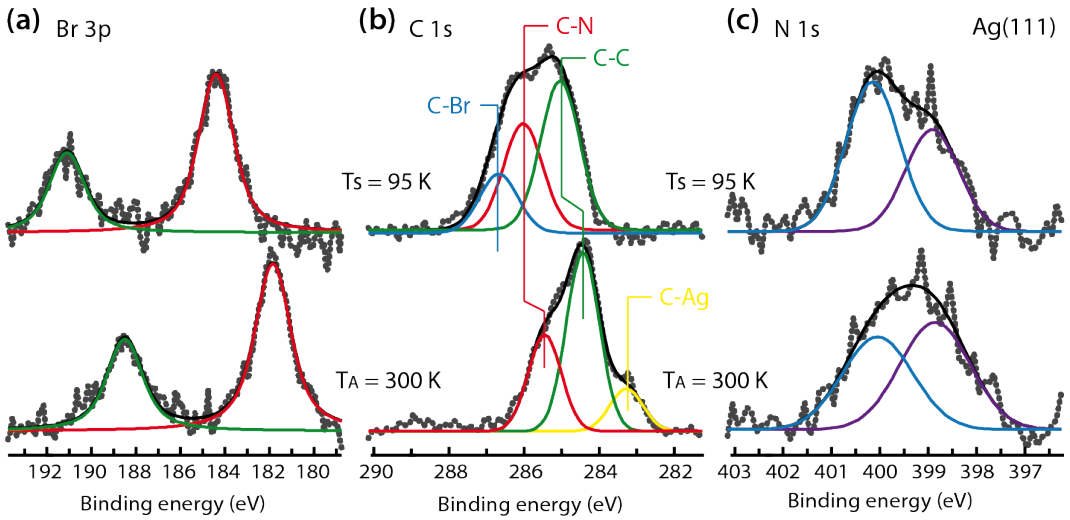


**Figure 3.34:** XP spectra of the Br 3p (a), C 1s (b), and N 1s (c) core levels of a submonolayer coverage of DBBQ on Ag(111) after deposition at 95 K (top), and after annealing to 300 K (bottom).

The C 1s spectra show clear changes during this process (**Figure 3.34**b). Three peaks appear with intensity ratio of 3:2:1, corresponding to the ratio of the chemically different C atoms on the molecule: unsubstituted $sp^2$ C, C next to N and C next to Br. The peak centered at 286.5 eV is assigned to C-Br[137,138], and is no longer present after annealing to 300 K, which further proved that the C-Br scission happened after this treatment. A new peak at 283.2 eV occurred, which is assigned to C-Ag metal coordination.[136-140] The peaks located at BE of 284.4 eV and 285.4 eV are assigned to $sp^2$ conjugated C and C-N, respectively.[141]

There is an interesting phenomenon in the N 1s spectra (**Figure 3.34**c). The DBBQ molecule contains two equivalent N but unexpectedly the N 1s spectrum is split into two peaks. The lower BE peak centered at 398.3 eV is assigned to iminic N (=N-).[142,143] Typically, the BE of metallated N is about 399-400 eV, however Ag coordination is not commonly observed with N atoms on surfaces.[144] Another rationalization could be the possible halogen bond between a Br atom and the N lone pair.[145,146] In our measurements, the higher BE peak is located at 400 eV. We can attribute this peak to the previously unobserved halogen bond between Br atoms and N in adjacent molecules, which is mediated by the surface providing a planar geometry[147]. After annealing to 300 K, C-Br scission happened. The chemisorbed Br atoms can still interact with N forming Br···N bonds.

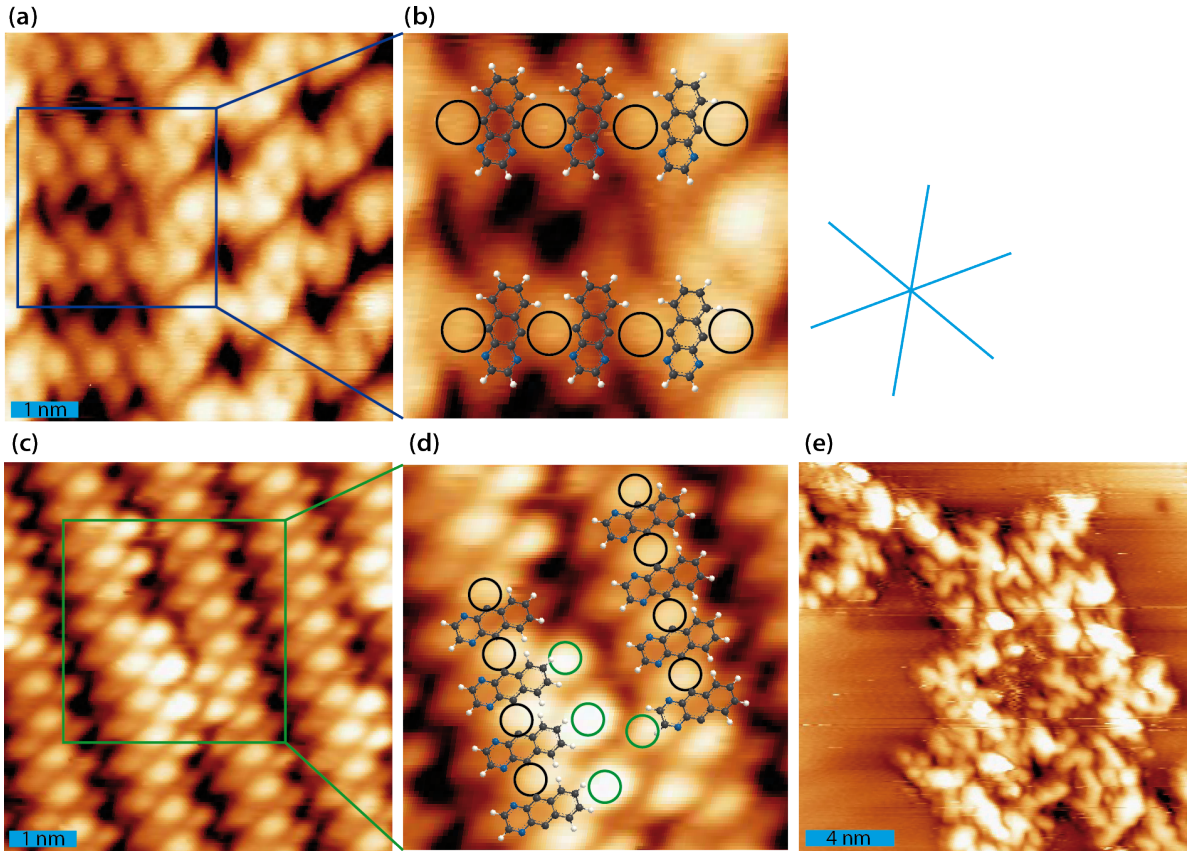


**Figure 3.35:** STM topography of DBBQ on Ag(111) after RT deposition (a) ($T_{STM}$ ~ 110 K, $U_s$ = 1.40 V, $I_t$ = 0.11 nA) and after annealing to 373 K (c) ($T_{STM}$ ~ 180 K, $U_s$ = 1.25 V, $I_t$ = 0.08 nA). (b, d) Magnified image of the blue and green box, respectively, superposed with possible molecular models. Black circles denote Ag adatoms, whereas green circles denote possible Br atoms. (e) STM image of aggregated molecules on Ag(111) after annealing to 500 K ($T_{STM}$ ~ RT, $U_s$ = 1.25 V, $I_t$ = 0.08 nA). The blue star indicates the high symmetry directions of the Ag(111) substrate.

As deduced from XPS measurements, DBBQ molecules completely debrominated after RT deposition on Ag(111). The STM result after RT deposition is shown in **Figure 3.35**a, where the faint stick-like objects correspond to the debrominated molecular backbone, and the brighter round protrusions represent Ag adatoms. The detailed image superposed with molecular models in **Figure 3.35**b gives a more intuitive demonstration. So it is quite clear by RT deposition on the Ag substrate, DBBQ molecules debrominated and interact with Ag adatoms, forming a favorable intermediate state of the Ullmann coupling.[137]

After gradually annealing to 373 K (**Figure 3.35**c), long-range order could be improved with elongation of the organometallic molecular chains made of bright dots interspaced by dark bars. Similar to the RT data, these bright dots linking the molecules are Ag adatoms, and in between the adjacent molecular chains, the other bright dots are probably Br atoms.[148] It is clearer to see from the magnified image superposed with molecular models.

We note that no direct evidence of the aforementioned Br···N halogen bonds can be found in our STM images of the self-assembly. However, as there is only a small portion of the expected Br atoms visible in the STM images, we can reasonably expect some of those to be in such a close proximity to the molecules, that they are not distinguishable. In the two preparations, the backbone of the DBBQ molecules all resembled along the high symmetry directions of the substrate. After further annealing to higher temperatures the surface coverage decreased and the remaining molecules aggregated in irregular islands, such as displayed in **Figure 3.35**e.

### 3.2.1.2 Thermal behavior of DBBQ on Au(111)

Since the desired Ullmann coupling did not succeed, we continued to study this molecule on the Au(111) substrate. The debromination was again monitored by the Br 3p spectra (**Figure 3.36**a). Molecules are also intact after deposition on a cold Au substrate ($T_s$ = 95 K). After annealing to 323 K, complete debromination was observed.

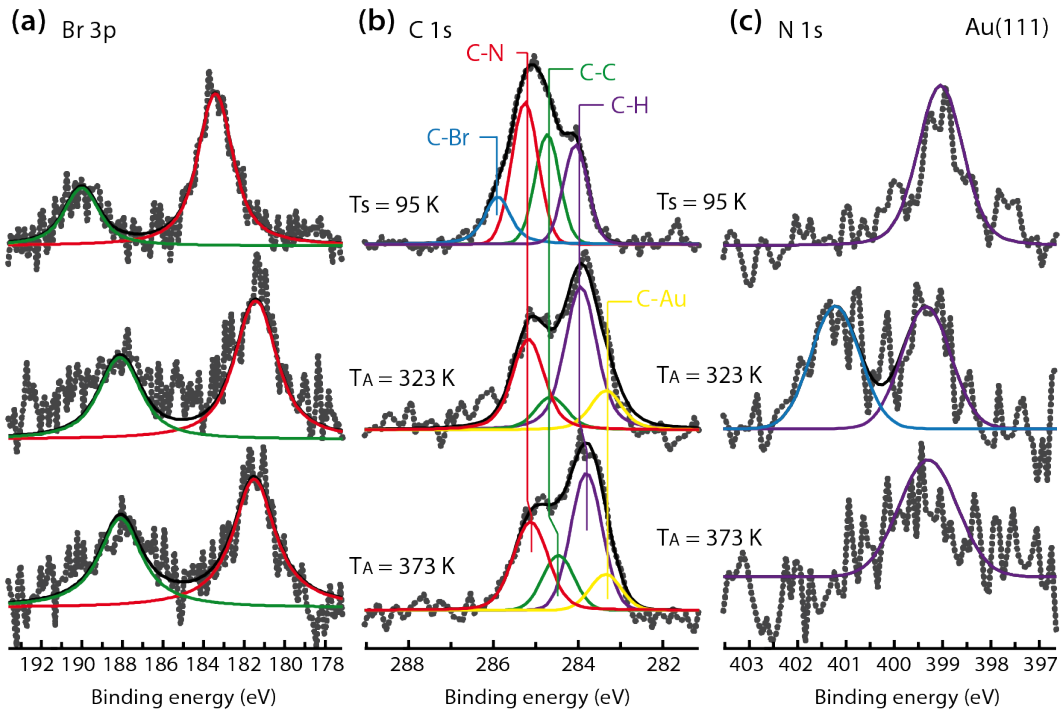


**Figure 3.36:** XP spectra of the Br 3p (a), C 1s (b), and N 1s (c) core levels of a submonolayer coverage of DBBQ on Au(111) after deposition at 95 K (top), after annealing to 323 K (middle), and after annealing to 373 K (bottom) .

The C 1s spectrum corresponding to the deposition of DBBQ on a cold Au substrate ($T_s$ = 95 K) is deconvoluted into the four peaks shown in **Figure 3.36**b (top). As discussed in the

former chapter, the peak centered at 285.9 eV is assigned to C-Br[149], which is no longer present after annealing to 323 K, confirming the completion of the debromination. The peak located at a BE of 285.2 eV is assigned to C-N[141], which remains the same after annealing to higher temperatures. Moreover, the peaks centered at 284.0 eV and 284.7 eV are assigned to $sp^2$ hybridized C-H and C-C, respectively,[140,150,151] which shifted to lower BE after annealing to 373 K. Similar to the results on Ag(111), there also appeared a new peak at lower BE of 283.3 eV, which originated from carbon bonded to gold[140] after annealing to 323 K.

However, the N 1s spectra are somewhat complicated (see **Figure 3.36**c). There is only one peak centered at 399 eV after deposition on the cold Au substrate, which can be assigned to the typical peak for pyridinic N[152]. After annealing to 323 K, there appeared a new peak at 401.3 eV, which is probably caused by a quaternary-type nitrogen.[152-155] The formation of this quaternary-type nitrogen could originate either from the interaction with Br atoms or with Au adatoms.[156,157] After further annealing to 373 K, this contribution vanished.

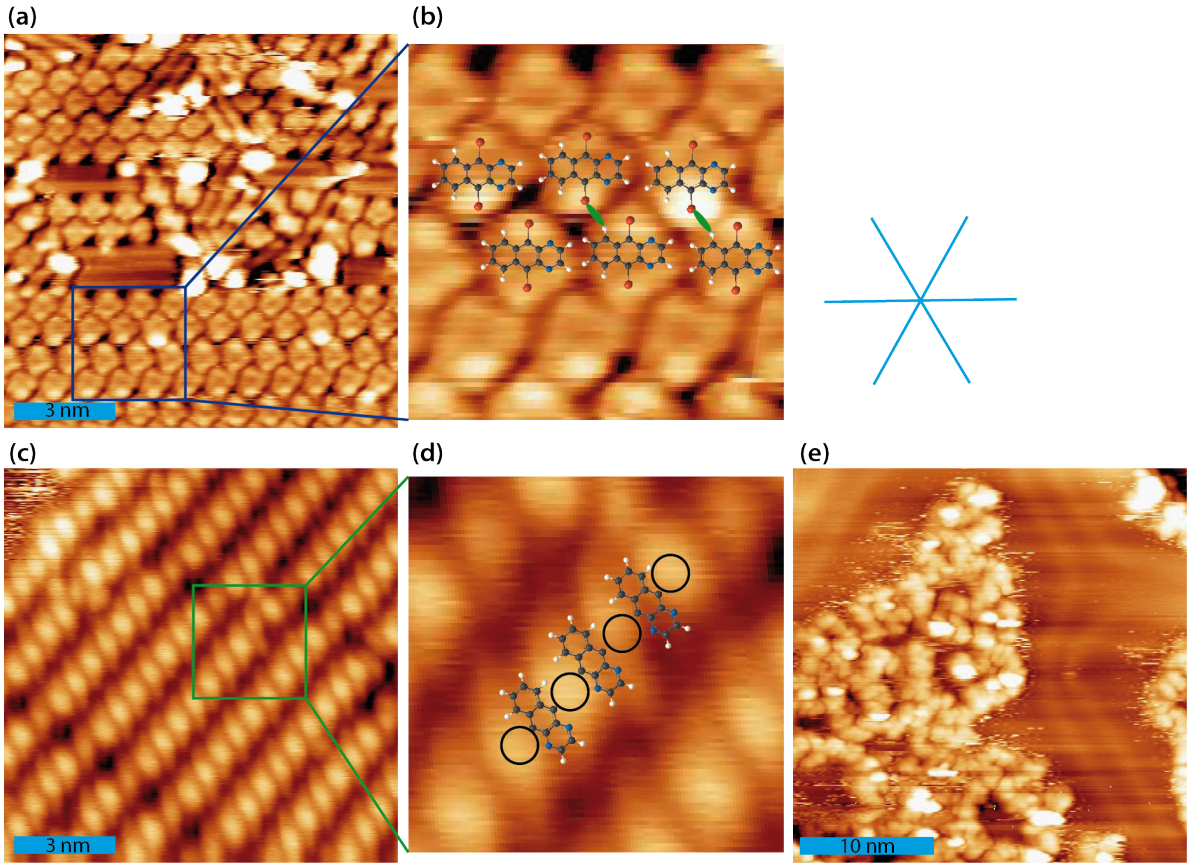


**Figure 3.37:** (a) STM morphology of DBBQ molecules on Au(111) after RT deposition and annealing to 323 K ($T_{STM}$ ~ 110 K, $U_s$ = 0.63 V, $I_t$ = 0.12 nA). (b) Magnified image of the blue box superposed with molecular

models. The green ovals indicate H-bond interactions. (c) STM image of metal coordinated molecular chains after annealing to 380 K ($T_{STM}$ ~ 200 K, $U_s$ = 0.94 V, $I_t$ = 0.10 nA). (d) Magnified image of the green box superposed with molecular models. The black circles represent Au adatoms. (e) STM image of aggregated molecules after annealing to 450 K ($T_{STM}$ ~ 180 K, $U_s$ = 1.20 V, $I_t$ = 0.11 nA). The blue star indicates the high symmetry directions of the Au(111) substrate.

A representative STM image after annealing to 323 K is displayed in **Figure 3.37**a. Intact DBBQ molecules were observed on the surface[158]. The molecular backbones aligned along the high symmetry directions of the substrate. The green ovals highlight the H-bond interactions between Br and H in benzene rings that stabilize this arrangement. But in other areas, some molecules debrominated and the Br atoms can be visualized. After annealing to 380 K, metal coordinated molecular chains appeared similar to those on Ag(111), in agreement with the XPS results. The dimmer bars are corresponding to molecular backbones, and the brighter protrusions are associated with Au adatoms. The molecular backbones also assembled along the high symmetry directions of the substrate. After further annealing to 450 K, most of the molecules desorbed from the surface and the remaining molecules aggregated in islands (see **Figure 3.37**e).

### 3.2.1.3 Investigation of DBBQ on Cu(111)

In the following, we investigated this molecule on the more active Cu(111) substrate. As usual, we first explored the chemical state of this molecule after deposition.

Molecules are also intact after deposition on the cold Cu(111) substrate ($T_s$ = 100 K), deduced from Br 3p spectrum shown in **Figure 3.38**a. After annealing to 173 K, partial debromination already happened. Following further annealing to 373 K, molecules are fully debrominated. The evolution of C 1s spectra is very similar to that on Ag(111) (**Figure 3.34**b), where the appearance of lower BE peak at 283.7 eV is assigned to the carbon bound to copper.

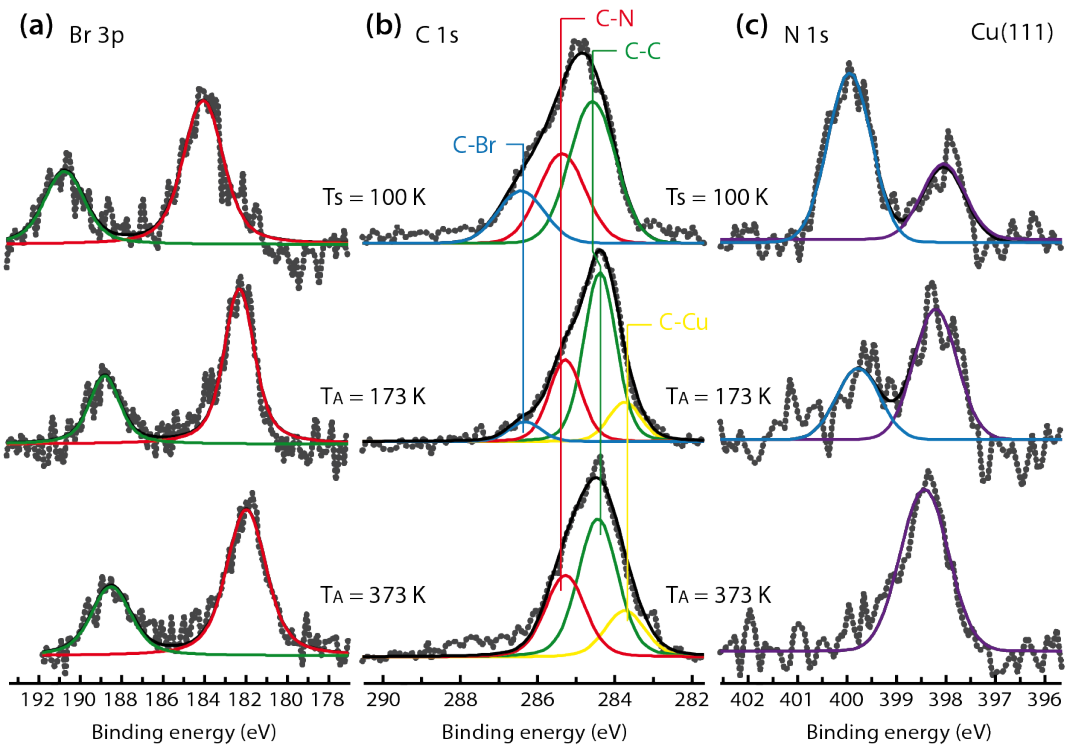


**Figure 3.38:** XP spectra of the Br 3p (a), C 1s (b), and N 1s (c) core levels of a submonolayer coverage of DBBQ on Cu(111) after deposition at 100 K (top), after annealing to 173 K (middle) and after annealing to 373 K (bottom).

The changes of the N 1s spectra are also similar to that on Ag(111). There are two peaks after deposition of DBBQ on the cold Cu substrate ($T_s$ = 100 K), centered at 398.1 eV and 400 eV, assigned to iminic N (=N-) and N interacted with Br, respectively, as discussed above. After annealing to 173 K, the intensity of the higher BE peak decreased. After further annealing to 373 K, this peak completely vanished, which means that the interaction between N and Br is no longer present. An alternative interpretation of the splitting of the N 1s spectra is presented below. The peak centered at 398.1 eV can be assigned to metal (here Cu) adatom coordinated CN species and the peak centered at 400 eV to uncoordinated CN species,[159-161] respectively. After annealing to higher temperatures, the intensity of the higher BE peak decreased and eventually vanished, which implies all the N coordinated with Cu adatoms. This scenario is consistent with the STM data, which show that most of the molecules after this temperature treatment can be found within extended chains. Therefore it is plausible to also propose that within these chains the monomers are linked both by C-Cu-C links, as well as N···Cu···N.

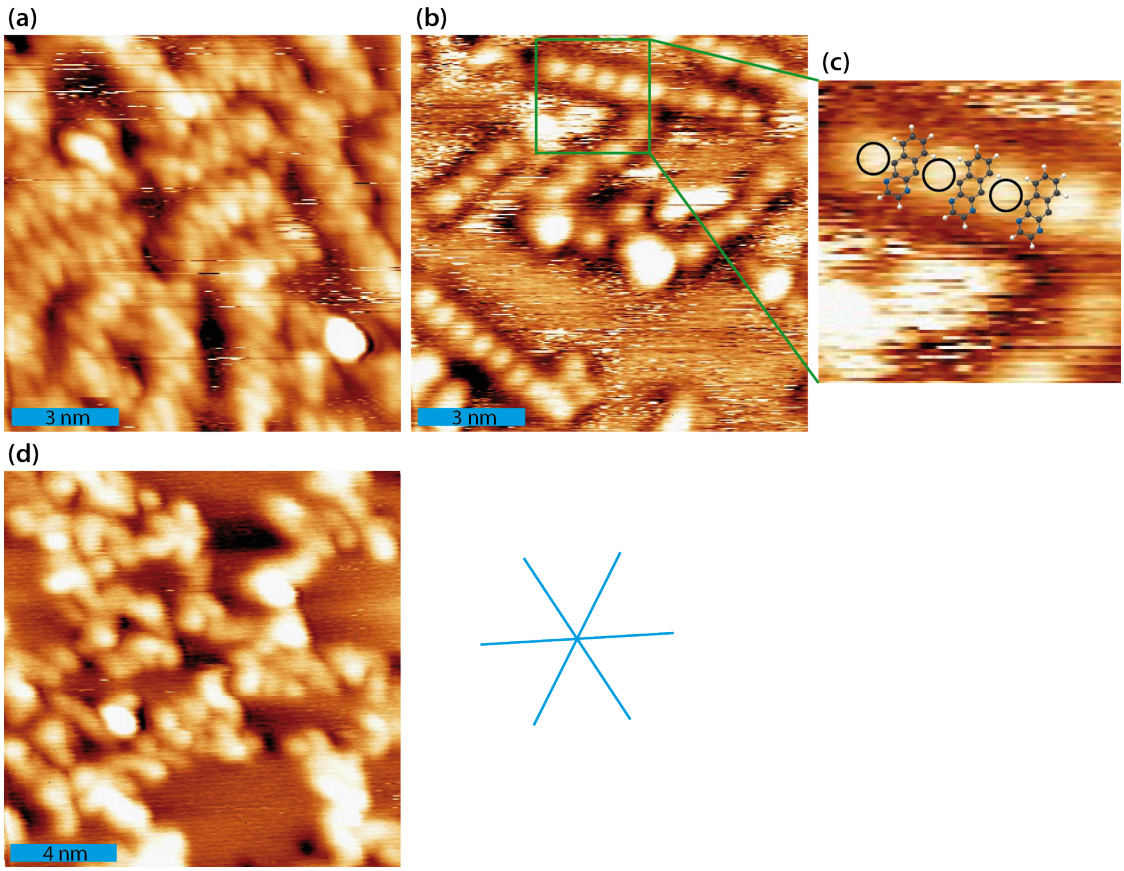


**Figure 3.39:** STM morphology of DBBQ molecules on Cu(111) after RT deposition (a) ($T_{STM}$ ~ RT, $U_s$ = -1.28 V, $I_t$ = -0.07 nA). (b) After annealing to 423 K ($T_{STM}$ ~ 210 K, $U_s$ = 1.25 V, $I_t$ = 0.11 nA). (c) Magnified image of the green box superposed with molecular models; black circles represent Cu adatoms. (d) After annealing to 503 K ($T_{STM}$ ~ RT, $U_s$ = 1.16 V, $I_t$ = 0.12 nA). The blue star indicates the high symmetry directions of the Cu(111) substrate.

**Figure 3.39** shows an STM image of DBBQ molecules on Cu(111) after RT deposition (a) and after annealing to 423 K (b). Similar molecular chains appeared consisted of debrominated DBBQ molecules interacting with Cu adatoms, yet without long-range order, displayed in **Figure 3.39**b. The molecular backbones also resembled along the high symmetry directions of the substrate. The halogen bonds are again not resolved in STM images. After annealing to 503 K, molecules aggregated on the surface and no ordered polymers can be observed.

### 3.2.2 Molecular behavior of DBBPP on Ag(111) and Cu(111)

#### 3.2.2.1 Investigation of DBBPP on Cu(111)

Firstly, we did XPS measurements to study the chemical state of the molecules after deposition.

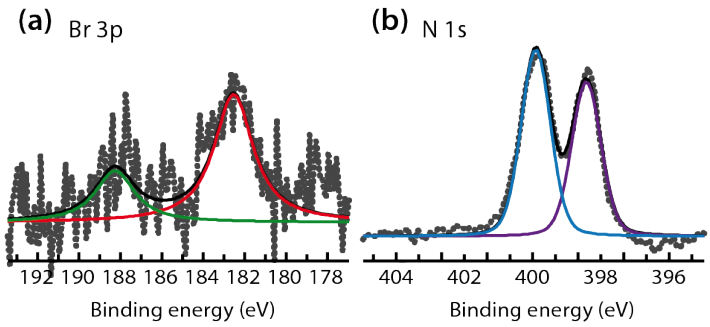


**Figure 3.40:** XP spectra of the Br 3p (a) and N 1s (b) core levels of a multilayer coverage of DBBPP on Cu(111) after RT deposition.

DBBPP debrominated after RT deposition on the Cu(111) substrate, but the debromination already occurred partially during sublimation of the compound in crucible before facing to the surface. This is explained by the relative intensities of the Br 3p and N 1s core levels (**Figure 3.40**) normalized for the photoionization cross-sections[162] of 1 : 13, far less from the molecular ratio of 1 :1. In the Br 3p XP spectrum (shown in **Figure 3.40**a) the peaks appear at BE typical for chemisorbed Br atoms after C–Br bond scission, indicating that all Br atoms are in the interface of the Cu surface and the multilayer film. In the N 1s spectrum, there are also two peaks with similar intensities, indicating that both contributions should be present within the multilayer. As Br is not present in the multilayer, this may indicate a reaction of the C radical with a portion of the iminic N at the multilayer.

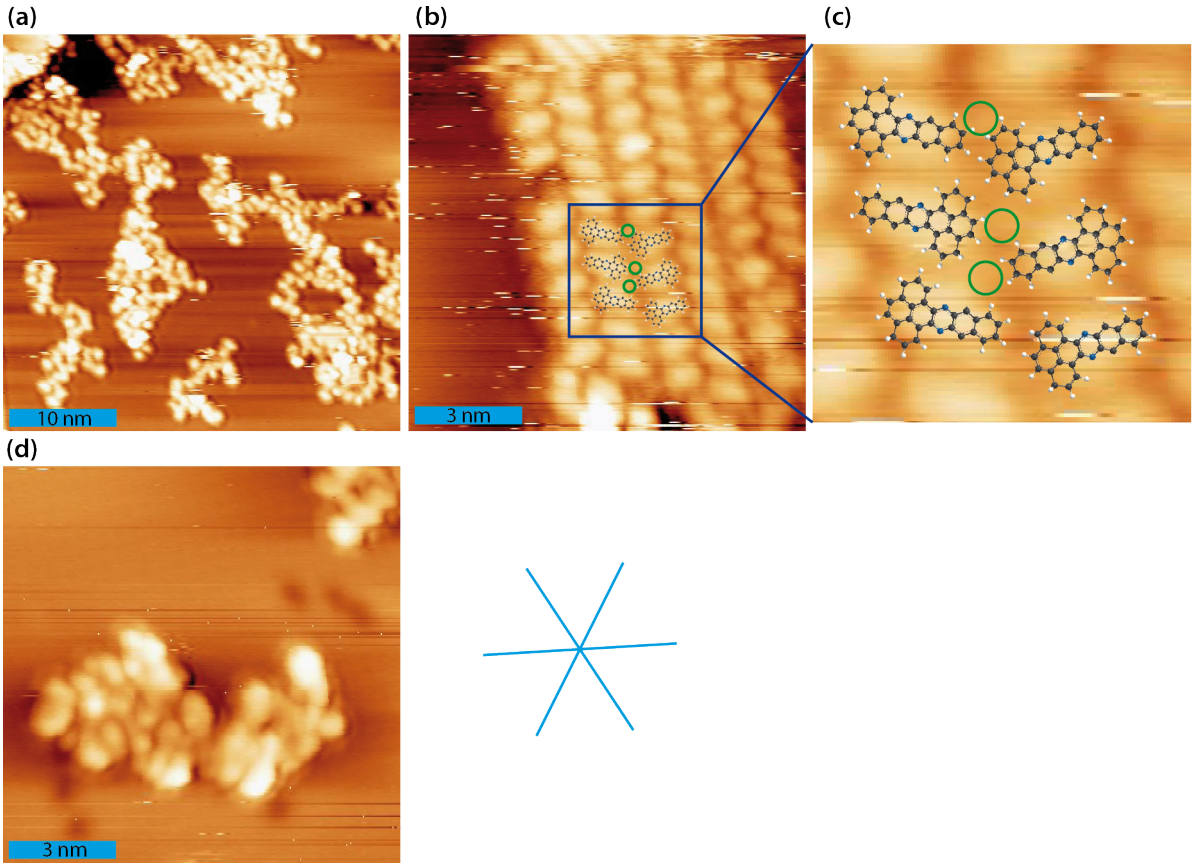


**Figure 3.41:** STM image of DBBPP on Cu(111) after RT deposition (a) ($T_{STM}$ ~ 130 K, $U_s$ = -1.25 V, $I_t$ = -0.08 nA) and after annealing to 430 K (b) ($T_{STM}$ ~ 130 K, $U_s$ = -1.36 V, $I_t$ = -0.07 nA). The green circles indicate Br atoms. (c) Magnified image of the blue box superposed with molecular models. (d) STM image of the aggregated molecules on Cu(111) after annealing to 560 K ($T_{STM}$ ~ RT, $U_s$ = 1.25 V, $I_t$ = 0.08 nA). The blue star indicates the high symmetry directions of the Cu(111) substrate.

After RT deposition, DBBPP molecules are randomly distributed on the Cu(111) substrate (**Figure 3.41**a). As inferred from XPS results, these molecules are already debrominated. After annealing to 430 K, these debrominated DBBPP molecules self-assembled regularly (**Figure 3.41**b). In between the adjacent rows, there are also Br atoms resolved as small dots highlighted in green circles. The proposed models for the stripe formation are shown in **Figure 3.41**c, where in the individual rows, DBBPP molecules align oppositely to each other due to the steric hindrance of the big side group. After further annealing to 560 K, molecules aggregated on the surface (**Figure 3.41**d).

### 3.2.2.2 Investigation of DBBPP on Ag(111)

In the following, we studied this molecule on the Ag(111) substrate. After RT deposition and annealing to 373 K, molecules adsorbed on the surface in a visually disordered way shown in **Figure 3.42**a. But the FFT analysis shown in **Figure 3.42**b reveals the real-space

image actually preserves long-range order with two symmetrically equivalent domains (green and red circles) appearing. The green arrow indicates the high symmetry direction of the substrate in reciprocal space. And the unit cell of the self-assembly of the molecules was measured to be 5.2-5.9 nm by 7.3-8.0 nm with an angle between them of 65-70° in the FFT of the real space STM images in **Figure 3.42**a, c. The accuracy of these measurements is estimated to be 20%.

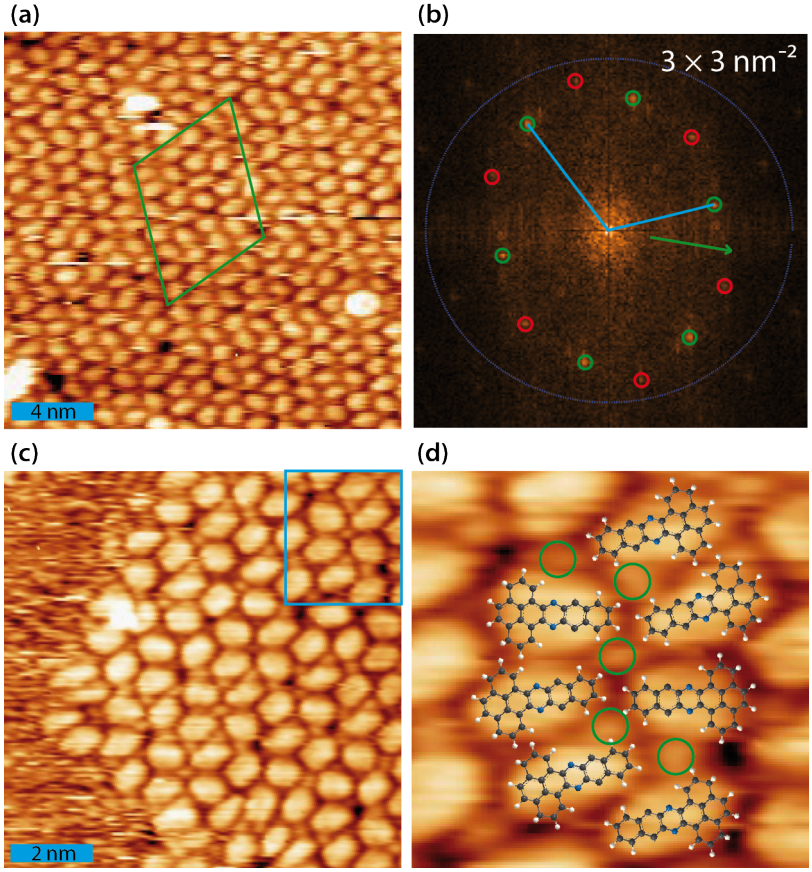


**Figure 3.42:** (a) Overview STM image of DBBPP molecules on Ag(111) after RT deposition and annealing to 373 K ($T_{STM}$ ~ 110 K, $U_s$ = -1.13 V, $I_t$ = -0.10 nA). (b) Zoom in the FFT of (a), the green arrow indicates the high symmetry direction of the reciprocal space. (c) Detailed STM image scanned after annealing to 373 K ($T_{STM}$ ~ 150 K, $U_s$ = 1.20 V, $I_t$ = 0.11 nA). (d) Magnified STM image of the blue box in (c), superposed with molecular models. Green circles represent Br atoms.

After annealing to 373 K, no big difference was observed and there is still no regular self-assembly of the molecules. From the detailed image shown in **Figure 3.42**d, we can see some Br atoms intermixed with debrominated molecules.

### 3.2.3 Summary and conclusions

In this chapter, we mainly studied two molecules: DBBQ and DBBPP on three different fcc (111) metal substrates aiming at the production of N-doped graphene nanoribbons through Ullmann coupling. Debromination occurs for both compounds on all three surfaces: Ag(111), Au(111) and Cu(111). For DBBPP molecules, debromination already occurs during sublimation in the crucible. An important result of this investigation is that a portion of the N atoms has a significantly different and unexpected chemical shift evidenced by the N 1s spectra. We tentatively rationalize this by proposing that N interacts strongly with either Br atoms (both attached to the molecule and chemisorbed on the surface) via halogen-nitrogen bonds or with surface metal adatoms. By annealing to higher temperatures, this interaction was weakened and eventually vanished.

On all three substrates, DBBQ forms metal-organic chains after RT deposition which maintained after annealing to moderate temperatures and have been proposed to be intermediates to the formation of covalent polymeric chains[21,125,163]. However, there are no regular polymeric chains observed under any circumstances. High-temperature annealing results in aggregated structures. This might be related to an interference of the halogen bonding between the N and Br. So the molecules can not form C-C bond before decomposing in carbonaceous species by higher temperature annealing.

## 3.3 N-Heterocyclic Carbenes on Solid Metal Surfaces: Bis-Carbene Metal Adatom Bonding Scheme of Monolayer Films on Au(111), Cu(111) and Pt(111)

Carbenes are currently considered a promising alternative to thiols for self-assembled monolayers (SAMs)[48] as well as metal-molecule junctions. They are thermally robust entities[49] with rich chemical reactivity[50,51] and predicted to have superior electronic conductivity to thiols.[52] Accordingly, an atomistic scale understanding of the adsorption geometry on solid surfaces and their mobility is essential in the design of such nanotechnology applications. In particular N-heterocyclic carbenes (NHC) are persistent carbenes which have enabled an acceleration in the aforementioned applications[54] and are developing in a very active research field.

Hitherto there are merely a handful of microscopy studies of NHC ligands on well-defined surfaces, and only two were able to address the assembly at the single molecule level.[74,164,165] All of these studies are carried out on the technologically relevant Au(111) surface, but although they assign protrusions of molecular dimensions in the STM images to upstanding NHC ligands, the overall surface morphology is markedly different. The samples prepared from solution showed significant surface pitting under the molecular layer, in good agreement with thiol SAMs on Au(111), and in one case, short range ordering of protrusions as close as 0.6 nm apart to each other.[74] The samples prepared in ultra-high vacuum (UHV) revealed high surface mobility at room temperature even for coverages close to monolayers[164] and excellent long range ordering at 77 K.[165]

In this chapter, we aim to systematically elucidate the chemical nature of these ligands by studying a prototypical NHC on three different substrates, Cu, Au, and Pt(111) under UHV conditions with a combination of microscopy and X-ray spectroscopy. We employed 1,3-dimethyl-1*H*-imidazol-3-ium-2-carboxylate as the precursor of the NHC 1,3-dimethyl-1*H*-imidazol-3-ium-2-ide (IMe, **Scheme 3**), which (as recently demonstrated)[165] in UHV produces free IMe after heating of the solid powder to ~ 393 K. The carbene molecule was chosen so as to minimize the impact of possible steric hindrance from the side groups (here methyl, instead of phenyl, mesityl or isopropylphenyl which were also explored in the aforementioned studies)[166] as well as being able to discriminate better the C 1s core level binding energy of the carbene (here corresponding to 20% of the total C 1s signal against 4.7-6.6% for the other NHC investigated by STM).

**Scheme 3.** Decomposition of 1,3-dimethyl-1*H*-imidazol-3-ium-2-carboxylate to 1,3-dimethyl-1*H*-imidazol-3-ium-2-ide (IMe) and carbon dioxide under UHV by heating to 393 K.

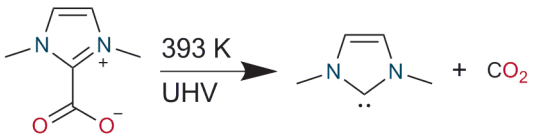


### 3.3.1 Self-Assembly of IMe on the Cu(111) Substrate

Firstly, we studied the molecular behavior of IMe on Cu(111). After deposition of IMe on Cu(111) at room temperature, a densely packed layer appeared on the surface as shown in **Figure 3.43**a. One can identify bright round protrusions arranged in dimers connected with a thin, dimmer waist (examples outlined in yellow). Each protrusion is consistent with the expected dimensions of a single planar IMe. On metallic surfaces, NHCs are generally reported to form metal carbenes directed perpendicular to the surface plane.[48,54,164,165,167,168] Besides the two unpaired electrons, the free NHC employed contains no other moieties which could be anticipated to give rise to directional attractive interactions, such as hydrogen bonding.

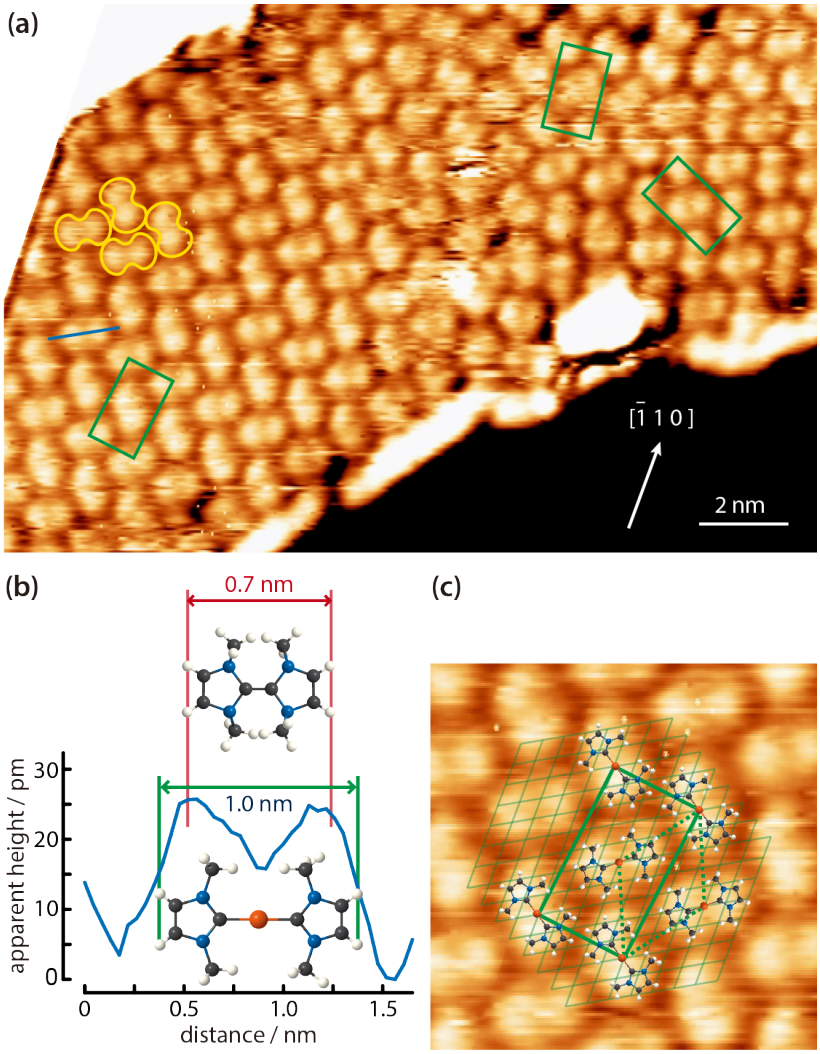


**Figure 3.43:** STM observations of IMe on Cu(111). **(a)** STM image ($T_{STM}$ = 100 K, $U_s$ = 1.58 V, $I_t$ = 0.11 nA) of a densely packed layer of dimeric NHC-Cu-NHC complexes (examples outlined in yellow) on Cu(111). The unit cell of the overlayer structure is shown in green. The Cu [$\bar{1}$10] direction is indicated. **(b)** Line profile across a dimer – cf. blue line in (a) - compared with the ball-and-stick models of a tetraazafulvalene (top) and a $(IMe)_2Cu$ (bottom) unit. **(c)** Zoom in STM image (4.5×4.5 $nm^2$) of the left domain in (a) superposed with molecular models, the underlying Cu(111) lattice (thin lines), the overlayer lattice (thick rectangle) and the Cu adatom lattice (dotted line). C, N, H, and Cu atoms are represented by black, blue, white, and orange spheres, respectively.

Two different possibilities may account for the observed dimerization. Either the carbene moieties react to yield a tetraazafulvalene[169,170] (**Figure 3.43**b top) or a surface Cu adatom reacts with two carbene molecules to form an organometallic $(NHC)_2Cu$ compound. The former is a rather elusive, non-planar species,[169] whereas complexes of Cu and NHC have been obtained already by solution chemistry and found to have the imidazole rings nearly coplanar, arranged opposite each other.[171] The room temperature incorporation of copper substrate atoms in the formation of metal-organic complexes and/or networks originating

from halogenated precursors,[127,172,173] thiolates,[174] and pyridyl moieties,[175] is well documented on the Cu(111) surface. The difference in the distance of the C atoms of the two linked IMe moieties in the case for a direct carbene-carbene bond, or a carbene-Cu-carbene bond is 0.25 nm. The resulting length of the dimer would be 0.74 nm in case of tetraazafulvalene formation vs. 0.99 nm in the case of $(IMe)_2Cu$. **Figure 3.43**b compares a line profile across a dimer which measures ~ 1.00 nm, with the structural models of a tetraazafulvalene[72] and a $(IMe)_2Cu$,[73] showing that the latter is a much better fit. Moreover, in the tetraazafulvalene molecule, the two rings have a reported dihedral angle of 7.4°, resulting in opposing methyl groups having a difference of 0.23 nm in height.[72] No evidence of such an asymmetry in the apparent height is evident in the STM images. The C 1s signal of such a surface (cf. 'Spectroscopic signatures of IMe on Cu(111) and Au(111)') further support the formation of $(IMe)_2Cu$. The observed STM contrast, whereby the inserted Cu atom is not particularly bright in comparison to the NHC, is consistent with observations of Cu coordination with carbonitrile groups[176,177] with deprotonated amine groups[111,178] and within tetrapyrrole compounds.[179,180]

We further note that a spontaneous imaging change can occasionally be found, whereby the dimer protrusions can be resolved as single protrusions, i.e. imaging of the central Cu atoms instead, which can be illustrated by STM images of the same area in **Figure 3.44**. Such a change might occur due to a tip apex conformational change or adsorbed molecules on the tip alternating its imaging behavior.

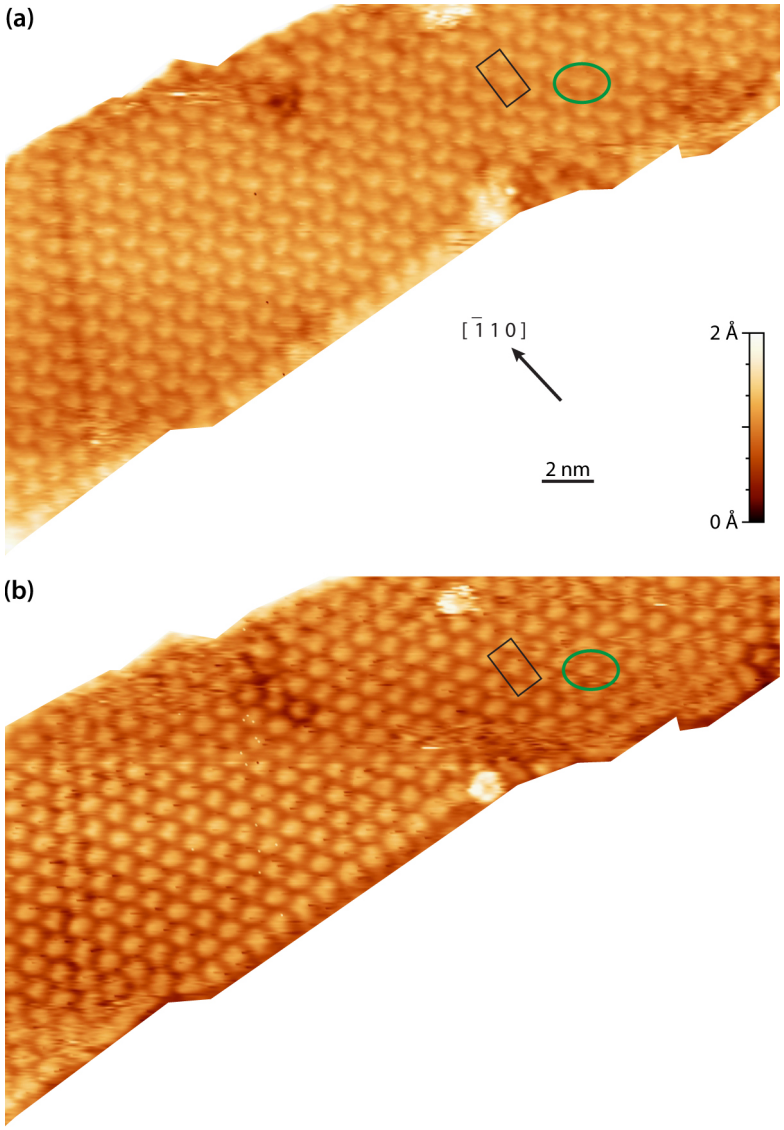


**Figure 3.44:** Consecutive STM images of $Cu(IMe)_2$ on Cu(111) revealing different contrast of the $Cu(IMe)_2$ units. (a) In $Cu(IMe)_2$ (example circled in green), the IMe moieties are imaged. Note that the lateral resolution does not allow a clear distinction of the two IMe in the same complex at this scale. The high symmetry axis of the substrate and the unit cell are indicated. ($T_{STM}$ = 98 K, $I_t$ = 0.08 nA, $U_s$ = −1.58 V) (b) Here each complex (example circled in green) is imaged as a more bright and round protrusion centered at the Cu atom of the complex. ($T_{STM}$ = 98 K, $I_t$ = 0.09 nA, $U_s$ = −1.58 V)

Detailed structures are shown in **Figure 3.43**c, where molecular models are overlaid on the STM image. The dimers arrange in a zig-zag fashion to form a two-dimensional crystalline layer. This is characterized by a rectangular unit cell which contains two dimers (indicated in green). The dimensions of the unit cell are measured to be approximately 1.7-1.9 nm and 0.9-1.1 nm, whereas the angle between the unit cell vectors is 85°-90°. The long axis of the overlayer unit cell was estimated to be rotated by ~ 8° with respect to the underlying Cu(111) high symmetry axis. The dimers appear with equal apparent height,

hinting at equivalent adsorption sites.[181] Considering that all the centers of the dimers (i.e. the Cu adatoms) are located in equivalent adsorption sites, within the range and accuracy of our measurements the monolayer structure of $(IMe)_2Cu$ can be described by the epitaxy matrix $\begin{pmatrix} 7 & -1 \\ 3 & 5 \end{pmatrix}$. **Figure 3.43**c shows the proposed epitaxial model of $(IMe)_2Cu$ superposed on the STM image. The $(IMe)_2Cu$ complexes are placed in equivalent adsorption sites, and the angle between the long axes of the dimers is 72°; however reasonably good matching can be obtained for angles in the range of 60° to 90°. At the borders of the domains, dimers of fainter contrast are observed, indicating a high mobility under these measurement conditions (with a substrate temperature of 100 K). Three symmetrically equivalent unit cells with respect to the underlying Cu lattice can be found on the same atomically flat terrace imaged in **Figure 3.43**a (indicated in green). We note that we also observed single domains extending over the complete atomically flat areas as shown in **Figure 3.44**.

### 3.3.2 Self-Assembly of IMe on the Au(111) Substrate

In the context of the stable formation of dimer of NHCs with Cu, we revisit the interpretation of the experiment featuring the same NHC molecule on Au(111). **Figure 3.45**a is an overview of a surface saturated with IMe at room temperature consistent with previous work.[165] The chevron structure of the Au(111) substrate underneath is clearly discernible. The periodicity of the fcc-hcp domain walls along the $[\bar{1}10]$ Au direction is noticeably affected. In our data it was measured to vary between 6.3 and 7.9 nm, instead of 6.3 nm for the pristine Au(111) surface in vacuum.[182] Such gradual lifting of the Au(111) herringbone reconstruction concomitant with the extraction of the extra Au surface atoms has been observed upon adsorption of $NO_2$[183] and trimethylphosphine,[184,185] respectively. However, in contrast to earlier works, as well as for another NHC on Au(111),[164] no islands related to these extra Au adatoms were found. For example, the periodicity of the fcc-hcp domain walls in **Figure 3.45**a is ~ 7.5 nm. A dense packed island of extra adatoms of the reduced reconstruction in **Figure 3.45**a would be expected to have a radius of ~ 2.0 nm. Depressions also appear commonly on the elbow sites (see **Figure 3.45**a).

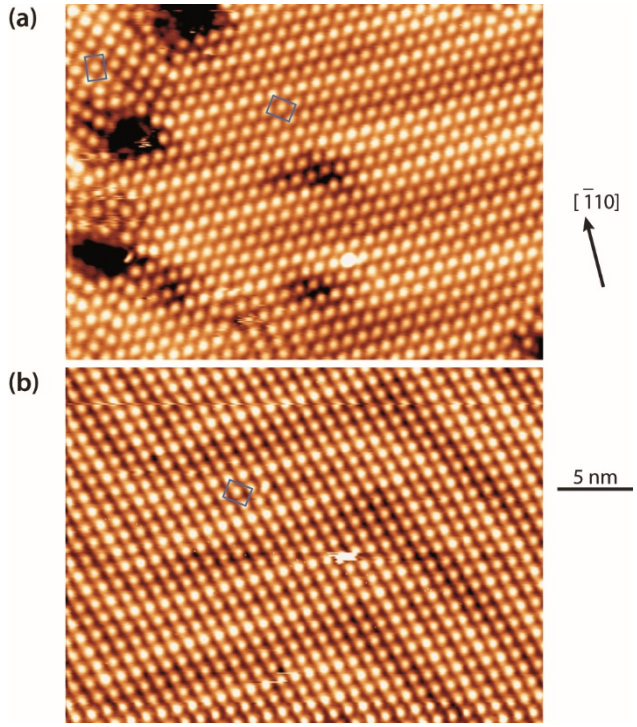


**Figure 3.45:** Overview STM images of a saturation coverage of IMe on the Au(111) surface (a) following deposition at room temperature ($T_{STM}$ = 100 K, $U_s$ = 1.63 V, $I_t$ = 0.08 nA) and (b) annealing to ~ 330 K ($T_{STM}$ = 150 K, $U_s$ = 1.44 V, $I_t$ = 0.09 nA). The scale bar corresponds to 5 nm. The unit cell of the overlayer structure is shown in blue and the Au [$\bar{1}$10] symmetry direction is indicated.

We note that the Au adatoms originating from the extracted atoms of the relaxed periodicity of the soliton walls and the elbow sites are reasonably expected to be incorporated in direct bonding with NHC units and another possible source of Au adatoms is the intrinsic thermally activated adatoms. The unit cell of the IMe assembly was measured in different images to be 1.1-1.2 nm by 1.6-1.8 nm and an angle of 87° to 90°.

After mild annealing to ~ 330 K, we notice an improved ordering of both the Au surface and the surface overlayer (**Figure 3.45**b). The herringbone reconstruction appears more regular and no pitting appears at the elbow sites, whereas the molecular layer shows single domains wetting different orientations of the soliton walls and the elbows. This indicates that the unit cell has a certain degree of flexibility, so as to maintain its direction upon a change of the soliton wall direction. The epitaxy matrix $\begin{pmatrix} 1 & -5 \\ 5 & 3 \end{pmatrix}$ on the herringbone reconstructed Au(111) results in inequivalent unit cells, depending in the orientation of the reconstruction. These are unit cells with sides within the range of 1.5-1.6 nm by 1.2-1.3 nm and angles of 85°-90° between them. Crucially, it is consistent with the observed

orientations of domains and results in each bright protrusion appearing in equivalent adsorption site.

The dimensions of the unit cell and the density of the bright protrusions are strikingly similar to that of the $(IMe)_2Cu$ on Cu(111) presented above. We further note that the asymmetry between the two different protrusions in the unit cell is very faint in our STM images (**Figure 3.46**a), however was more clear in the higher resolution data reported earlier.[165] Previously, each bright protrusion was ascribed to an upstanding (IMe)Au complex (see **Figure 3.46**b), which was free to diffuse on the surface at room temperature, whereas at low coverages, isolated almost planar bis- and tris-carbene gold complexes were clearly identified on Au(111), by imaging as bright protrusions both the IMe ligands and the Au adatom (**Figure 3.46**a).[165] Au adatoms in planar metal organic complexes are commonly the most outstanding features in STM images as can be seen for methyl thiolate gold complexes on Au(111).[186]

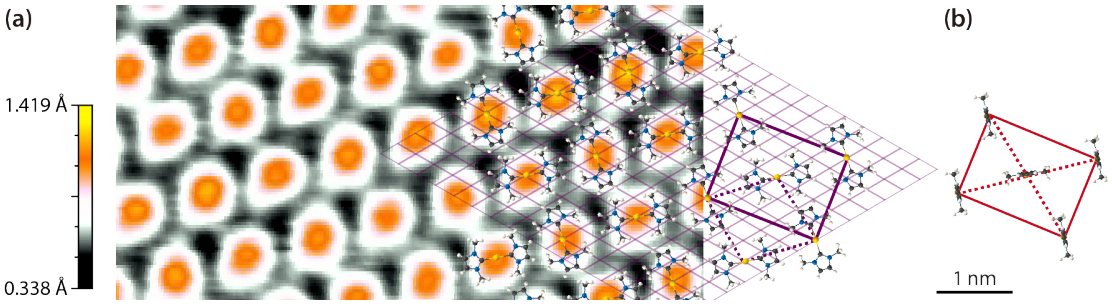


**Figure 3.46:** (a) Zoom in STM image of a saturation coverage of IMe on Au(111) ($T_{STM}$ = 100 K, $U_s$ = 1.62 V, $I_t$ = 0.10 nA) overlayed with proposed molecular model of $(IMe)_2Au$ analogous to the observation of $(IMe)_2Cu$ Cu(111). The thin lines indicate the substrate unit cell, the thick solid lines the overlayer unit cell and dotted lines the Au adatom lattice. (b) Reported unit cell and top view of the previously proposed molecular model of the same assembly,[9] drawn in the same scale as for our work. C, N, H, and Au atoms are represented by black, blue, white, and yellow spheres, respectively.

An upstanding geometry of (IMe)Au complexes in the dense packed structure observed results in a density of 1 IMe per 0.9 $nm^2$ (**Figure 3.46**b),[165] which is approximately half the density of NHC on the Cu(111) surface shown above (1 IMe per 0.56 $nm^2$). Hence the upstanding configuration does not seem to enhance the packing density, a driving force for upstanding configuration in self-assembly,[187] weakening the plausibility of the previously proposed model.[165] The results thus point to $(IMe)_2Au$ formation, like the corresponding $(IMe)_2Cu$ on Cu(111). This interpretation is in good agreement with the reported reaction of an NHC with gold nanoparticles which results in bis-carbene gold(I) complexes.[74] Additionally, parallels can be drawn with the formation of "staple" motifs (i.e. the stapling

of a Au atom by two opposing ligands) with the less sterically imposing thiolate, methyl thiolate: this is consistently found to be energetically favored on the Au(111) facets.[188]

### 3.3.3 Spectroscopic signatures of IMe on Cu(111) and Au(111).

To compare the interaction of the IMe with the Cu and Au surfaces we performed XPS investigations after deposition of IMe at room temperature on both surfaces (**Figure 3.47**). No oxygen signal was detected in either case, consistent with the $CO_2$ group being abstracted from the IMe precursor and not interacting with the surfaces. The purple lines in **Figure 3.47** correspond to the C 1s and N 1s core levels of a saturation coverage of IMe on Au(111). The N 1s spectra (**Figure 3.47**b) show the same peak with binding energy of 401.1 eV. This is in-between the binding energies of a neutral (399.2-400.5 eV)[106,189,190] and a protonated (402.0 eV)[106] amino group on a metal surface. It can therefore be deduced that some positive charge is present in the N atoms in this configuration.

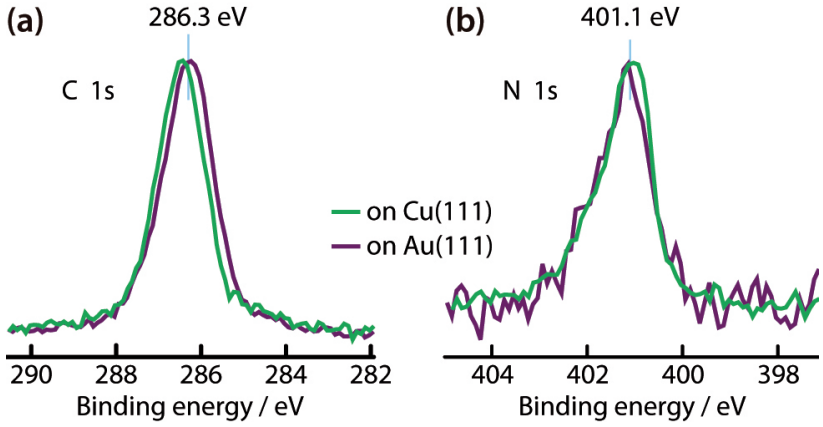


**Figure 3.47:** XP spectra of IMe on Cu(111) (green lines) and on Au(111) (purple lines). (a) C1s and N 1s core levels. The spectra are normalized in intensity for easier comparison.

The C 1s appears a single peak with full width at half maximum of 1.4 eV (**Figure 3.47**a). No clear discrimination can be made between the different C atoms within this peak. The observed binding energy of ~ 286.3 eV is in good agreement with literature values of C atoms bonded to N atoms.[150] However, the C atom of the carbene, being connected to two N atoms, should have a higher binding energy by ~1.5 eV with respect to the C atoms connected to a single N atom,[191] and since it contributes for 20% of the signal intensity it would be expected to be clearly discernible. On the other hand, the formation of a C-metal adatom bond is expected to result in a downshift of ~1 eV.[138] The appearance of a single peak is indicative of the formation of an organometallic bond with the carbene atom, corroborating our assignment of the dimers on Cu(111) to $(NHC)_2Cu$. Importantly, both

core levels have the same binding energy (within 0.1-0.2 eV) and shape on both Au(111) and Cu(111), as expected for molecules showing the same interaction pattern with the supporting surfaces. On Cu(111) planar IMe dimers are directly visualized, hence on Au(111) the IMe moieties are expected to be planar as well.

### 3.3.4 Self-Assembly of IMe on the Pt(111) Substrate

Further, we investigated the bonding of NHCs on a more active metal surface Pt(111). **Figure 3.48**a shows an overview of the topography after dosing NHCs on Pt(111) at room temperature, recorded at 93 K. On Pt(111), NHC also coordinated with Pt adatoms forming dimeric $(NHC)_2$-Pt species, which can be demonstrated by statistic histogram (in **Figure 3.48**c) of the molecular length measured by line profiles taken on molecules with characteristic of faint imaging center and two bright protrusions. Combined with a normal distribution curve, we can show that the approximate length is 0.98 ± 0.02 nm, which is the right value for the length of $(NHC)_2$-Pt dimer[192].

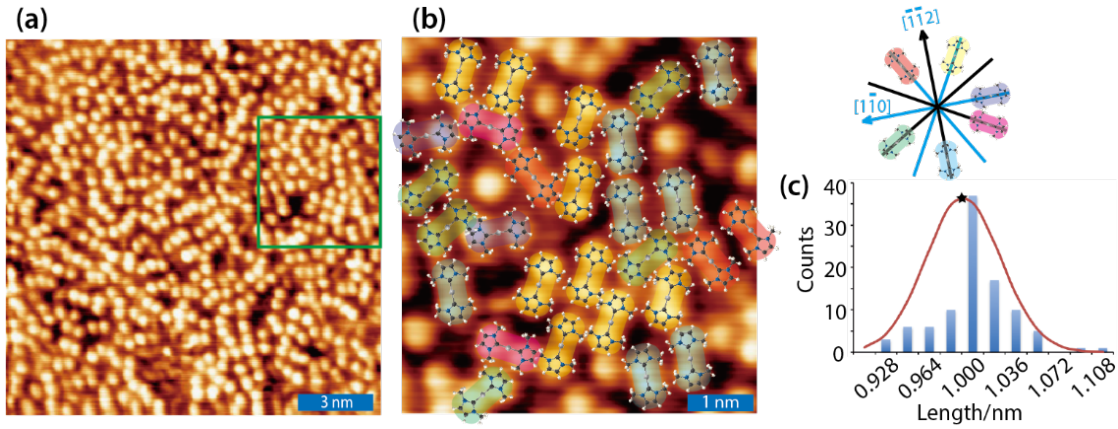


**Figure 3.48:** (a) Overview of the irregular arrangement of NHC on Pt(111) recorded at 93 K ($U_b$ = 1.25 V, $I_t$ = 0.10 nA). (b) Magnified STM image ($U_b$ = 1.25 V, $I_t$ = 0.12 nA) of the area marked in the green box in (a) overlaid by a color coded orientational distribution map of the generated $(NHC)_2$-Pt dimers combined with molecular models. The Pt(111) high-symmetry axes are indicated in blue star and the diagonal directions indicated in black. (c) Statistic histogram and normal distribution of the length of the dimeric NHC-Pt complexes.

The detailed structures of the area marked in green box are presented in **Figure 3.48**b, where molecular models are overlaid on the STM image. Besides, we made a color coded orientational distribution map of the generated $(NHC)_2$-Pt dimers. From that we can see clearly that these dimers either register on the three high-symmetric directions of Pt(111) substrate, or in the diagonal directions. Thus a substrate-induced specific orientation of the

individual dimers can be assumed, but there is no obvious regular pattern for the preferential alignment direction.

This randomly oriented allocation is probably due to a strong molecule-substrate interaction[193-195]. So the carbene complexes can not move freely on the surface like what we observed on Au(111) and Cu(111).

### 3.3.5 Summary and conclusions

In this chapter, We investigated the saturated monolayers of a sterically not imposing NHC on Cu(111), Au(111), and Pt(111) single crystal surfaces under well-defined, UHV conditions. At room temperature the free carbene forms clearly identifiable dimers on Cu(111), which are assigned to planar NHC "stapled" by a Cu adatom. We found a remarkably similar packing on Au(111) and identical spectroscopic signatures of the C 1s and N 1s core levels of the IMe on both surfaces. We therefore deduced that also on the technologically important Au(111) surfaces, the planar bis-carbene metal formation is preferential under our conditions even at high coverages. It is thus appropriate to draw attention to the possibility of such bidentate motifs at high coverages and expect that a complex landscape might emerge for the exact control of the adsorption geometry of carbenes on solid surfaces, kindred to the adsorption of thiolates on Au(111).

On the more active surface Pt(111), dimeric $(IMe)_2$-Pt species also generated and these dimers either register on the three high-symmetric directions of Pt(111) substrate, or in the diagonal directions, however, there is no long range order.

As carbene ligands can bind and stabilize a plethora of metals they are currently deemed as promising protean surface anchors, thus our findings are expected to be of relevance to the rational engineering of modifications of extended surfaces and nanoparticles.

## 3.4 Interaction of Cyclosporin A with different metal centers: alkali metals vs. transition metals

A number of natural cyclic peptides have been used for their antibiotic, antitumor and immunosuppressive properties[196-198], partly due to their higher stability against decomposition with regard to their linear counterparts[199]. Due to their chemical conformation and functional diversity, cyclic peptides are considered as versatile molecular building units for emerging nanodevices.[55-57] In biological systems, some cyclic peptides can selectively transport metal ions.[196,200] Mimicking nature, both natural and synthetic cyclic peptides could be developed to interact with ions in their centers or on specific residues[58], a desirable property for functional structures[201,202]. In contrast to other commonly employed nanotechnology materials, such as carbon nanotubes, cyclic peptides offer several advantages like biological compatibility, ease of functionalization *via* structural diversity; therefore they are suitable for different applications in biochemistry, chemistry, biology, materials science, and medicine.[203]

A variety of techniques, such as NMR, XRD, and molecular dynamics simulations, have been applied to study structural properties and ion transport mechanisms of macrocyclic peptides.[204,205] These experimental studies on the functionalities of cyclic peptide structures average over the whole molecular ensemble, lacking detailed information on the single molecular level. It is plausible to envision that studying cyclic peptides at the single molecule level could lead to beneficial insights into the functionalities of this important type of peptides. However, single-molecule observation of macrocyclic peptides is still a challenge. Although most studies of cyclic peptides are done in solvent, UHV–STM can provide information with *in situ* probing the varying geometric and electronic structure of biomolecules in a clean and less interfering environment,[206,207] and is capable to address macrocyclic peptides at subnanometer level.[208,209] Compared with STM in ambient conditions, cyclic peptide molecules can directly adsorb on the metal substrate in UHV without co-assembly of a template network, which might influence potential molecular configuration changes.[210]

**Scheme 3.4.** Chemical structure of CsA.

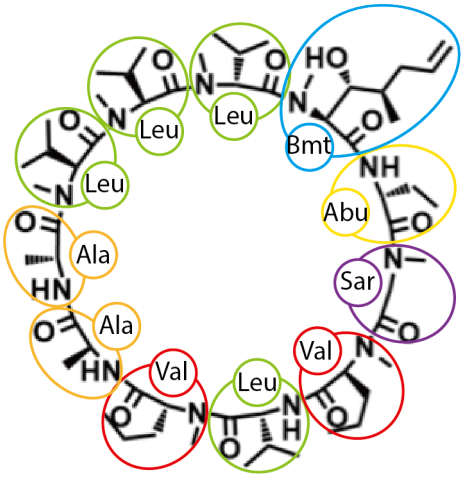


In this section, we investigated cyclosporine A (CsA, **Scheme 3.4**) inspired by the multitude of its biological functionalities. CsA is an immunosuppressant drug widely used in organ transplantation to prevent rejection:[211,212] It reduces the activity of the immune system by interfering with the growth of T cells. Moreover, CsA may cause potassium retention in kidney associated hyperkalemia and kidney dysfunction, which means that potassium may interact and lead to the conformational changes of CsA and/or the formation of potential biomaterials. For comparison, we also investigated the coordination of transition metal atoms (iron and cobalt) to surface-supported CsA molecules. This study will be essential for elucidating interactions of cyclic peptides with both alkali and transition metals.

### 3.4.1 Molecular configuration and self-assembly of Cyclosporin A on Cu(111)

CsA contains 11 amino acids (**Scheme 3.4**), and the MeBmt residue [213] (circled in blue in **Scheme 3.4**) has a longer side group with a chain of five carbon atoms terminated with an alkene. As support, a coinage metal surface has been employed in forming adsorbate-substrate system with various molecules. Copper has been successfully used to support chiral organization of adsorbed amino acid and dipeptides.[214,215] Hence, the Cu(111) was chosen in order to immobilize the adsorbed CsA molecules as on the more inert Au (111) surface the CsA molecules were too mobile on the plain surface and could only be pinned on the step edges under our conditions.

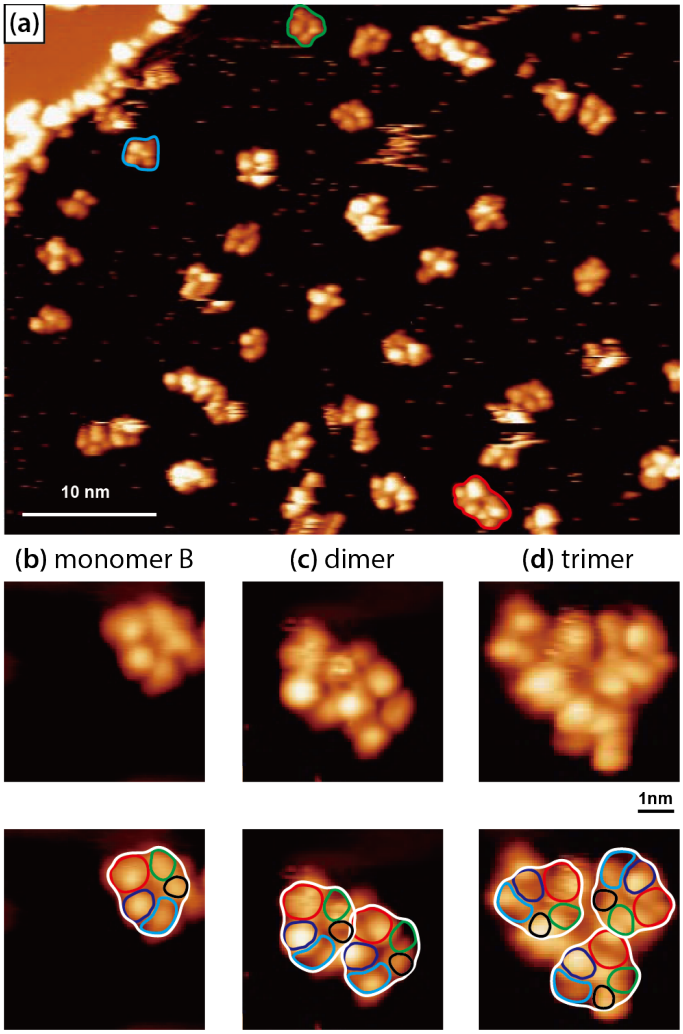


**Figure 3.49:** STM of CsA molecules on the Cu (111) surface. (a) Typical large scale image. Two kinds of monomers, types A and B, can be identified as irregular polygons and indicated by the blue and green circles, respectively ($U_s$ = -2.09 V, $I_t$ = -0.07 nA). (b-d) High resolution images in the same scale: (b) a monomer type B ($U_s$ = -2.43 V, $I_t$ = -0.06 nA), (c) a dimer composed by two monomers type B ($U_s$ = -2.51 V, $I_t$ = -0.08 nA), (d) a trimer composed by three monomers type B ($U_s$ = -2.43 V, $I_t$ = -0.08 nA). In the bottom row the bright protrusions assigned to different groups of amino acids are circled in different colors.

**Figure 3.49** displays a typical large scale STM micrograph of CsA adsorbed on Cu(111). Two types of CsA adsorption appearances can be distinguished from high resolution images (A and B in **Figure 3.50**) with individual CsA molecules observed as irregular polygons. The diameters of the single CsA molecules dispersed on the surface of Cu(111) were measured to be 1.6 ± 0.3 nm (**Figure 3.49**), consistent with neutron scattering experiments data[216] and the static individual CsA molecules observed on the Au(111) surface. Additionally we observed compact assembly of oligomers such as dimers (**Figure 3.49**c) and trimers (**Figure 3.49**d). They are presumably stabilized by hydrogen bonding between the amino groups (-NH-) and carbonyl groups (-C=O). The amino groups and carbonyl

groups are distributed evenly on the CsA cycle, which gives rise to a plethora of possible interaction positions of the eleven residues of the cyclic peptide leading to a variety of dimer and trimer configurations (**Figure 3.49**a).

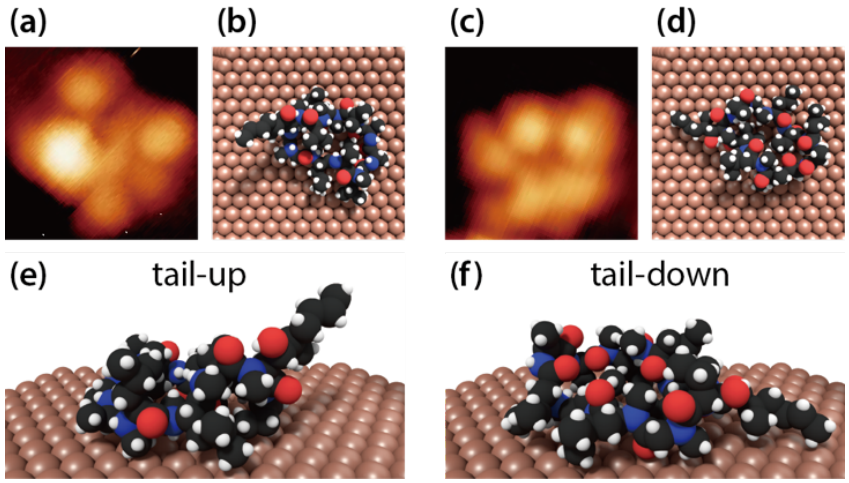


**Figure 3.50:** Adsorption configurations of CsAon the Cu(111) surface. (a,c) STM zoom in monomer (a) type A ($U_s$ = -2.75 V, $I_t$ = -0.08 nA) and (c) type B ($U_s$ = -2.43 V, $I_t$ = -0.08 nA). (b,d,e,f) Corresponding simulated adsorption of CsA with (b,e) tail-up and (d,f) tail-down, shown in (b,d) top view and (e,f) side view.

By simulating the two types of adsorption configuration A and B (**Figure 3.50**), we can propose tentative adsorption scenario. Both configurations are characterized by five to six bright protrusions, indicating submolecular resolution though not single residue resolution, in accordance with other STM studies of peptides on surfaces.[206,208,209] Because all the side groups of CsA are alkyl or alkene chains with similar electronic density of states, the contrast variation on the irregular polygonal ring could be associated with the topographic difference of the side chains. Thus, the part with the high apparent height on the peptide cycle should be attributed to the longer side group at residue MeBmt in **Scheme 3.4**. CsA molecules with the longer side group in different direction appear as two types of monomers with different adsorption configurations. The monomer in **Figure 3.50**a appears as a polygon with a brighter spot at one of its corners in the STM image. The monomer in **Figure 3.50**c appears as a polygon with a central cavity and a protrusion at one of its corners in the STM image. The contrast variation of the irregular polygonal ring could be associated with the topographic difference of the side chains. We simulated the adsorption process of CsA on Cu (111) assuming an “up” and “down” configuration of the tail as shown in the space filling models in **Figure 3.50**. Monomer A in **Figure 3.50**a matches well with the “tail-up” configuration where the alkyl chain points away from the Cu (111) surface, whereas monomer type B in **Figure 3.50**c matches the “tail-down” configuration

with the alkyl chain lying close to the Cu (111). The relative frequencies of the monomers were 24.8% tail-up and 75.2% tail-down.

### 3.4.2 Interaction of Cyclosporin A with different metals: K, Fe, and Co

It is well-known that cyclic peptides can function as ion channels forming ionophores. Since CsA can cause potassium retention, potassium may be a metal center which interacts with CsA. Potassium was introduced gradually to the Cu(111) surface covered with CsA molecules. **Figure 3.51** shows a typical STM micrograph of the CsA molecules after dosing potassium for a minute (amount ca. 3 atoms per molecule). One can notice that some CsA molecules appear filled and others empty. The potassium atoms lead to an appearance change from an irregular polygonal to a nearly triangular shape (**Figure 3.51**e).

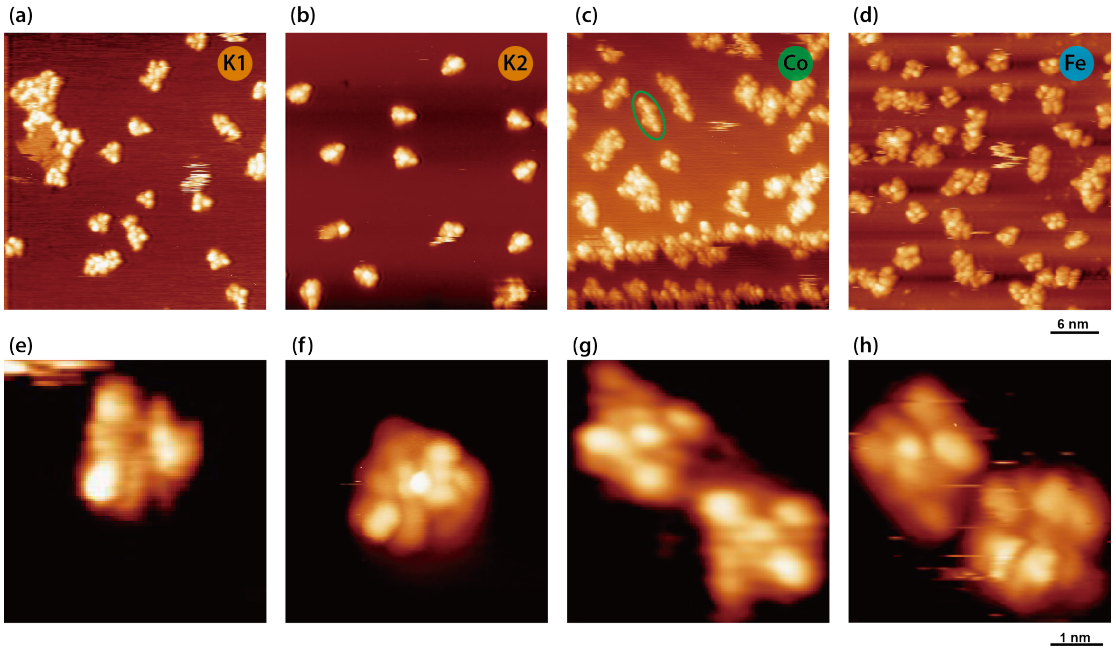


**Figure 3.51:** The interaction of CsA with alkali metals: K and transition metals: Fe and Co on Cu (111). (a) STM image of CsA with K at low K coverage. (e) Non-uniform triangle of CsA monomer with more bright spots. (b) Interaction of CsA with K at high K coverage. (f) Uniform triangle of CsA monomer with three bright spots on top. (c) Interaction of CsA with Co. (g) CsA monomer with bright spots in the center. (d) Interaction of CsA with Fe. (h) CsA monomer with bright spots in the center or on the macrocycle.

**Figure 3.51**e is the high resolution STM image of a CsA monomer with increased bright spots (from 5 to 9 protrusions of non-uniform apparent height) on the peptide circle. **Figure 3.51**b shows the morphology of the surface after dosing three times amount of potassium. The configuration of CsA changed to uniform teardrops containing eleven protrusions and exemplifying the filled center (**Figure 3.51**f), providing supportive evidence of the

formation of CsA-K complexes. The apparent average area of the CsA-K complex is slightly expanded from 0.249 $nm^2$ to 0.292 $nm^2$. So we may conclude that the cyclic peptide can coordinate and accommodate an increased number of K atoms within their cavity, and we propose that K binds exclusively to amide carbonyl oxygen atoms in the CsA, in a similar scenario as observed with the K coordination of the six carbonyl oxygens from the valine groups of cyclic peptide-valinomycin.[217] In the case of CsA, intramolecular (instead of intermolecular) carbonyls are gradually "pinched/stapled" together with the increasing K atoms, leading to different CsA configurations. And also, as increasing K dosage, more and more monomers were observed.

We further investigated the interaction of CsA with the transition metals iron and cobalt. Evidence for iron atoms could be found both on the center and on the side chains of CsA (**Figure 3.51**h). Increasing the amount of Fe, the configuration did not change so much, indicating that the Fe uptake is more limited in comparison to the K uptake. Similarly, the cobalt atoms can enter into the CsA macrocycle, shown as bright spots in the center (**Figure 3.51**g) and induce uniform conformation changes of CsA monomers. More interestingly, well-defined CsA-Co-CsA dimers could be found indicated in green circle in **Figure 3.51**c.

### 3.4.2 Summary and conclusions

In summary, we have investigated CsA on Cu(111) under well-defined conditions with submolecular resolution. Two kinds of configurations of CsA on Cu(111) have been elucidated by real-space imaging and molecular modeling. Distinct phase transformations were monitored after dosing three different metals. Potassium atoms prefer complexing within the center of CsA and saturate its hydrogen bonding sites. As increasing the coverage of K atoms, CsA-K complexes transformed into uniform triangular species and more and more monomers were observed. Iron atoms may also coordinate with carbonyls of the CsA either sitting in the macrocycle of the CsA or on the side chains. Cobalt atoms can enter into the macrocycle or sit between the CsA molecules forming CsA-Co-CsA dimers.

# 4. Conclusions and Outlook

A systematic investigation of two pathways (Schiff base formation and Ullmann coupling) towards synthesizing N-doped graphene nanoribbons, the self-assembly of N-heterocyclic carbene monolayers, and the interaction of a macrocyclic peptide (Cyclosporin A) with different metals (K, Fe, Co), on close-packed Ag(111), Au(111), Cu(111), and Pt(111) surfaces were presented in this thesis. The self-assembly of the molecules was resolved by means of STM. Supplementary XPS measurements provided insight into the chemical state of the molecules.

Different combinations of tetraketone and tetraamine molecules were employed aiming to trigger the Schiff base formation reaction to synthesize N-doped graphene nanoribbons. In the investigation of tetraketone 1 and tetraamine 1, we explored the influence of annealing temperature, stoichiometry of tetraketone to tetraamine, and the underlying metal surface. Only on Ag(111), different oligomers generated, because silver gives the best compromise between adsorption strength and moderate chemical interaction. Besides, we found this imine formation reaction requires an activation step: lift-off of the ketones. On the Au(111) surface, tetraketone 1 and tetraamine 1 went through several temperature dependent phase transformations. But the anchoring appears to be too weak to promote the condensation reaction, such that the majority of the tetraketone molecules desorbed when the temperature was raised. On the contrary, the Cu(111) surface interacts too strongly with the molecules and resulted in decomposition rather than polymerization. In order to produce longer polymers, we tailed the molecular precursors in an attempt to tune the interaction with the substrate by introducing more or less bulky groups. But unfortunately on Ag(111) substrate, the combination of tetraketone 3 and tetraamine 1, tetraketone 2 and tetraamine 1, tetraketone 2 and tetraamine 3, tetraketone 2 and tetraamine 2, all failed to form oligomers, let alone polymers. The main reason still lies in the interaction between molecules and substrate, the compromise between anchoring and mobility of the molecules as well as the intermolecular interactions.

Then we proposed a new method, a two-step reaction to synthesize this N-doped graphene nanoribbons, first utilizing Ullmann coupling to link C-C, and then C-H cleaving and reacting with the neighboring N. We studied two molecules: DBBQ and DBBPP on

three coinage metal substrates: Ag(111), Au(111) and Cu(111). DBBQ formed organometallic chains on all three substrates. Despite the organometallic species being a precursor of the Ullmann coupling product, no well-defined Ullman coupling was observed under any circumstances. There is a significant discovery deduced from N 1s spectra that N interacts strongly either with the Br atoms forming halogen-nitrogen bonds, or with surface metal adatoms, which could interfere with the Ullmann coupling.

The saturated monolayers of a sterically not imposing NHC on Cu(111), Au(111), and Pt(111) single crystal surfaces were investigated. At room temperature the free carbene forms clearly identifiable dimers on Cu(111), which are assigned to planar NHC "stapled" by a Cu adatom. We found a remarkably similar packing on Au(111) and identical spectroscopic signatures of the C 1s and N 1s core levels of the IMe on both surfaces. We therefore deduced on Au(111), the planar bis-carbene metal formation is preferential. On the more active surface Pt(111), dimeric $(IMe)_2$-Pt species also generated and these dimers either register on the three high-symmetric directions of Pt(111) substrate, or in the diagonal directions.

Besides organic molecules, natural cyclic peptides are also used as versatile molecular building units for emerging nanodevices. We investigated a macrocyclic peptide Cyclosporin A on Cu(111) with submolecular resolution. Two kinds of configurations of CsA on Cu(111) have been elucidated by real-space imaging and molecular modeling. Distinct phase transformation were monitored after dosing three different metals. Potassium atoms prefer complexing within the center of CsA and saturate its hydrogen bonding sites. As increasing the coverage of K atoms, CsA-K complexes transformed into uniform triangular species and more and more monomers were observed. Iron atoms may also coordinate with carbonyls of the CsA either sitting in the macrocycle of the CsA or on the side chains. Cobalt atoms can enter into the macrocycle or sit between CsA molecules forming CsA-Co-CsA dimers.

This work has demonstrated the feasibility of preparing PPA-based oligomers on a metal surface, but there is still a long way to go to produce long polymers. Besides the two pathways that were tried in this thesis: Schiff base formation and Ullmann coupling, there are still other reactions that can be utilized in the future. As carbene ligands can bind and stabilize a plethora of metals, they are currently deemed as promising protean surface anchors, but the stability of our produced carbene is not so satisfying, which is the challenge for future work. The findings about the interaction between macrocyclic peptides and different metals can provide valuable input to the design of ion channels.

# 5. Acknowledgments

Firstly, I would like to thank Prof. Johannes Barth for giving me this opportunity to work at E20 in the field of surface science and for his great supervision during the whole period of time. I also would like to thank Dr. Joachim Reichert for his supervision, discussions, for his help in repairing and maintaining the STM equipment so I am able to finish all the experiments. I am extremely thankful to Dr. Anthoula Papageorgiou for direct supervision, frequent discussions, and great help in guiding me to the area of STM. All the techniques and scanning methods that I learned from her are treasures for my future work.

I would like to thank the whole team of the Aarhus–STM group, to our former team members Seung Cheol Oh and Dr. Özge Sağlam who gave me a preliminary introduction of STM and some tips, also to Bodong Zhang, Dr. Yuanyuan Guo, and Dr. Chao Jing for nice cooperation, scientific support, and helpful discussions.

Furthermore, I would like to thank the synchrotron team, Dr. Florian Klappenberger, Dr. Francesco Allegretti, Dr. David A. Duncan, Dr. Yiqi Zhang, and Peter Deimel for great help in XPS measurements performed in synchrotron facility in Berlin and in TUM—WSI laboratory in Garching.

I also want to thank Sandeep More, Dr. Aurelio Mateo-Alonso, and Valentina Montagna from POLYMAT, university of the Basque Country, also to Dr. Guillaume Médard and Dr. Bernard Kuster from Proteomics and Bioanalytics chair of TUM for synthesizing so nice molecules that I can work with.

I would like to thank Viktoria Blaschek for great help in administration and other daily trouble in my life or work, thank Max Glanz for help in computer, software and safety training, and thank Karl Eberle for technical support in XPS measurements.

And I want to thank the colleagues in my office, Alissa Wiengarten, Felix Bischoff, Martin Schwarz, Jacob Ducke, and Juan Li for the nice atmosphere, casual chatting and scientific discussions. And of course I want to thank also everyone else at E20 for your kindness that makes me feel warmed.

Finally, I am deeply grateful to my family. To Xianglan Liu, my mother, for her selfless love and support that got me here. To Yan Jiang, my sister, who accompanies my mother,

takes care of her when I am not at home. To Chengyong Xiao, my husband, who cares about me, loves me, encourages me, always.

This work was supported by the China Scholarship Council (CSC).

# 6. List of publications


1. A. Wiengarten, J.A. Lloyd, K. Seufert, J. Reichert, W. Auwärter, R. Han, D. A. Duncan, F. Allegretti, S. Fischer, S Cheol Oh, ö. Sağlam, L. Jiang, S. Vijayaraghavan, D. Écija, A. C. Papageorgiou and J. V. Barth. Surface-assisted cyclodehydrogenation; break the symmetry, enhance the selectivity. *Chemistry – A European Journal* **2015**, *21*, 12285-12290
2. L. Jiang, A.C. Papageorgiou, S.C. Oh, Ö. Sağlam, J. Reichert, D.A. Duncan, Y. Zhang, F. Klappenberger, Y. Guo, F. Allegretti, S. More, R. Bhosale, A. Mateo-Alonso and J.V. Barth. Synthesis of pyrene-fused pyrazaacenes on metal surfaces: Toward one-dimensional conjugated nanostructures. *ACS Nano*, **2016**, *10* (1), 1033–1041.
3. M. J. Taylor, L. Jiang, J. Reichert, A. C. Papageorgiou, S. K. Beaumont, K. Wilson, A. F. Lee, J. V. Barth, and G. Kyriakou. Catalytic Hydrogenation and Hydrodeoxygenation of Furfural Over Pt(111); a Model System for the Rational Design and Operation of Practical Biomass Conversion Catalysts. *J. Phys. Chem. C*, **2017**, *121* (15), 8490–8497.
4. L. Jiang, G. Médard, B. Zhang, F. Haag, F. Allegretti, J. Reichert, A. P. Seitsonen, B. Kuster, J. V. Barth, and A. C. Papageorgiou. N-Heterocyclic Carbenes on Metal Surfaces: Bis-Carbene Metal Adatom Bonding Scheme of Monolayer Films on Coinage Metal Surfaces. *Submitted*
5. Y. Guo, L. Jiang, B. Zhang, J. Reichert, A. C. Papageorgiou, and J. V. Barth. Interaction of Cyclosporin A with different metal centers: alkali metals vs. transition metals. *In preparation*
6. L. Jiang, A.C. Papageorgiou, B. Zhang, Y. Guo, F. Allegretti, S. More, R. Bhosale, J. Reichert, A. Mateo-Alonso and J.V. Barth. Self-assembly of tetraamine and tetraketone stabilized by H-bond interaction vs. metal-coordination on three different coinage metal surfaces. *In preparation*
7. L. Jiang, A.C. Papageorgiou, B. Zhang, Y. Guo, F. Allegretti, V. Montagna, J. Reichert, A. Mateo-Alonso and J.V. Barth. Investigations of nitrogenated precursors for on-surface Ullmann type coupling polymerization by STM and XPS on coinage metal surfaces. *In preparation*

# Bibliography


(1) Stöhr, M.; Wahl, M.; Galka, C. H.; Riehm, T.; Jung, T. A.; Gade, L. H. *Angewandte Chemie International Edition* **2005**, *44*, 7394.

(2) Guo, J.; Xu, Y.; Jin, S.; Chen, L.; Kaji, T.; Honsho, Y.; Addicoat, M. A.; Kim, J.; Saeki, A.; Ihee, H.; Seki, S.; Irle, S.; Hiramoto, M.; Gao, J.; Jiang, D. *Nat Commun* **2013**, *4*, 2736.

(3) De Feyter, S.; Miura, A.; Yao, S.; Chen, Z.; Würthner, F.; Jonkheijm, P.; Schenning, A. P. H. J.; Meijer, E. W.; De Schryver, F. C. *Nano Letters* **2004**, *5*, 77.

(4) Keeling, D. L.; Oxtoby, N. S.; Wilson, C.; Humphry, M. J.; Champness, N. R.; Beton, P. H. *Nano Letters* **2002**, *3*, 9.

(5) Kudernac, T.; Lei, S.; Elemans, J. A.; De Feyter, S. *Chem Soc Rev* **2009**, *38*, 402.

(6) Theobald, J. A.; Oxtoby, N. S.; Phillips, M. A.; Champness, N. R.; Beton, P. H. *Nature* **2003**, *424*, 1029.

(7) van Hameren, R.; Schön, P.; van Buul, A. M.; Hoogboom, J.; Lazarenko, S. V.; Gerritsen, J. W.; Engelkamp, H.; Christianen, P. C. M.; Heus, H. A.; Maan, J. C.; Rasing, T.; Speller, S.; Rowan, A. E.; Elemans, J. A. A. W.; Nolte, R. J. M. *Science* **2006**, *314*, 1433.

(8) Furukawa, S.; Tahara, K.; De Schryver, F. C.; Van der Auweraer, M.; Tobe, Y.; De Feyter, S. *Angewandte Chemie (International ed. in English)* **2007**, *46*, 2831.

(9) Stepanow, S.; Lingenfelder, M.; Dmitriev, A.; Spillmann, H.; Delvigne, E.; Lin, N.; Deng, X.; Cai, C.; Barth, J. V.; Kern, K. *Nat Mater* **2004**, *3*, 229.

(10) Grill, L.; Dyer, M.; Lafferentz, L.; Persson, M.; Peters, M. V.; Hecht, S. *Nat Nano* **2007**, *2*, 687.

(11) Lackinger, M.; Heckl, W. M. *Journal of Physics D: Applied Physics* **2011**, *44*, 464011.

(12) Perepichka, D. F.; Rosei, F. *Science* **2009**, *323*, 216.

(13) Mendez, J.; Lopez, M. F.; Martin-Gago, J. A. *Chemical Society Reviews* **2011**, *40*, 4578.

(14) Weigelt, S.; Busse, C.; Bombis, C.; Knudsen, M. M.; Gothelf, K. V.; Strunskus, T.; Wöll, C.; Dahlbom, M.; Hammer, B.; Lægsgaard, E.; Besenbacher, F.; Linderoth, T. R. *Angewandte Chemie International Edition* **2007**, *46*, 9227.

(15) Weigelt, S.; Busse, C.; Bombis, C.; Knudsen, M. M.; Gothelf, K. V.; Lægsgaard, E.; Besenbacher, F.; Linderoth, T. R. *Angewandte Chemie International Edition* **2008**, *47*, 4406.

(16) Tanoue, R.; Higuchi, R.; Enoki, N.; Miyasato, Y.; Uemura, S.; Kimizuka, N.; Stieg, A. Z.; Gimzewski, J. K.; Kunitake, M. *ACS Nano* **2011**, *5*, 3923.

(17) Tanoue, R.; Higuchi, R.; Ikebe, K.; Uemura, S.; Kimizuka, N.; Stieg, A. Z.; Gimzewski, J. K.; Kunitake, M. *Langmuir* **2012**, *28*, 13844.

(18) Liu, X.-H.; Guan, C.-Z.; Ding, S.-Y.; Wang, W.; Yan, H.-J.; Wang, D.; Wan, L.-J. *Journal of the American Chemical Society* **2013**, *135*, 10470.

(19) LafferentzL; EberhardtV; DriC; AfrichC; ComelliG; EschF; HechtS; GrillL *Nat Chem* **2012**, *4*, 215.

(20) Fan, Q.; Wang, C.; Han, Y.; Zhu, J.; Kuttner, J.; Hilt, G.; Gottfried, J. M. *ACS Nano* **2014**, *8*, 709.

(21) Gutzler, R.; Walch, H.; Eder, G.; Kloft, S.; Heckl, W. M.; Lackinger, M. *Chemical Communications* **2009**, 4456.

(22) Bieri, M.; Treier, M.; Cai, J.; Ait-Mansour, K.; Ruffieux, P.; Groning, O.; Groning, P.; Kastler, M.; Rieger, R.; Feng, X.; Mullen, K.; Fasel, R. *Chemical Communications* **2009**, 6919.

(23) Bieri, M.; Nguyen, M.-T.; Gröning, O.; Cai, J.; Treier, M.; Aït-Mansour, K.; Ruffieux, P.; Pignedoli, C. A.; Passerone, D.; Kastler, M.; Müllen, K.; Fasel, R. *Journal of the American Chemical Society* **2010**, *132*, 16669.

(24) Blunt, M. O.; Russell, J. C.; Champness, N. R.; Beton, P. H. *Chemical Communications* **2010**, *46*, 7157.

(25) Faury, T.; Dumur, F.; Clair, S.; Abel, M.; Porte, L.; Gigmes, D. *CrystEngComm* **2013**, *15*, 2067.

(26) Zwaneveld, N. A. A.; Pawlak, R.; Abel, M.; Catalin, D.; Gigmes, D.; Bertin, D.; Porte, L. *Journal of the American Chemical Society* **2008**, *130*, 6678.

(27) Guan, C.-Z.; Wang, D.; Wan, L.-J. *Chemical Communications* **2012**, *48*, 2943.

(28) Geim, A. K.; Novoselov, K. S. *Nat Mater* **2007**, *6*, 183.

(29) Allen, M. J.; Tung, V. C.; Kaner, R. B. *Chemical Reviews* **2010**, *110*, 132.

(30) Park, S.; Ruoff, R. S. *Nat Nano* **2009**, *4*, 217.

(31) Geim, A. K. *Science* **2009**, *324*, 1530.

(32) Rosei, F.; Schunack, M.; Naitoh, Y.; Jiang, P.; Gourdon, A.; Laegsgaard, E.; Stensgaard, I.; Joachim, C.; Besenbacher, F. *Progress in Surface Science* **2003**, *71*, 95.

(33) Barth, J. V.; Weckesser, J.; Cai, C.; Günter, P.; Bürgi, L.; Jeandupeux, O.; Kern, K. *Angewandte Chemie International Edition* **2000**, *39*, 1230.

(34) Barlow, S. M.; Raval, R. *Surface Science Reports* **2003**, *50*, 201.

(35) Barth, J. V. *Annual Review of Physical Chemistry* **2007**, *58*, 375.

(36) Wang, H.; Maiyalagan, T.; Wang, X. *ACS Catalysis* **2012**, *2*, 781.

(37) Zhao, L.; He, R.; Rim, K. T.; Schiros, T.; Kim, K. S.; Zhou, H.; Gutiérrez, C.; Chockalingam, S. P.; Arguello, C. J.; Pálová, L.; Nordlund, D.; Hybertsen, M. S.; Reichman, D. R.; Heinz, T. F.; Kim, P.; Pinczuk, A.; Flynn, G. W.; Pasupathy, A. N. *Science* **2011**, *333*, 999.

(38) Lv, R.; Li, Q.; Botello-Méndez, A. R.; Hayashi, T.; Wang, B.; Berkdemir, A.; Hao, Q.; Elías, A. L.; Cruz-Silva, R.; Gutiérrez, H. R.; Kim, Y. A.; Muramatsu, H.; Zhu, J.; Endo, M.; Terrones, H.; Charlier, J.-C.; Pan, M.; Terrones, M. *Sci. Rep.* **2012**, *2*.

(39) Bronner, C.; Stremlau, S.; Gille, M.; Braußе, F.; Haase, A.; Hecht, S.; Tegeder, P. *Angewandte Chemie International Edition* **2013**, *52*, 4422.

(40) Vo, T. H.; Shekhirev, M.; Kunkel, D. A.; Orange, F.; Guinel, M. J. F.; Enders, A.; Sinitskii, A. *Chemical Communications* **2014**, *50*, 4172.

(41) Cai, J.; Pignedoli, C. A.; Talirz, L.; Ruffieux, P.; Söde, H.; Liang, L.; Meunier, V.; Berger, R.; Li, R.; Feng, X.; Müllen, K.; Fasel, R. *Nat Nano* **2014**, *9*, 896.

(42) Wang, X.; Li, X.; Zhang, L.; Yoon, Y.; Weber, P. K.; Wang, H.; Guo, J.; Dai, H. *Science* **2009**, *324*, 768.

(43) Cui, T.; Lv, R.; Huang, Z.-H.; Zhu, H.; Zhang, J.; Li, Z.; Jia, Y.; Kang, F.; Wang, K.; Wu, D. *Carbon* **2011**, *49*, 5022.

(44) Qu, L.; Liu, Y.; Baek, J.-B.; Dai, L. *ACS Nano* **2010**, *4*, 1321.

(45) Elías, A. L.; Carrero-Sánchez, J. C.; Terrones, H.; Endo, M.; Laclette, J. P.; Terrones, M. *Small* **2007**, *3*, 1723.

(46) Carrero-Sánchez, J. C.; Elías, A. L.; Mancilla, R.; Arrellín, G.; Terrones, H.; Laclette, J. P.; Terrones, M. *Nano Letters* **2006**, *6*, 1609.

(47) Wang, Y.; Shao, Y.; Matson, D. W.; Li, J.; Lin, Y. *ACS Nano* **2010**, *4*, 1790.

(48) Crudden, C. M.; Horton, J. H.; Ebralidze, I. I.; Zenkina, O. V.; McLean, A. B.; Drevniok, B.; She, Z.; Kraatz, H.-B.; Mosey, N. J.; Seki, T.; Keske, E. C.; Leake, J. D.; Rousina-Webb, A.; Wu, G. *Nat Chem* **2014**, *6*, 409.

(49) Zahidi, E.; Oudghiri-Hassani, H.; McBreen, P. H. *Nature* **2001**, *409*, 1023.

(50) Zhou, Y.; Trewyn, B. G.; Angelici, R. J.; Woo, L. K. *Journal of the American Chemical Society* **2009**, *131*, 11734.

(51) Tulevski, G. S.; Myers, M. B.; Hybertsen, M. S.; Steigerwald, M. L.; Nuckolls, C. *Science* **2005**, *309*, 591.

(52) Lang, N. D.; Kagan, C. R. *Nano Letters* **2006**, *6*, 2955.

(53) Hopkinson, M. N.; Richter, C.; Schedler, M.; Glorius, F. *Nature* **2014**, *510*, 485.

(54) Zhukhovitskiy, A. V.; MacLeod, M. J.; Johnson, J. A. *Chemical Reviews* **2015**, *115*, 11503.

(55) Marrone, T. J.; Merz, K. M. J. *Journal of the American Chemical Society* **1995**, *117*, 779.

(56) Rizo, J.; Gierasch, L. M. *Annual review of biochemistry* **1992**, *61*, 387.

(57) Amorín, M.; Castedo, L.; Granja, J. R. *Journal of the American Chemical Society* **2003**, *125*, 2844.

(58) Montenegro, J.; Ghadiri, M. R.; Granja, J. R. *Accounts of chemical research* **2013**, *46*, 2955.

(59) Gerd, B. H., Rohrer. *Helvetica Physica Acta* **1982**, *55*, 726.

(60) Atkins, P. W.; dePaula, J. *Physikalische Chemie*; Wiley-VCH: Weinheim, 2001.

(61) Chen, C. J. *Introduction to Scanning Tunneling Microscopy*; Oxford University Press: Oxford, 1993.

(62) Bardeen, J. *Physical Review Letters* **1961**, *6*, 57.

(63) Tersoff, J.; Hamann, D. R. *Physical Review B* **1985**, *31*, 805.

(64) Murphy, B. E., Trinity College Dublin, 2014.

(65) Besenbacher, F.; Lægsgaard, E.; Stensgaard, I. *Materials Today* **2005**, *8*, 26.

(66) Laegsgaard, E.; Österlund, L.; Thostrup, P.; Rasmussen, P. B.; Stensgaard, I.; Besenbacher, F. *Review of Scientific Instruments* **2001**, *72*, 3537.

(67) Fischer, S., Technical University of Munich, 2013.

(68) Vestergaard, E. K., University of Aarhus, 2004.

(69) Horcas, I.; Fernández, R.; Gómez-Rodríguez, J. M.; Colchero, J.; Gómez-Herrero, J.; Baro, A. M. *Review of Scientific Instruments* **2007**, *78*.

(70) Einstein, A. *Annalen der Physik* **1905**, *322*, 132.

(71) Takayama, A. In *High-Resolution Spin-Resolved Photoemission Spectrometer and the Rashba Effect in Bismuth Thin Films*; Springer Japan: Tokyo, 2015, p 15.

(72) Kamplain, J. W.; Lynch, V. M.; Bielawski, C. W. *Organic Letters* **2007**, *9*, 5401.

(73) Lazreg, F.; Slawin, A. M. Z.; Cazin, C. S. J. *Organometallics* **2012**, *31*, 7969.

(74) Rodriguez-Castillo, M.; Laurencin, D.; Tielens, F.; van der Lee, A.; Clement, S.; Guari, Y.; Richeter, S. *Dalton Transactions* **2014**, *43*, 5978.

(75) Kroto, H. W.; Heath, J. R.; O'Brien, S. C.; Curl, R. F.; Smalley, R. E. *Nature* **1985**, *318*, 162.

(76) Denk, R.; Hohage, M.; Zeppenfeld, P.; Cai, J.; Pignedoli, C. A.; Söde, H.; Fasel, R.; Feng, X.; Müllen, K.; Wang, S.; Prezzi, D.; Ferretti, A.; Ruini, A.; Molinari, E.; Ruffieux, P. *Nat Commun* **2014**, *5*.

(77) Mateo-Alonso, A. *Chemical Society Reviews* **2014**, *43*, 6311.

(78) Mateo-Alonso, A.; Ehli, C.; Chen, K. H.; Guldi, D. M.; Prato, M. *Journal of Physical Chemistry A* **2007**, *111*, 12669.

(79) Mateo-Alonso, A.; Kulisic, N.; Valenti, G.; Marcaccio, M.; Paolucci, F.; Prato, M. *Chemistry-an Asian Journal* **2010**, *5*, 482.

(80) Kulisic, N.; More, S.; Mateo-Alonso, A. *Chemical Communications* **2011**, *47*, 514.

(81) More, S.; Bhosale, R.; Choudhary, S.; Mateo-Alonso, A. *Organic Letters* **2012**, *14*, 4170.

(82) More, S.; Bhosale, R.; Mateo-Alonso, A. *Chemistry – A European Journal* **2014**, *20*, 10626.

(83) Gao, B. X.; Wang, M.; Cheng, Y. X.; Wang, L. X.; Jing, X. B.; Wang, F. S. *Journal of the American Chemical Society* **2008**, *130*, 8297.

(84) Stille, J. K.; Mainen, E. L. *Journal of Polymer Science Part B-Polymer Letters* **1966**, *4*, 665.

(85) Stille, J. K.; Mainen, E. L. *Macromolecules* **1968**, *1*, 36.

(86) Imai, K.; Kuhihara, M.; Mathias, L.; Wittmann, J.; Alston, W. B.; Stille, J. K. *Macromolecules* **1973**, *6*, 158.

(87) Hu, F.-Y.; Zhang, X.-M.; Wang, X.-C.; Wang, S.; Wang, H.-Q.; Duan, W.-B.; Zeng, Q.-D.; Wang, C. *ACS Applied Materials & Interfaces* **2013**, *5*, 1583.

(88) Liu, X.-H.; Mo, Y.-P.; Yue, J.-Y.; Zheng, Q.-N.; Yan, H.-J.; Wang, D.; Wan, L.-J. *Small* **2014**, *10*, 4934.

(89) Tanoue, R.; Higuchi, R.; Ikebe, K.; Uemura, S.; Kimizuka, N.; Stieg, A. Z.; Gimzewski, J. K.; Kunitake, M. *Journal of Electroanalytical Chemistry* **2014**, *716*, 145.

(90) Xu, L.; Zhou, X.; Tian, W. Q.; Gao, T.; Zhang, Y. F.; Lei, S.; Liu, Z. F. *Angewandte Chemie International Edition* **2014**, *53*, 9564.

(91) Xu, L.; Zhou, X.; Yu, Y.; Tian, W. Q.; Ma, J.; Lei, S. *ACS Nano* **2013**, *7*, 8066.

(92) Ciesielski, A.; El Garah, M.; Haar, S.; Kovaříček, P.; Lehn, J.-M.; Samorì, P. *Nat Chem* **2014**, *6*, 1017.

(93) Alvarado, S. F.; Rieß, W.; Jandke, M.; Strohriegl, P. *Organic Electronics* **2001**, *2*, 75.

(94) Jiang, L.; Papageorgiou, A. C.; Oh, S. C.; Sağlam, Ö.; Reichert, J.; Duncan, D. A.; Zhang, Y.-Q.; Klappenberger, F.; Guo, Y.; Allegretti, F.; More, S.; Bhosale, R.; Mateo-Alonso, A.; Barth, J. V. *ACS Nano* **2016**, *10*, 1033.

(95) Oh, S. C., Technical University of Munich 2014.

(96) Huang, S. X.; Fischer, D. A.; Gland, J. L. *The Journal of Physical Chemistry* **1996**, *100*, 10223.

(97) Furukawa, M.; Yamada, T.; Katano, S.; Kawai, M.; Ogasawara, H.; Nilsson, A. *Surface Science* **2007**, *601*, 5433.

(98) Lin, Y.-P.; Ourdjini, O.; Giovanelli, L.; Clair, S.; Faury, T.; Ksari, Y.; Themlin, J.-M.; Porte, L.; Abel, M. *The Journal of Physical Chemistry C* **2013**, *117*, 9895.

(99) Davies, P. R.; Edwards, D.; Richards, D. *The Journal of Physical Chemistry B* **2004**, *108*, 18630.

(100) Heimel, G.; Duhm, S.; Salzmann, I.; Gerlach, A.; Strozecka, A.; Niederhausen, J.; Bürker, C.; Hosokai, T.; Fernandez Torrente, I.; Schulze, G.; Winkler, S.; Wilke, A.; Schlesinger, R.; Frisch, J.; Bröker, B.; Vollmer, A.; Detlefs, B.; Pflaum, J.; Kera, S.; Franke, K. J.; Ueno, N.; Pascual, J. I.; Schreiber, F.; Koch, N. *Nat Chem* **2013**, *5*, 187.

(101) Wiengarten, A.; Seufert, K.; Auwärter, W.; Ecija, D.; Diller, K.; Allegretti, F.; Bischoff, F.; Fischer, S.; Duncan, D. A.; Papageorgiou, A. C.; Klappenberger, F.; Acres, R. G.; Ngo, T. H.; Barth, J. V. *Journal of the American Chemical Society* **2014**, *136*, 9346.

(102) Moulder, J. F. *Handbook of X-ray photoelectron spectroscopy: a reference book of standard spectra for identification and interpretation of XPS data*, 1992.

(103) Rancan, M.; Sedona, F.; Di Marino, M.; Armelao, L.; Sambi, M. *Chemical Communications* **2011**, *47*, 5744.

(104) Li, K.; Amann, T.; List, M.; Walter, M.; Moseler, M.; Kailer, A.; Rühe, J. *Langmuir* **2015**.

(105) Fischer, S.; Papageorgiou, A. C.; Lloyd, J. A.; Oh, S. C.; Diller, K.; Allegretti, F.; Klappenberger, F.; Seitsonen, A. P.; Reichert, J.; Barth, J. V. *ACS Nano* **2014**, *8*, 207.

(106) Fischer, S.; Papageorgiou, A. C.; Marschall, M.; Reichert, J.; Diller, K.; Klappenberger, F.; Allegretti, F.; Nefedov, A.; Wöll, C.; Barth, J. V. *Journal of Physical Chemistry C* **2012**, *116*, 20356.

(107) Kürpick, U.; Rahman, T. S. *Physical Review Letters* **1999**, *83*, 2765.

(108) Bartels, L.; Meyer, G.; Rieder, K. H. *Physical Review Letters* **1997**, *79*, 697.

(109) Meyer, G.; Rieder, K. H. *MRS Bulletin* **2013**, *23*, 28.

(110) Meyer, G.; Repp, J.; Zöphel, S.; Braun, K.-F.; Hla, S. W.; Fölsch, S.; Bartels, L.; Moresco, F.; Rieder, K. H. *Single Molecules* **2000**, *1*, 79.

(111) Shchyrba, A.; Wäckerlin, C.; Nowakowski, J.; Nowakowska, S.; Björk, J.; Fatayer, S.; Girovsky, J.; Nijs, T.; Martens, S. C.; Kleibert, A.; Stöhr, M.; Ballav, N.; Jung, T. A.; Gade, L. H. *Journal of the American Chemical Society* **2014**, *136*, 9355.

(112) Zhang, Y.-Q.; Kepčija, N.; Kleinschrodt, M.; Diller, K.; Fischer, S.; Papageorgiou, A. C.; Allegretti, F.; Björk, J.; Klyatskaya, S.; Klappenberger, F.; Ruben, M.; Barth, J. V. *Nat Commun* **2012**, *3*, 1286.

(113) Papageorgiou, A. C.; Fischer, S.; Reichert, J.; Diller, K.; Blobner, F.; Klappenberger, F.; Allegretti, F.; Seitsonen, A. P.; Barth, J. V. *ACS Nano* **2012**, *6*, 2477.

(114) Novoselov, K. S.; Geim, A. K.; Morozov, S. V.; Jiang, D.; Zhang, Y.; Dubonos, S. V.; Grigorieva, I. V.; Firsov, A. A. *Science* **2004**, *306*, 666.

(115) Cardenas, L.; Gutzler, R.; Lipton-Duffin, J.; Fu, C.; Brusso, J. L.; Dinca, L. E.; Vondracek, M.; Fagot-Revurat, Y.; Malterre, D.; Rosei, F.; Perepichka, D. F. *Chemical Science* **2013**, *4*, 3263.

(116) Wei, D.; Liu, Y.; Wang, Y.; Zhang, H.; Huang, L.; Yu, G. *Nano Letters* **2009**, *9*, 1752.

(117) Deifallah, M.; McMillan, P. F.; Corà, F. *The Journal of Physical Chemistry C* **2008**, *112*, 5447.

(118) Roldán, R.; López-Sancho, M. P.; Guinea, F. *Physical Review B* **2008**, *77*, 115410.

(119) Dai, J.; Yuan, J.; Giannozzi, P. *Applied Physics Letters* **2009**, *95*, 232105.

(120) Panchakarla, L. S.; Subrahmanyam, K. S.; Saha, S. K.; Govindaraj, A.; Krishnamurthy, H. R.; Waghmare, U. V.; Rao, C. N. R. *Advanced Materials* **2009**, *21*, 4726.

(121) Sun, Z.; Yan, Z.; Yao, J.; Beitler, E.; Zhu, Y.; Tour, J. M. *Nature* **2010**, *468*, 549.

(122) Jin, Z.; Yao, J.; Kittrell, C.; Tour, J. M. *ACS Nano* **2011**, *5*, 4112.

(123) Deng, D.; Pan, X.; Yu, L.; Cui, Y.; Jiang, Y.; Qi, J.; Li, W.-X.; Fu, Q.; Ma, X.; Xue, Q.; Sun, G.; Bao, X. *Chemistry of Materials* **2011**, *23*, 1188.

(124) Ullmann, F.; Bielecki, J. *Berichte der deutschen chemischen Gesellschaft* **1901**, *34*, 2174.

(125) Lipton-Duffin, J. A.; Ivasenko, O.; Perepichka, D. F.; Rosei, F. *Small* **2009**, *5*, 592.

(126) Lipton-Duffin, J. A.; Miwa, J. A.; Kondratenko, M.; Cicoira, F.; Sumpter, B. G.; Meunier, V.; Perepichka, D. F.; Rosei, F. *Proceedings of the National Academy of Sciences* **2010**, *107*, 11200.

(127) Wang, W.; Shi, X.; Wang, S.; Van Hove, M. A.; Lin, N. *Journal of the American Chemical Society* **2011**, *133*, 13264.

(128) Bieri, M.; Blankenburg, S.; Kivala, M.; Pignedoli, C. A.; Ruffieux, P.; Mullen, K.; Fasel, R. *Chemical Communications* **2011**, *47*, 10239.

(129) Cai, J.; Ruffieux, P.; Jaafar, R.; Bieri, M.; Braun, T.; Blankenburg, S.; Muoth, M.; Seitsonen, A. P.; Saleh, M.; Feng, X.; Mullen, K.; Fasel, R. *Nature* **2010**, *466*, 470.

(130) Liu, J.; Li, B.-W.; Tan, Y.-Z.; Giannakopoulos, A.; Sanchez-Sanchez, C.; Beljonne, D.; Ruffieux, P.; Fasel, R.; Feng, X.; Müllen, K. *Journal of the American Chemical Society* **2015**, *137*, 6097.

(131) Treier, M.; Pignedoli, C. A.; Laino, T.; Rieger, R.; Müllen, K.; Passerone, D.; Fasel, R. *Nat Chem* **2011**, *3*, 61.

(132) In't Veld, M.; Iavicoli, P.; Haq, S.; Amabilino, D. B.; Raval, R. *Chemical Communications* **2008**, 1536.

(133) Haq, S.; Hanke, F.; Sharp, J.; Persson, M.; Amabilino, D. B.; Raval, R. *ACS Nano* **2014**, *8*, 8856.

(134) El-Shall, M. S.; Ibrahim, Y. M.; Alsharaeh, E. H.; Meot-Ner, M.; Watson, S. P. *Journal of the American Chemical Society* **2009**, *131*, 10066.

(135) Chen, M.; Xiao, J.; Steinrück, H.-P.; Wang, S.; Wang, W.; Lin, N.; Hieringer, W.; Gottfried, J. M. *The Journal of Physical Chemistry C* **2014**, *118*, 6820.

(136) Fan, Q.; Wang, C.; Liu, L.; Han, Y.; Zhao, J.; Zhu, J.; Kuttner, J.; Hilt, G.; Gottfried, J. M. *The Journal of Physical Chemistry C* **2014**, *118*, 13018.

(137) Di Giovannantonio, M.; El Garah, M.; Lipton-Duffin, J.; Meunier, V.; Cardenas, L.; Fagot Revurat, Y.; Cossaro, A.; Verdini, A.; Perepichka, D. F.; Rosei, F.; Contini, G. *ACS Nano* **2013**, *7*, 8190.

(138) Ferrighi, L.; Píš, I.; Nguyen, T. H.; Cattelan, M.; Nappini, S.; Basagni, A.; Parravicini, M.; Papagni, A.; Sedona, F.; Magnano, E.; Bondino, F.; Di Valentin, C.; Agnoli, S. *Chemistry – A European Journal* **2015**, *21*, 5826.

(139) Píš, I.; Ferrighi, L.; Nguyen, T. H.; Nappini, S.; Vaghi, L.; Basagni, A.; Magnano, E.; Papagni, A.; Sedona, F.; Di Valentin, C.; Agnoli, S.; Bondino, F. *The Journal of Physical Chemistry C* **2016**, *120*, 4909.

(140) Basagni, A.; Ferrighi, L.; Cattelan, M.; Nicolas, L.; Handrup, K.; Vaghi, L.; Papagni, A.; Sedona, F.; Valentin, C. D.; Agnoli, S.; Sambi, M. *Chemical Communications* **2015**, *51*, 12593.

(141) Basagni, A.; Vasseur, G.; Pignedoli, C. A.; Vilas-Varela, M.; Peña, D.; Nicolas, L.; Vitali, L.; Lobo-Checa, J.; de Oteyza, D. G.; Sedona, F.; Casarin, M.; Ortega, J. E.; Sambi, M. *ACS Nano* **2016**, *10*, 2644.

(142) Papageorgiou, A. C.; Diller, K.; Fischer, S.; Allegretti, F.; Klappenberger, F.; Oh, S. C.; Sağlam, Ö.; Reichert, J.; Wiengarten, A.; Seufert, K.; Auwärter, W.; Barth, J. V. *The Journal of Physical Chemistry C* **2016**, *120*, 8751.

(143) Diller, K.; Klappenberger, F.; Marschall, M.; Hermann, K.; Nefedov, A.; Wöll, C.; Barth, J. V. *The Journal of Chemical Physics* **2012**, *136*, 014705.

(144) Diller, K.; Papageorgiou, A. C.; Klappenberger, F.; Allegretti, F.; Barth, J. V.; Auwärter, W. *Chem. Soc. Rev.* **2016**, *45*, 1629.

(145) Cavallo, G.; Metrangolo, P.; Milani, R.; Pilati, T.; Priimagi, A.; Resnati, G.; Terraneo, G. *Chemical Reviews* **2016**, *116*, 2478.

(146) Mavracic, J.; Cincic, D.; Kaitner, B. *CrystEngComm* **2016**, *18*, 3343.

(147) Khavasi, H. R.; Hosseini, M.; Tehrani, A. A.; Naderi, S. *CrystEngComm* **2014**, *16*, 4546.

(148) Park, J.; Kim, K. Y.; Chung, K.-H.; Yoon, J. K.; Kim, H.; Han, S.; Kahng, S.-J. *The Journal of Physical Chemistry C* **2011**, *115*, 14834.

(149) Basagni, A.; Sedona, F.; Pignedoli, C. A.; Cattelan, M.; Nicolas, L.; Casarin, M.; Sambi, M. *Journal of the American Chemical Society* **2015**, *137*, 1802.

(150) Beamson, G.; Briggs, D. *High Resolution XPS of Organic Polymers: The Scienta ESCA300 Database*; Wiley: New York, 1992.

(151) Simonov, K. A.; Vinogradov, N. A.; Vinogradov, A. S.; Generalov, A. V.; Zagrebina, E. M.; Mårtensson, N.; Cafolla, A. A.; Carpy, T.; Cunniffe, J. P.; Preobrajenski, A. B. *The Journal of Physical Chemistry C* **2014**, *118*, 12532.

(152) Wang, D.-W.; Su, D. *Energy & Environmental Science* **2014**, *7*, 576.

(153) Kundu, S.; Nagaiah, T. C.; Xia, W.; Wang, Y.; Dommele, S. V.; Bitter, J. H.; Santa, M.; Grundmeier, G.; Bron, M.; Schuhmann, W.; Muhler, M. *The Journal of Physical Chemistry C* **2009**, *113*, 14302.

(154) Maldonado, S.; Morin, S.; Stevenson, K. J. *Carbon* **2006**, *44*, 1429.

(155) Rao, C. V.; Cabrera, C. R.; Ishikawa, Y. *The Journal of Physical Chemistry Letters* **2010**, *1*, 2622.

(156) Gammon, W. J.; Kraft, O.; Reilly, A. C.; Holloway, B. C. *Carbon* **2003**, *41*, 1917.

(157) Shen, C.; Haryono, M.; Grohmann, A.; Buck, M.; Weidner, T.; Ballav, N.; Zharnikov, M. *Langmuir* **2008**, *24*, 12883.

(158) Koch, M., Freien Universität Berlin, 2013.

(159) Weber, P. B.; Hellwig, R.; Paintner, T.; Lattelais, M.; Paszkiewicz, M.; Casado Aguilar, P.; Deimel, P. S.; Guo, Y.; Zhang, Y.-Q.; Allegretti, F.; Papageorgiou, A. C.; Reichert, J.; Klyatskaya, S.; Ruben, M.; Barth, J. V.; Bocquet, M.-L.; Klappenberger, F. *Angewandte Chemie International Edition* **2016**, *55*, 5754.

(160) Marschall, M.; Reichert, J.; Diller, K.; Klyatskaya, S.; Ruben, M.; Nefedov, A.; Wöll, C.; Kantorovich, L. N.; Klappenberger, F.; Barth, J. V. *The Journal of Physical Chemistry C* **2014**, *118*, 2622.

(161) Urban, C.; Wang, Y.; Rodriguez-Fernandez, J.; Garcia, R.; Herranz, M. A.; Alcami, M.; Martin, N.; Martin, F.; Gallego, J. M.; Miranda, R.; Otero, R. *Chemical Communications* **2014**, *50*, 833.

(162) Yeh, J. J.; Lindau, I. *Atomic Data and Nuclear Data Tables* **1985**, *32*, 1.

(163) Blake, M. M.; Nanayakkara, S. U.; Claridge, S. A.; Fernández-Torres, L. C.; Sykes, E. C. H.; Weiss, P. S. *The Journal of Physical Chemistry A* **2009**, *113*, 13167.

(164) Crudden, C. M.; Horton, J. H.; Narouz, M. R.; Li, Z.; Smith, C. A.; Munro, K.; Baddeley, C. J.; Larrea, C. R.; Drevniok, B.; Thanabalasingam, B.; McLean, A. B.; Zenkina, O. V.; Ebralidze, I. I.; She, Z.; Kraatz, H.-B.; Mosey, N. J.; Saunders, L. N.; Yagi, A. *Nature Communications* **2016**, *7*, 12654.

(165) Wang, G.; Rühling, A.; Amirjalayer, S.; Knor, M.; Ernst, J. B.; Richter, C.; Gao, H.-J.; Timmer, A.; Gao, H.-Y.; Doltsinis, N. L.; Glorius, F.; Fuchs, H. *Nat. Chem.* **2017**, *9*, 152.

(166) Gomez-Suarez, A.; Nelson, D. J.; Nolan, S. P. *Chemical Communications* **2017**.

(167) Lara, P.; Rivada-Wheelaghan, O.; Conejero, S.; Poteau, R.; Philippot, K.; Chaudret, B. *Angewandte Chemie International Edition* **2011**, *50*, 12080.

(168) Zhukhovitskiy, A. V.; Mavros, M. G.; Van Voorhis, T.; Johnson, J. A. *Journal of the American Chemical Society* **2013**, *135*, 7418.

(169) Jolly, P. I.; Zhou, S.; Thomson, D. W.; Garnier, J.; Parkinson, J. A.; Tuttle, T.; Murphy, J. A. *Chemical Science* **2012**, *3*, 1675.

(170) Matena, M.; Riehm, T.; Stöhr, M.; Jung, T. A.; Gade, L. H. *Angewandte Chemie* **2008**, *120*, 2448.

(171) Hu, X.; Castro-Rodriguez, I.; Olsen, K.; Meyer, K. *Organometallics* **2004**, *23*, 755.

(172) Lewis, E. A.; Murphy, C. J.; Liriano, M. L.; Sykes, E. C. H. *Chemical Communications* **2014**, *50*, 1006.

(173) Walch, H.; Gutzler, R.; Sirtl, T.; Eder, G.; Lackinger, M. *The Journal of Physical Chemistry C* **2010**, *114*, 12604.

(174) Walch, H.; Dienstmaier, J.; Eder, G.; Gutzler, R.; Schlögl, S.; Sirtl, T.; Das, K.; Schmittel, M.; Lackinger, M. *Journal of the American Chemical Society* **2011**, *133*, 7909.

(175) Eichberger, M.; Marschall, M.; Reichert, J.; Weber-Bargioni, A.; Auwärter, W.; Wang, R. L. C.; Kreuzer, H. J.; Pennec, Y.; Schiffrin, A.; Barth, J. V. *Nano Letters* **2008**, *8*, 4608.

(176) Pivetta, M.; Pacchioni, G. E.; Schlickum, U.; Barth, J. V.; Brune, H. *Physical Review Letters* **2013**, *110*, 086102.

(177) Pacchioni, G. E.; Pivetta, M.; Brune, H. *The Journal of Physical Chemistry C* **2015**, *119*, 25442.

(178) Björk, J.; Matena, M.; Dyer, M. S.; Enache, M.; Lobo-Checa, J.; Gade, L. H.; Jung, T. A.; Stöhr, M.; Persson, M. *Physical Chemistry Chemical Physics* **2010**, *12*, 8815.

(179) Haq, S.; Hanke, F.; Dyer, M. S.; Persson, M.; Iavicoli, P.; Amabilino, D. B.; Raval, R. *Journal of the American Chemical Society* **2011**, *133*, 12031.

(180) Diller, K.; Klappenberger, F.; Allegretti, F.; Papageorgiou, A. C.; Fischer, S.; Wiengarten, A.; Joshi, S.; Seufert, K.; Écija, D.; Auwärter, W.; Barth, J. V. *The Journal of Chemical Physics* **2013**, *138*, 154710.

(181) Lloyd, J. A.; Papageorgiou, A. C.; Fischer, S.; Oh, S. C.; Sağlam, Ö.; Diller, K.; Duncan, D. A.; Allegretti, F.; Klappenberger, F.; Stöhr, M.; Maurer, R. J.; Reuter, K.; Reichert, J.; Barth, J. V. *Nano Letters* **2016**, *16*, 1884.

(182) Barth, J. V.; Brune, H.; Ertl, G.; Behm, R. J. *Physical Review B* **1990**, *42*, 9307.

(183) Driver, S. M.; Zhang, T.; King, D. A. *Angewandte Chemie International Edition* **2007**, *46*, 700.

(184) Jewell, A. D.; Tierney, H. L.; Sykes, E. C. H. *Physical Review B* **2010**, *82*, 205401.

(185) Jewell, A. D.; Sykes, E. C. H.; Kyriakou, G. *ACS Nano* **2012**, *6*, 3545.

(186) Maksymovych, P.; Sorescu, D. C.; Yates, J. T. *Physical Review Letters* **2006**, *97*, 146103.

(187) Schreiber, F. *Progress in Surface Science* **2000**, *65*, 151.

(188) Hu, G.; Jin, R.; Jiang, D.-e. *Nanoscale* **2016**, *8*, 20103.

(189) Diller, K.; Klappenberger, F.; Allegretti, F.; Papageorgiou, A. C.; Fischer, S.; Duncan, D. A.; Maurer, R. J.; Lloyd, J. A.; Oh, S. C.; Reuter, K.; Barth, J. V. *Journal of Chemical Physics* **2014**, *141*.

(190) Tao, F.; Yuan, Z. L.; Chen, X. F.; Qiao, M. H.; Wang, Z. H.; Dai, Y. J.; Huang, H. G.; Cao, Y.; Xu, G. Q. *Physical Review B* **2003**, *67*, 245406.

(191) Plekan, O.; Feyer, V.; Richter, R.; Coreno, M.; de Simone, M.; Prince, K. C.; Trofimov, A. B.; Gromov, E. V.; Zaytseva, I. L.; Schirmer, J. *Chemical Physics* **2008**, *347*, 360.

(192) Taige, M. A.; Ahrens, S.; Strassner, T. *Journal of Organometallic Chemistry* **2011**, *696*, 2918.

(193) Uemura, S.; Tanoue, R.; Yilmaz, N.; Ohira, A.; Kunitake, M. *Materials* **2010**, *3*, 4252.

(194) Uemura, S.; Sakata, M.; Hirayama, C.; Kunitake, M. *Langmuir* **2004**, *20*, 9198.

(195) Pinardi, A. L.; Otero-Irurueta, G.; Palacio, I.; Martinez, J. I.; Sanchez-Sanchez, C.; Tello, M.; Rogero, C.; Cossaro, A.; Preobrajenski, A.; Gómez-Lor, B.; Jancarik, A.; Stará, I. G.; Starý, I.; Lopez, M. F.; Méndez, J.; Martin-Gago, J. A. *ACS Nano* **2013**, *7*, 3676.

(196) Furlong, I. J.; Mediavilla, C. L.; Ascaso, R.; Rivas, A. L.; Collins, M. K. *Cell Death & Differentiation* **1998**, *5*.

(197) Komatsu, Y.; Tomizaki, K.-y.; Tsukamoto, M.; Kato, T.; Nishino, N.; Sato, S.; Yamori, T.; Tsuruo, T.; Furumai, R.; Yoshida, M. *Cancer Research* **2001**, *61*, 4459.

(198) Weber, C.; Wider, G.; Von Freyberg, B.; Traber, R.; Braun, W.; Widmer, H.; Wüthrich, K. *Biochemistry* **1991**, *30*, 6563.

(199) Bogdanowich-Knipp, S. J.; Chakrabarti, S.; Siahaan, T. J.; Williams, T. D.; Dillman, R. K. *The Journal of Peptide Research* **1999**, *53*, 530.

(200) Casnati, A.; Pochini, A.; Ungaro, R.; Bocchi, C.; Ugozzoli, F.; Egberink, R. J.; Struijk, H.; Lugtenberg, R.; De Jong, F.; Reinhoudt, D. N. *Chemistry–A European Journal* **1996**, *2*, 436.

(201) Seabra, A. B.; Duran, N. *Peptides* **2013**, *39*, 47.

(202) Brea, R. J.; Reiriz, C.; Granja, J. R. *Chemical Society Reviews* **2010**, *39*, 1448.

(203) Ghadiri, M. R.; Granja, J. R.; Milligan, R. A.; McRee, D. E.; Khazanovich, N. *Nature* **1993**, *366*, 324.

(204) Bernardi, F.; Gaggelli, E.; Molteni, E.; Porciatti, E.; Valensin, D.; Valensin, G. *Biophysical journal* **2006**, *90*, 1350.

(205) Mikol, V.; Papageorgiou, C.; Borer, X. *Journal of medicinal chemistry* **1995**, *38*, 3361.

(206) Rinke, G.; Rauschenbach, S.; Harnau, L.; Albarghash, A.; Pauly, M.; Kern, K. *Nano letters* **2014**, *14*, 5609.

(207) Wang, Y.; Lingenfelder, M.; Classen, T.; Costantini, G.; Kern, K. *Journal of the American Chemical Society* **2007**, *129*, 15742.

(208) Deng, Z.; Thontasen, N.; Malinowski, N.; Rinke, G.; Harnau, L.; Rauschenbach, S.; Kern, K. *Nano Letters* **2012**, *12*, 2452.

(209) Abb, S.; Harnau, L.; Gutzler, R.; Rauschenbach, S.; Kern, K. *Nat Commun* **2016**, *7*.

(210) Li, Y.; Liu, C.; Xie, Y.; Li, X.; Fan, X.; Yuan, L.; Zeng, Q. *Chemical Communications* **2013**, *49*, 9021.

(211) Tan, N.-H.; Zhou, J. *Chemical reviews* **2006**, *106*, 840.

(212) Oates, J. A.; Wood, A. J.; Kahan, B. D. *New England Journal of Medicine* **1989**, *321*, 1725.

(213) Stevenson, C. L.; Tan, M. M.; Lechuga‐Ballesteros, D. *Journal of pharmaceutical sciences* **2003**, *92*, 1832.

(214) Schiffrin, A.; Reichert, J.; Pennec, Y.; Auwärter, W.; Weber-Bargioni, A.; Marschall, M.; Dell'Angela, M.; Cvetko, D.; Bavdek, G.; Cossaro, A. *The Journal of Physical Chemistry C* **2009**, *113*, 12101.

(215) Lingenfelder, M.; Tomba, G.; Costantini, G.; Colombi Ciacchi, L.; De Vita, A.; Kern, K. *Angewandte Chemie International Edition* **2007**, *46*, 4492.

(216) Knott, R. B.; Schefer, J.; Schoenborn, B. *Acta Crystallographica Section C: Crystal Structure Communications* **1990**, *46*, 1528.

(217) Neupert‐Laves, K.; Dobler, M. *Helvetica chimica acta* **1975**, *58*, 432.